SIGMA HYPERON PRODUCTION IN A TRIGGERED BUBBLE CHAMBER

by

Tejinder Singh Virdee

A thesis submitted for the degree
of Doctor of Philosophy of the
University of London

Department of Physics
Imperial College
London SW7

February 1979

ABSTRACT

Results on a pair of line reversed reactions

$$\pi^+ p \rightarrow K^+ \Sigma^+$$

$$K^- p \rightarrow \pi^- \Sigma^+$$

at 7.0 Gev/c are presented. Data were taken in the SLAC 1m. rapid cycling bubble chamber with the flashes being triggered by the fast forward going meson. Channel and differential cross-sections were extracted. The observation of the parity violating decay of the sigma hyperon in the bubble chamber enabled the measurement of its polarization. The results are compared with exchange degeneracy predictions. Results obtained at 11.5 Gev/c in the same apparatus by the SLAC bubble chamber group working in a loose collaboration with our group, are used to examine energy dependence. Results of a fit to a phenomenological model are also presented.

CONTENTS

Chapter 4. Corrections I

Chapter 5. Corrections II

Chapter 6. The Results

Chapter 7. Discussion and the Implication of the Results

Appendix 1

References

Acknowledgements

CHAPTER 1

Motivation For the Experiment

1.1 Introduction

Almost all of the information in particle physics is obtained by the study of collision processes. The dominant interaction in these processes is the strong interaction. Although a substantial amount of experimental data on strong interactions has been accumulated since the discovery of the pi-meson in 1947, no single theory has been able to describe the data in quantitative detail. The study of two-body elastic and inelastic reactions provides a good starting point for any theory.

1.2 Classification Schemes [1]

As the discovered number of particle states increased, certain regular patterns with respect to both internal (eg. isospin, hypercharge) and external (eg. spin) quantum numbers were noticed.

Particles with the same spin and parity were grouped into a classification involving representations of a special unitary symmetry group, the SU(3) group. Another scheme, the Regge recurrences, classified particles with the same internal quantum numbers but with different spins and masses. Fig. 1.1 illustrates the two schemes.

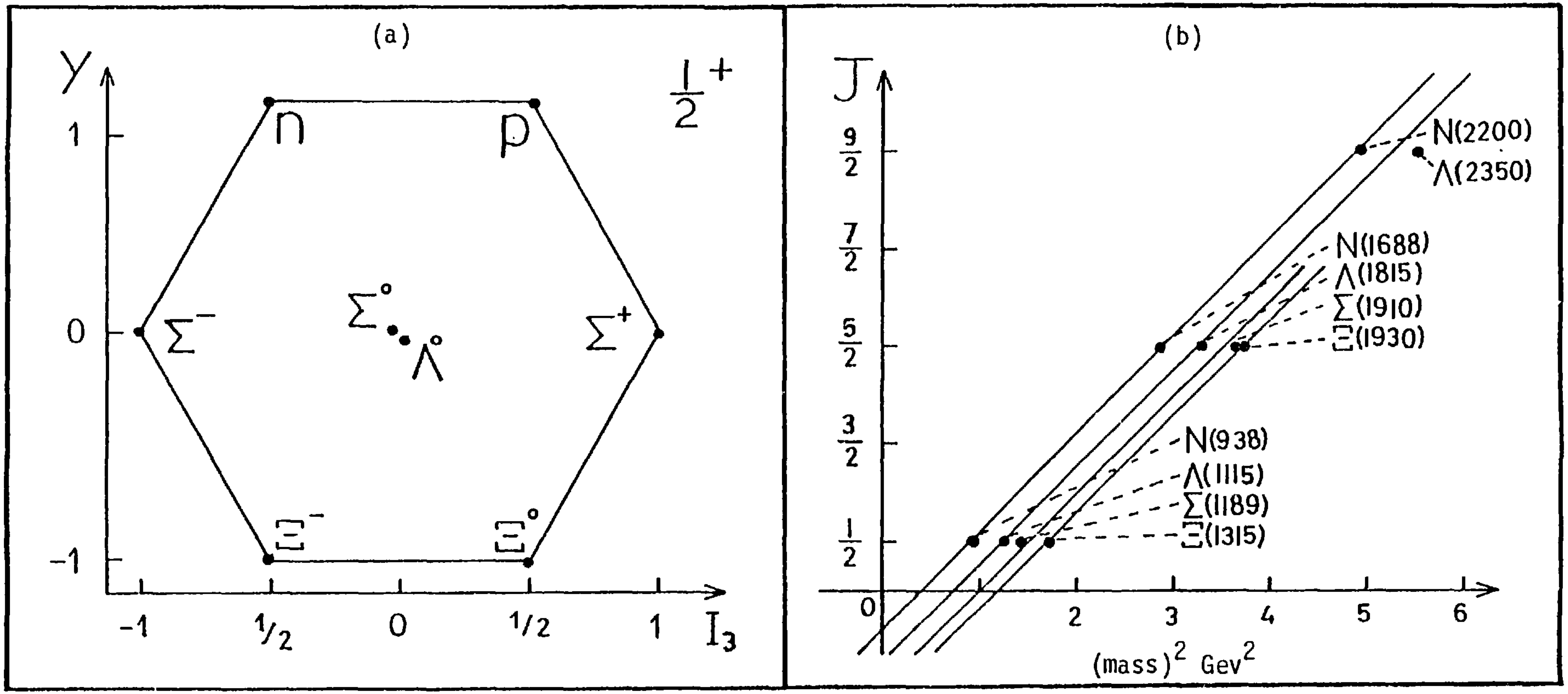

Fig. 1.1 The Classification Schemes

(a) The SU(3) Octet classification of spin-parity $1/2^+$ Baryons.

(b) The Chew-Frautschi plot for (N, Λ, Σ, Ξ) Baryons. The lines, assumed to be Regge Trajectories, connect families with same I, B and S. J is the intrinsic spin of the particles.

1.3 Two Body Phenomenology

At high energies, many two-body and quasi-two body hadron-hadron reactions are characterized by the tendency of the secondary particles to go in the forward-backward direction in the centre of mass. This led to the development of the peripheral model which allowed the quantum numbers to be exchanged with original directions being relatively unchanged.

A peripheral interaction is dominated by long range forces due to the exchange of a virtual particle. This generalizes Yukawa theory and is analagous to virtual photon exchange in electromagnetic interactions. Empirically the forward (backward) preference is observed only when the quantum numbers of the crossed t-channel correspond to some known meson (baryon). Thus the peripheral model considered the observed particles as the exchanged intermediaries.

However, models like the peripheral model involving the exchange of a particle of fixed spin J resulted in the violation of unitarity.

In Regge theory the spin of the exchanged particle is made a function of the four-momentum transfer i.e.

$$J \rightarrow \alpha(t)$$

This leads to an exchange of moving rather than fixed poles in the complex J - plane. With reference to Fig. 1.1 b, for $t > 0$, integer values of $\alpha(t)$ correspond to physical particles. With $\alpha(t) < 1$ in the scattering region ($t < 0$) for all exchanges, agreement with experiment is possible. This is the basis of the Regge pole model. The path followed by the moving pole is the Regge trajectory.

Hence the Regge and SU(3) classifications are somewhat complementary since the Regge poles which dominate high energy scattering exchanges also correlate the observed spectrum of hadronic states.

1.4 Crossing and Analyticity [5]

Crossing symmetry states that the three channels s, t, u representing reactions (Fig. 1.2), can be described by a single

s (direct)
$a + b \rightarrow c + d$ (i)

t (crossed)
$a + \overline{c} \rightarrow \overline{b} + d$ (ii)

u (crossed)
$a + \overline{d} \rightarrow \overline{b} + c$ (iii)

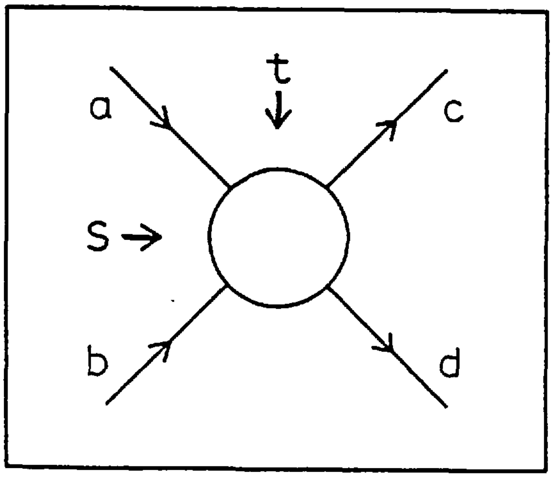

Fig. 1.2

function in s and t which represents the amplitude for these processes in the s and t physical regions appropriate for that process. However, as these regions do not overlap, the relationship is made by taking the physical amplitude to be the boundary value of an analytic function in complex s and t and which can then be continued from one region to another assuming the singularity structure is known.

Analytic functions are determined by the singularities they encompass. Mandelstam hypothesised that the only singularities of the invariant amplitude are poles and cuts (see Chapter 7) and that these singularities are connected to all possible intermediate states. This then determines the invariant amplitude. Thus what happens physically in one channel influences the behaviour of the amplitude in another channel.

1.5 Duality and Exchange Degeneracy (EXD) [7]

The development of duality increased the predictive power of the Regge pole model. The concept of duality results from the constraints imposed by analyticity and crossing symmetry through the technique of finite energy sum rules. This extended the influence of the Regge model to lower momenta where resonance formation is important. It was found that the direct channel resonances at low energy and cross-channel Regge poles at high energy provided, in an average sense, equivalent descriptions of the same phenomena.

Pictorially,

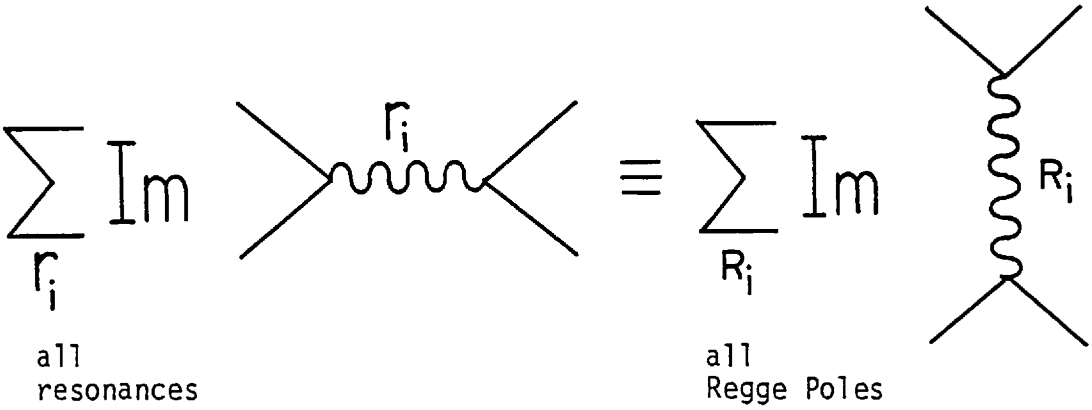

Fig. 1.3

To overcome the unacceptable vanishing of total cross-sections in exotic* channels, duality is expressed in two components.

If f is the scattering amplitude then:

Im f (resonance + background)= Im f (Regge poles + Pomeron)

Im f (resonance) = Im f (Regge Poles)

Im f (background) = Im f (Pomeron)

---

*Empirically, channels that cannot be classified as simple quark-antiquark or three-quark combinations have no established resonances and are said to be exotic.

In exotic channels we therefore have:

$$\text{Im } f \text{ (Regge Poles)} = 0$$

We cannot put all the Regge pole couplings equal to zero because then they would also vanish in the crossed channel which may not be exotic. This leads to the occurrence of Regge poles in exchange degenerate pairs (or more) such as to give purely real contribution to the scattering amplitude in the exotic channels.

EXD Regge poles have the same internal quantum numbers and identical trajectories.

EXD hypothesis can also be viewed as arising through the existence of exchange forces that make the dynamics of even and odd J different.[5] Thus two distinct sets of Regge poles will exist, characterised by a new quantum number called signature given by $(-1)^J$ for mesons and $(-1)^{J-\frac{1}{2}}$ for baryons. In the event of the exchange forces being non-existent or weak, we have the degeneracy of Regge poles having the same quantum numbers but opposite signatures i.e. EXD of Regge trajectories.

A good way to test EXD is to study a pair of line reversed reactions.

1.6 The Experiment [9]

This experiment was proposed primarily to conduct a high statistics study of Σ^+ and Y^{*+} production for incident π^+ and K^- beams, the reactions studied being:

$\pi^+ p \rightarrow K^+ \Sigma^+$ (I)

$K^- p \rightarrow \pi^- \Sigma^+$ (II)

$\pi^+ p \rightarrow K^+ Y^* (1385)$ (III)

$K^- p \rightarrow \pi^- Y^* (1385)$ (IV)

The allowed t-channel exchanges in these reactions correspond to $K^*(890)$ and $K^{**}(1420)$. At high energies these reactions are thought to be dominated by K^* and K^{**} Regge pole exchanges. Furthermore the K^* and K^{**} trajectories are expected to be exchange degenerate. A comparison of reactions (I) and (II), (III) and (IV) provides a simple test of EXD of K^* and K^{**} trajectories. At high energies and small $|t|$, EXD makes predictions on the differential cross-section and hyperon polarization in the above mentioned reactions.

Briefly these are:

a) differential cross-sections in I & II, III & IV should be equal,

b) either hyperon polarization should be zero (Strong EXD) or hyperon polarization should be equal in magnitude and opposite in sign for reactions I and II, III and IV (Weak EXD).

When this experiment was proposed (1974), the situation concerning the EXD of K^* and K^{**} trajectories was somewhat confused. Lower energy data showed strong violations of these predictions as the cross-section for the K^- induced reactions exceeded that from the π^+ reactions by a factor of 2 to 4. Higher energy data was of low statistical significance and the polarization measurement is important in extracting amplitudes. Also no experiment had studied the pairs of reactions I and II, III and IV in the same experimental setup. The resulting systematic uncertainties made the extent and the s dependence of the violation somewhat unclear.

The violation of EXD at low energies and data from other channels had shown the need for corrections to the basic Regge pole model. These corrections would tend to modify the EXD predictions.

Fig. 1.4 illustrates the data at around 4.0 Gev/c. It compares the differential cross-sections and the polarizations for the line-reversed reactions $\pi^+ p \rightarrow K^+ \Sigma^+$ and $K^- p \rightarrow \pi^- \Sigma^+$ around 4.0 Gev/c.

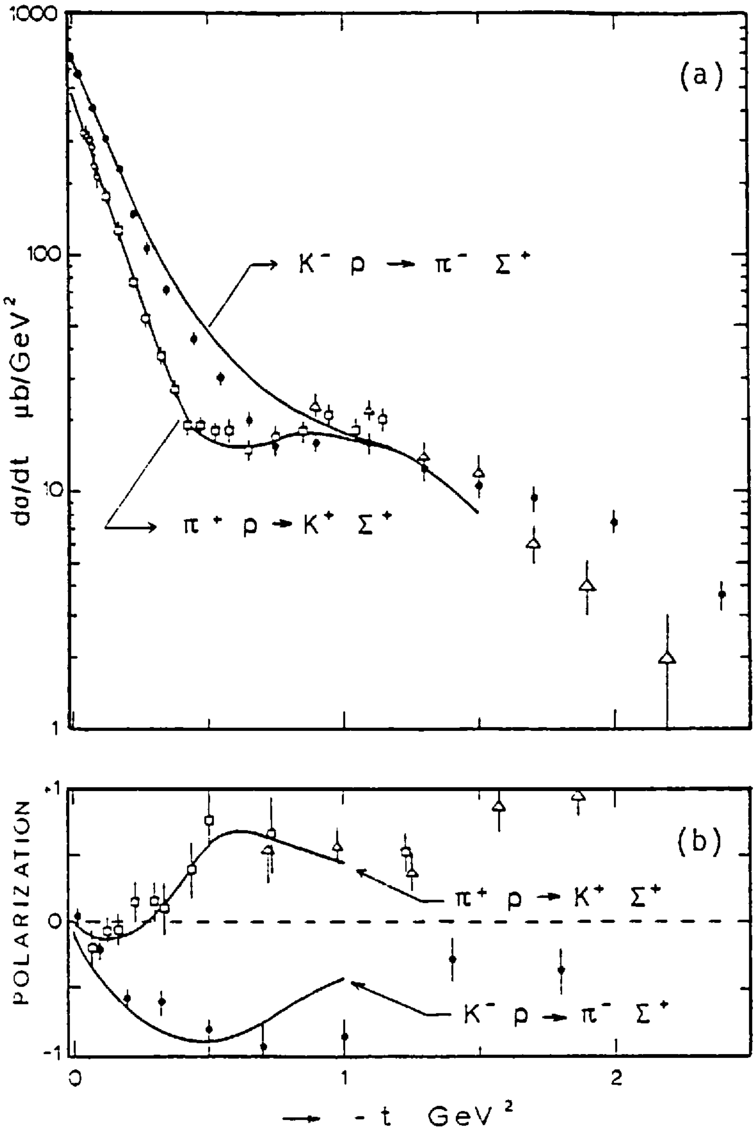

Fig. 1.4 Differential Cross-sections (a) and Polarizations (b) around 4.0 Gev/c.

Key Figure from reference

● 4.15 Gev/c $K^- p \to \pi^- \Sigma^+$ ref. 35

□ 4.0 Gev/c $\pi^+ p \to K^+ \Sigma^+$ ref. 32

△ 4.0 Gev/c $\pi^+ p \to K^+ \Sigma^+$ ref. 31

○ 4.25 Gev/c $\pi^+ p \to K^+ \Sigma^+$ ref. 29

At this energy the differential cross-sections for reactions (I) and (II) are certainly not equal. The polarization for $-t < 0.4\ (\mathrm{Gev/c})^2$ again disagrees with EXD although the disagreement with weak EXD for high $|t|$ is not large.

Previous experiments have indicated that Σ production is dominated by the spin non-flip amplitude while $Y^*(1385)$ production is dominated by the spin-flip amplitude. A high statistics, low systematic uncertainty study of Σ^+ and $Y^*(1385)$ production in reactions I - IV would enable us to examine the details of EXD violations.

1.7 The Choice of Technique

The cross-section for hypercharge exchange (HYCEX) reactions falls swiftly with increasing beam momenta. Thus a detailed analysis of these reactions at high energies would require a prohibatively large exposure in a conventional bubble chamber. Nevertheless, the bubble chamber is ideally suited for the examination of Σ^+ and Y^* resonances. The 4π observation capability enables most of the parity violating decays of Σ^+ and Λ^0 (both direct and from Y^*'s) to be clearly seen. Thus a good measurement of Σ^+ polarization, differential cross-sections and the Y^* density matrix can be made with a high statistics experiment in a bubble chamber.

The SLAC Hybrid Facility, comprising of a 1m rapid-cycling bubble chamber with its attendant electronic detectors upstream and downstream allowing particle identification was ideally suited for the study of the peripheral Σ^+ and Y^* production in reactions (I) to (IV). The fast forward going meson provided a simple trigger which resulted in an order of magnitude reduction in the required number of pictures. This made the present study feasible.

1.8 Data Taking

The Imperial College (IC) and the SLAC bubble chamber groups collaborated to set up the SLAC Hybrid Facility. The momenta at which the data were taken were chosen to be 7.0 Gev/c by IC and 11.5 Gev/c by SLAC. This allowed a reasonable spacing of energies to establish the energy dependence. Table 1.5 summarizes the data taking. Data at the two energies were analyzed independently.

	Beam	Period	Number of Pictures Taken x 1000
1.	π^+	Summer 1976	130
2.	π^+	Winter 1976	96
3.	π^+	Spring 1977	190
1.	K^-	Spring 1977	217
2.	K^-	Winter 1977	190

Table 1.1 Details of picture taking.

CHAPTER 2

The Experimental Setup and Description

2.1 The Beam

The 21 Gev/c primary electron beam is allowed to hit a (1.1 radiation length) beryllium target from which SLAC beamline 14 emerges. The primary beam is pulsed at rates up to 360 Hz with pulse duration of 1.6μs. The secondary beamline was designed to give up to 15 pulses/second with an average of 6 π^+ 's (4 K^- 's) per pulse at a momentum of 7.0 Gev/c. A single r.f. separator at the second focus was used in the K^- runs to achieve separation[12]. The K/π ratio obtained varied between 3 and 4. The layout of the secondary beamline is shown in Fig. 2.1.[14]

2.2 The SLAC Hybrid Facility[10,13]

The facility can be separated into three parts namely, the upstream system, the bubble chamber and the downstream system. Fig. 2.2 shows the layout of the facility.

2.2.1 The Upstream System

The two upstream plastic scintillators, S1 and BH, defined a beam particle. The threshold of the beam Cerenkov, CB, was such that only pions in the beam emitted Cerenkov light

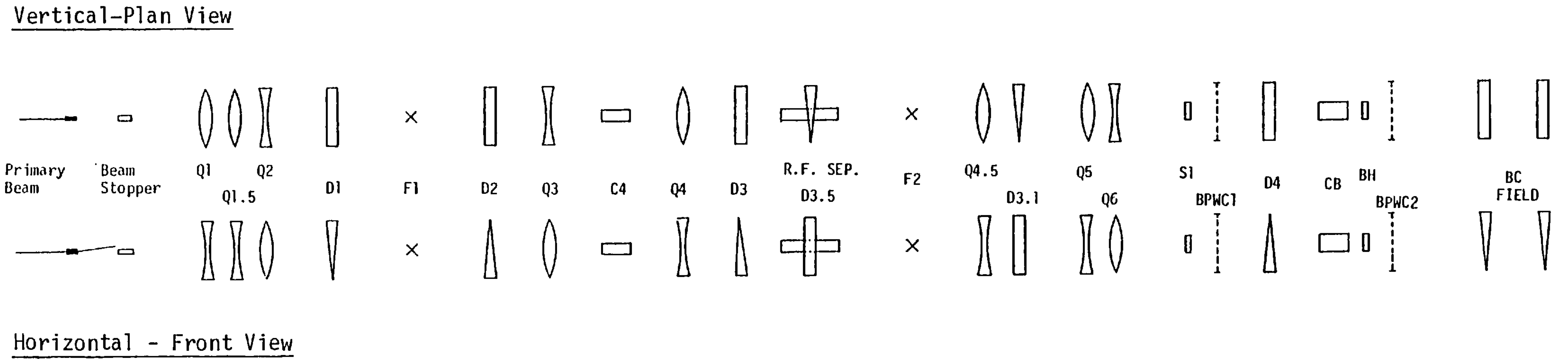

Fig. 2.1 SLAC Beamline 14

The secondary beam line emerged at 1^{o} to the horizontal. At the first focus, F1, there was a movable jaw collimator which selected a 25% momentum byte. The bending magnet, D3.5, was placed on the rf separator to aid separation. A 1% momentum byte selection was made at the second focus. The quadrupole magnets Q5 and Q6 made the beam parallel. The bending magnet, D4, aimed the beam for entry into the bubble chamber.

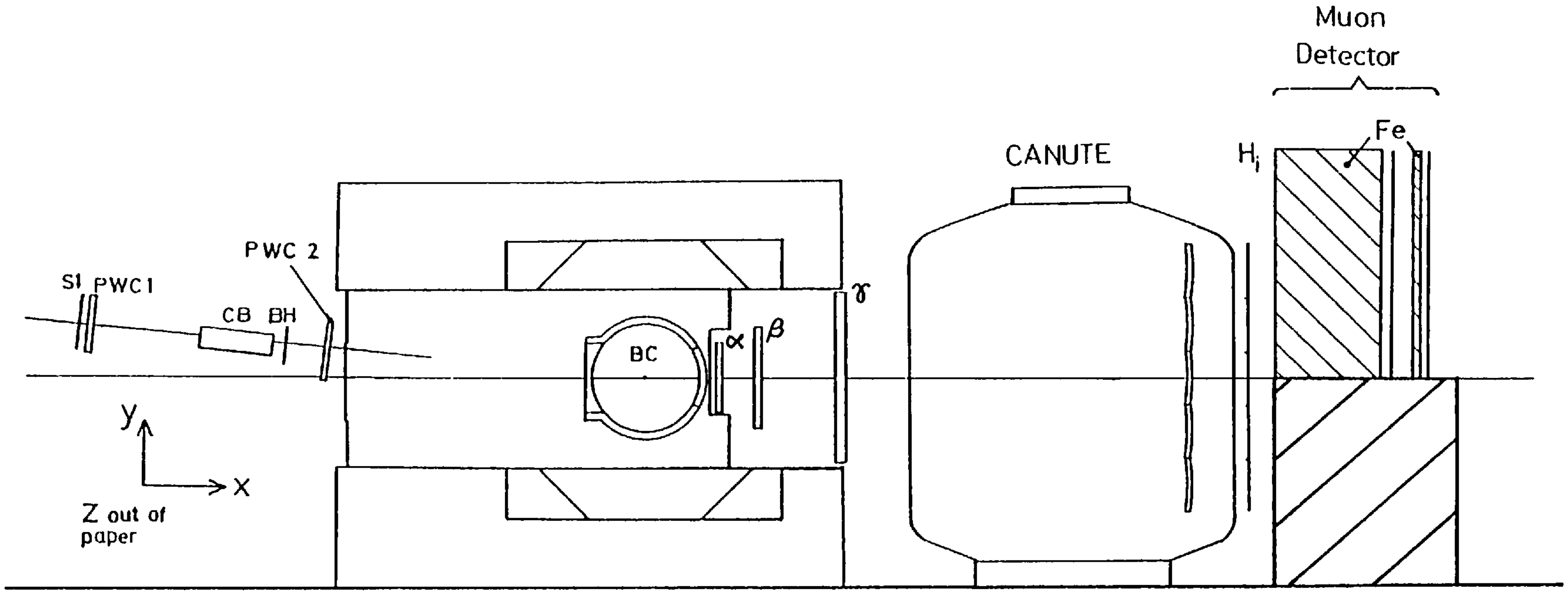

Fig. 2.2 Front View of the SLAC Hybrid Facility

The bubble chamber frame is such that the centre of the back of the front glass is (0, 0, 0). The centre of the chamber is (0, 0, - 25). The axes are shown at the bottom left. Dimensions are in cm.

(Table 2.2). Thus in the π^+ run light was demanded from CB while in the K^- run no light was demanded. Consequently, contamination of the beam by muons in the π^+ exposure, and $\bar{p}$ contamination in the K^- exposure, had to be allowed for (Chapter 5). The two beam multiwire proportional wire chambers (PWC), PWC 1 and PWC 2 defined the angle of entry into the bubble chamber and were also used in the software algorithm logic (cf 2.3.2). The details of the PWC's that were used are tabulated in Table 2.3.

2.2.2 The Bubble Chamber

The secondary beam was injected into the liquid hydrogen filled bubble chamber which acted both as a target and a detector. The principle features of the chamber are illustrated in Table 2.4.

Chamber Diameter	1 metre
Chamber Depth	43 cm
Pulsing Rate	10 - 15 Hz
Entrance & Exit Windows	1.5 mm Stainless Steel
Magnetic Field	18 Kg (Max 26 Kg)
Illumination	Bright Field (Piston covered with Scotchlite)
Camera Rate	2 Hz Maximum

Table 2.4 Details of the bubble chamber

Element	<x> cm	Dimensions cm (y x z) BC Frame	Other Details
S1	-899	25 x 25	
BH	-365	25 x 25	4 elements
Hodo	630	250 x 140	10 elements 50 x 70 Identical dimensions to CANUTE mirrors

Table 2.1 Details of the Scintillators.

Element	<x> cm	Length cm	Details
CB	-450	150	Pressure: Slightly above atmospheric Gas: Freon 12 Mode: Threshold Beam particles of π - mass or lower emit Cerenkov light
CANUTE	425	300	Pressure: 2.5 atmospheres Gas: Freon 12 Mode: Threshold Particles of π - mass above 1.9 Gev/c emit Cerenkov light

Table 2.2 Details of the Cerenkovs

	PWC	<x> cm	Dimensions (y x z) cm	Wire Plane Orientations
Upstream	BPWC1	-865	25 x 25	y x z
	BPWC2	-325	25 x 25	y x z
Downstream	α	77	72 x 22	y x u x z
	β	119	104 x 33	y x u x z
	γ	200	168 x 60	y x u x z

Table 2.3 Details of the multiwire proportional wire chambers.

There were 12 wires/inch. Wire planes were separated by 3.8 cm. In the downstream PWC's the diagonal wires (u - plane) form a 3: 4: 5 triangle with the others (36.9^0 to the horizontal).

Element	<x> cm	Thickness cm	Dimensions cm	Other Details
Iron	715	115	240 x 200	
Scintillator	785		240 x 200	12 elements (40 x 100)
Iron	811	9	240 x 200	
Scintillator	827		240 x 200	12 elements (40 x 100)

Table 2.5 Details of the muon detector.

2.2.3 The Downstream System

The downstream system which provided information on momenta, angles and masses of the outgoing particles, consisted of 3 proportional wire chambers, a large pressurized multicell Cerenkov counter, CANUTE, and a hodoscope array. The details of these elements are given in Tables 2.1, 2.2, 2.3. For the K^- run a muon detector (Table 2.5) was added downstream of CANUTE to eliminate false triggers from K^- muon decays.

2.3 The Trigger

The process of deciding whether or not to take a picture can be split into two stages.

2.3.1 The Fast Hardware Trigger

This decision was made by the fast electronics in approximately 20 nsec. The triggering signatures for the π^+ and K^- induced reactions were fast outgoing K^+ and π^- respectively. With reference to figure 2.2, the hardware trigger for π^+ induced reactions was:

$$S1 \,.\, CB \,.\, BH \,.\, \overline{CSUM} \,.\, \Sigma Hi \qquad \text{(i)}$$

and for K^- induced reactions it was:

$$S1 \cdot \overline{CB} \cdot BH \cdot CSUM \cdot \qquad \text{(ii)}$$

S1 . CB . BH defined a π^+ or μ^+ and S1 . $\overline{\mathrm{CB}}$. BH . defined an incident K^- or $\bar{p}$.

CSUM was the summed signal from all 10 elements of CANUTE.

ΣHi was an 'or' of all 10 elements of the hodoscope behind CANUTE.

So $\overline{\mathrm{CSUM}}$. ΣHi implied that a particle, which is either a K or a p went through the downstream hodoscope.

The background causing hardware triggers in addition to the wanted events was given largely by:

a) interactions in exit windows of the bubble chamber and the vacuum tank

b) interactions in the gas of CANUTE

c) low momenta outgoing particles

d) in the K^- run, decays of the beam particles.

In the π^+ exposure, condition (i) was satisfied by 1 in 25 beam tracks while in the K^- exposure condition (ii) was satisfied by 1 in 15 beam tracks.

The hardware trigger caused the PWC read out. This data, along with Cerenkov pulse heights and scaler data were stored in electronics. This took approximately 100 ns. Thus it was possible to read in a second hardware trigger in the same 1.6 μs beam spill. This reduced trigger dead-time losses.

After the second hardware trigger had been read in or at the end of the beam spill, the data was read into the computer via CAMAC in 200 μsec and a software algorithm was executed.

2.3.2 The Software Trigger Algorithm [11]

The object of the algorithm was to derive the interaction vertex and the momentum of the fast outgoing track which had caused the fast trigger. The maximum time allowed to decide whether or not to take a picture was given by the bubble growth. It was found that the algorithm took roughly 1ms. Since one still had approximately 1.5 ms before the bubbles grew large enough to be photographed, a second trigger, if there was one could be processed. The main steps in the execution of the trigger algorithm were:

a) multiplicity checks: both planes of PWC2 were checked for at least one, but no more than two hits. More than two hits in the beam planes caused the trigger to be rejected. If one of the PWC2 planes did not have any hits, the planes of PWC1 were similarly checked. If the latter gave a positive result, then faked hits were generated at PWC2. This was only possible because the beam was set up to be as parallel as possible.

With no information linking y and z in beam PWC's, considering more than 2 hits in each plane would have lead to spurious triggers as well as consuming time. A maximum of 5 hits (the first five) in the downstream PWC's were read out. Monte Carlo studies suggested that 5 was a large enough multiplicity, with accidentals included, for reaction channels of interest.

b) by using the tie-up condition,

$$4y + 3z - 5u = \text{const}$$

matched hits in PWC's α, β, γ, were found and saved for later use.

c) a pair of downstream PWC's, both with at least one matched hit was chosen.

d) beam tracks found in PWC2 were projected into the pair of downstream PWC's being used. The hit predictions were compared with the matched hits already found to remove beam interactions in CANUTE. This is equivalent to a small beam veto which effectively moved with the position of the particular beam track and caused a small loss of acceptance at very small $|t|$. (See Chapter 4 for details).

e) the non-bend plane was used to calculate the vertex position, which was the intersection of the beam trajectory and the trajectory formed by the z hits of the chosen pair of downstream PWC's. If the dip of the fast outgoing track was too small, the vertex position was imposed. If, taking into account the errors, the vertex was found not to lie in the fiducial volume, the trigger was rejected. So to a certain extent false triggers caused by interactions in the windows of the bubble chamber and the vacuum tank were rejected. The vertex position test also eliminated most false triggers caused by beam $K^- \to \pi^- \pi^0$ decays occurring outside the fiducial volume.

f) the calculated vertex position, the bend plane hits in the beam and the downstream PWC's were used to calculate the momentum of the outgoing track. A momentum lower than 2.5 (3.5) Gev/c caused the trigger not to be accepted in π^+ (K^-) exposures.

g) using the calculated momentum, the outgoing track was projected into the PWC so far unused and predictions were made for y, u and z hits. Confirmation was required from at least one of these before the trigger was accepted. This eliminated a majority of software triggers caused by associating hits from different tracks.

h) finally, if the pair of PWC's being used gave a negative result, the next pair of PWC's was tried, the procedure being repeated from step (c).

In the K^- exposure, the muon hodoscopes were examined before step (a) to eliminate triggers from K^- muon decays.

If the trigger algorithm generated a positive response, the computer sent a signal, along with various data for the picture box, to the bubble chamber to take a picture. The camera had a dead time of 0.5 secs.

A fixed length record of useful data (PWC hits, scintillator hits, Cerenkov pulse heights, scaler and picture box data) was written on a magnetic tape for every hardware trigger regardless of whether or not a picture was taken.

The software trigger reduced the acceptable number of hardware triggers by an order of magnitude. So the overall trigger reduced the picture taking rate to 1 in every 250 beam tracks or 40 bubble chamber pulses, thus reducing the film taken by an order of magnitude. The basic aim of the trigger was to achieve this reduction.

CHAPTER 3

The Event Processing Chain

3.1 Introduction

A charged particle when traversing through the liquid hydrogen of a bubble chamber leaves behind it a trail of ions. If now the pressure is suddenly dropped, with temperature held constant, the liquid becomes superheated allowing bubble formation at the ionization centres. By illuminating the chamber with flash lights and photographing it with three cameras, a stereoscopic recording of the charged particles taking part in interactions is obtained.

The electronic counter data and a set of 3 pictures represent the raw data for each event. The major steps in the processing[22] of an event are (see Fig. 3.1) scanning and measuring
geometrical reconstruction in space
kinematical reconstruction
hypothesis selection.

3.2 Scanning and Measuring

The purpose of scanning is to enable selection and classification of events to be measured. After scanning events were selected for measurement on the basis of the following criteria:

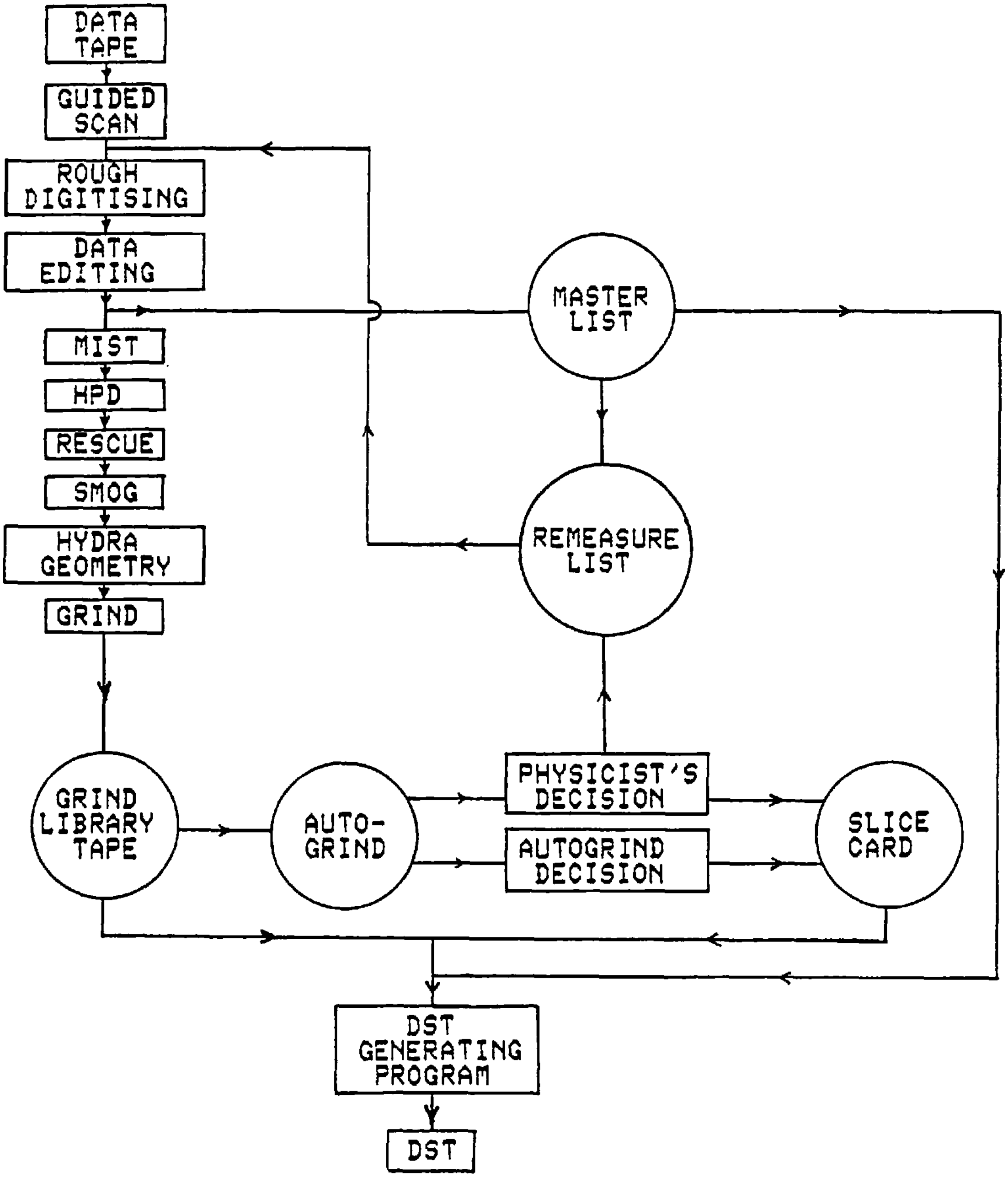

Fig. 3.1. The Event Processing Chain.

a) The interaction appeared to be on the beam which caused the picture to be taken. This was checked with the aid of a template positioned with respect to the fiducials as illustrated in Fig. 3.2. The parallel beam allowed the scale on the template to be normalised to the BPWC2 y hits (the Y2 number). The scanners were guided to look for interacting beams within a certain tolerance about the Y2 number. This meant that over a third of the interactions appearing on the film did not have to be measured.

b) The interaction vertex was not in region D (Fig. 3.2). This enabled the outgoing tracks to be sufficiently long for good measurement.

Initially all events which passed the above two criteria were measured. However, over most of the film only the events with visible strangeness were measured while the rest were recorded.

3.2.2 MIST-HAZE/RESCUE-SMOG [21]

A computer controlled device, the Hough Powell device (HPD) was used to measure the events. The HPD was run in the "road guidance" mode. This involved rough digitisation of the vertex, the middle and end of each track and two well separated fiducials on each of the three views. Program MIST assembled

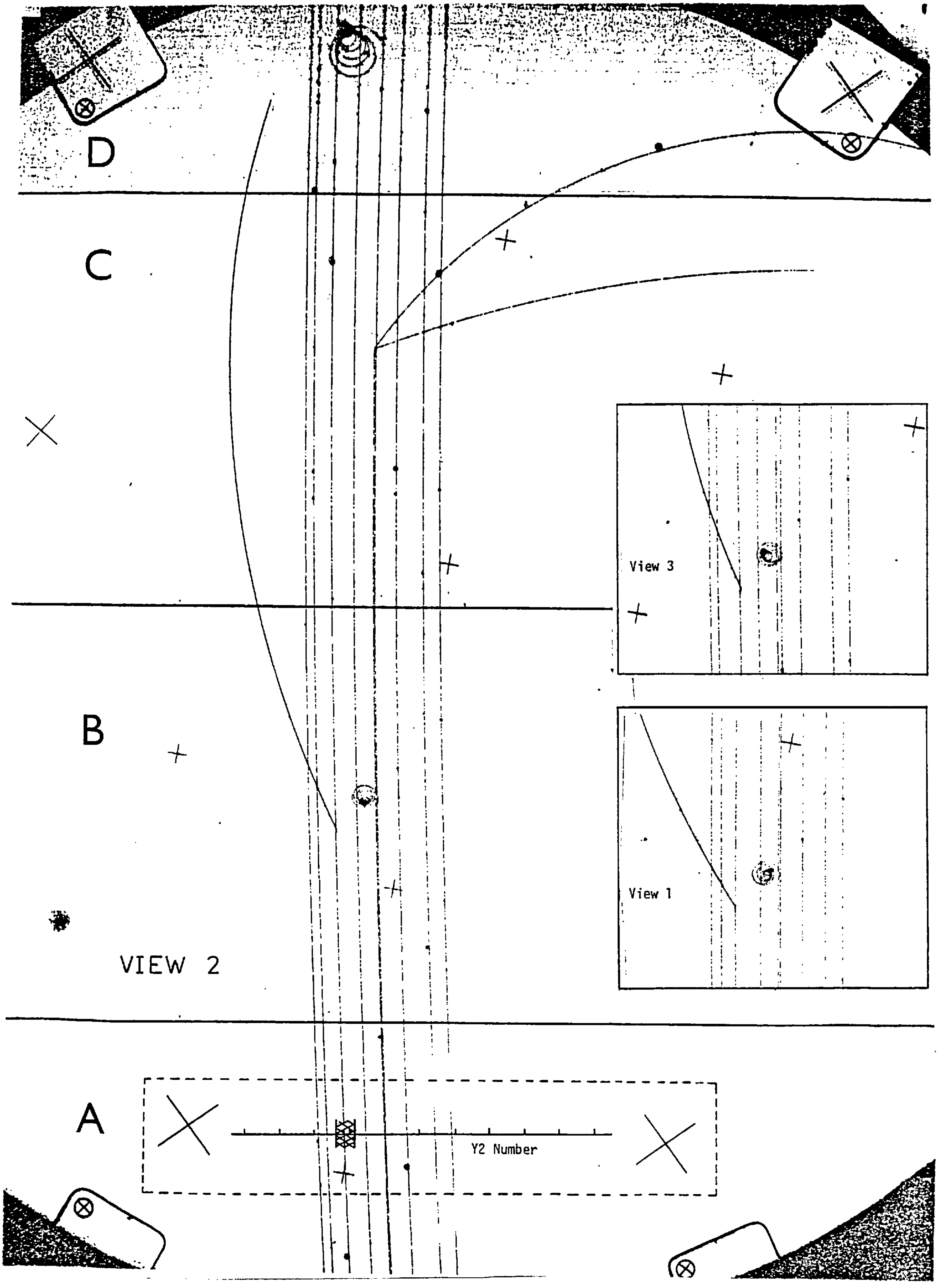

Fig. 3.2 Events in the SLAC Rapid Cycling Bubble Chamber.

The event of interest is the 2-prong with a kink. The insets show View's 1 and 3 of the event. The scan was performed on View 2. The dotted rectangle represents the template.

the data to be input into the HPD analysis program HAZE. This input data were used to create and update a book-keeping list, the Master-list. HAZE used the rough measurements to define a circular band, known as a road, of width between 0.5 and 1mm on film. The digitisings within the bands were used to calculate master points for the tracks. For each track the density of these digitisings was used to determine the ionisation, which later assisted in particle identification. The program RESCUE tried to recover events which had failed in HAZE. The program SMOG combined the HAZE/RESCUE output from the three views which then served as input to the geometry reconstruction program, HYDRA geometry.

3.3 Geometrical Reconstruction[23] and Hybridisation[19]

The object of a geometrical reconstruction program is to provide a three-dimensional description of events in bubble chamber space. For the principles the reader is referred to ref. 22.

Essentially the output consisted of spatial (x, y, z) coordinates of all vertices; momentum, dip and azimuthal angles (p, λ, ϕ) at the appropriate vertices and mass-dependent residuals for all tracks of an event. The residuals were useful in particle identification.

In the final part of the program, the beam and triggering track hybridisation was undertaken. The three-momenta and the well determined vertex position were used as starting values to swim the fast forward and beam tracks to downstream and upstream PWC's respectively. The appropriate hits were found and the track parameters were then adjusted to minimise the displacement to both bubble chamber and PWC points. The hybridised values were taken if the χ^2 was good. Otherwise the bubble chamber values were used. The improvement in the triggering track parameters, especially the momentum and dip, is illustrated in Fig. 3.3. a,b. In the π^+ induced reactions, only events which had a hybridised outgoing track and a hit in the hodoscope were used for physics analysis. This coupled with CANUTE having no light (a requirement of the hardware trigger), implied that the track could be confidently assumed to be a kaon or a proton. In the K^- induced reactions, a hodoscope hit was not demanded, but the hybridisation requirement, CANUTE having light and a negative signal from the muon counter implied that the outgoing track was probably a pion. This was important because at these high momenta neither ionisation nor track residuals can help in particle identification.

3.4 Kinematical Reconstruction

The object here was to obtain a physical interpretation of the event in terms of the participating particles and their three-momenta. The determination of the masses and quantum numbers of the particles was carried out using the conservation constraints of energy-momentum and the relevant quantum numbers.

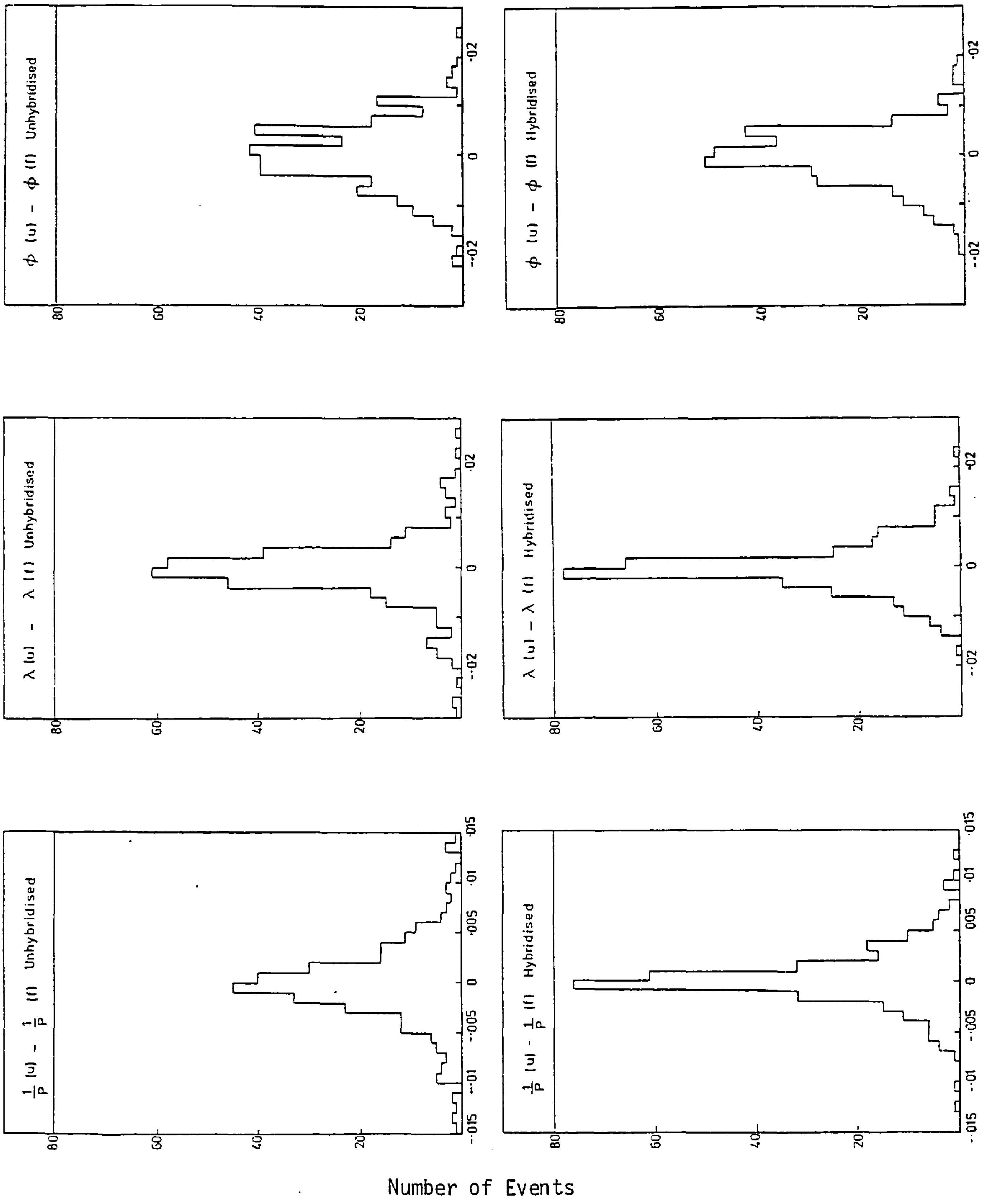

Fig. 3.3a The triggering track parameter pulls in 7C multivertex fits for the reaction $\pi^+ p \rightarrow K^+ \Lambda \pi^+$.
The case where hybridisation of the triggering track was attempted is compared with the case where bare bubble chamber measurements were used. (Units are Gev/c, radians).

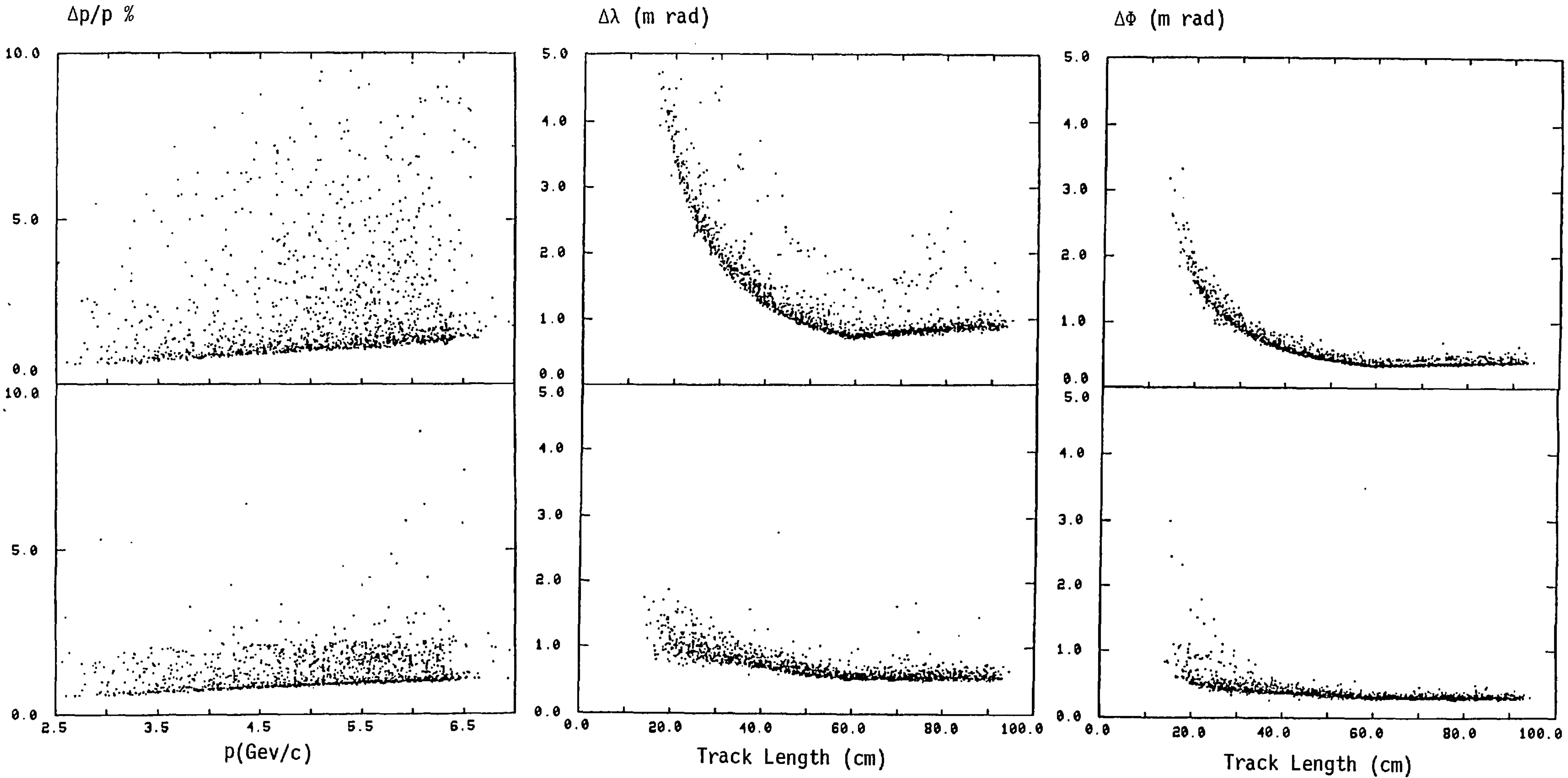

Fig. 3.3b. The Error Distributions for the fast track before and after hybridisation

For a given topology, a complete set of possible mass permutations of the final state particles, satisfying the quantum number conservation laws was compiled and used to setup the kinematics program GRIND to process the HYDRA Geometry output.

3.4.1 Some Details of GRIND [24]

The input data was initially read into GRIND banks and prepared in the form required for kinematic fitting. The major steps are outlined below:

a) The quality of the measurement of track parameters was determined

b) The measured beam track parameters were weighted with those of a standard beam track, taking due account of errors. The weighting was given by [24A]

$$<\underline{X}> = \left[\frac{\underline{X}\text{meas}}{(\underline{\Delta}\text{meas})^2} + \frac{\underline{X}\text{std}}{(\underline{\Delta}\text{std})^2}\right] \Bigg/ \left[\frac{1}{(\underline{\Delta}\text{meas})^2} + \frac{1}{(\underline{\Delta}\text{std})^2}\right] \quad \text{(i)}$$

where $X \equiv (\frac{1}{p}, \lambda, \phi)$, $\Delta \equiv$ errors on $\underline{X}$, and meas, std $\equiv$ measured, standard.

The standard beam track was parameterised from long well determined beam tracks. Essentially, the weighting affected the shorter unhybridised beam tracks. The errors on the standard beam track, as well as all other tracks, were adjusted until the stretch functions had the expected form. The stretch function is a standard normal distribution function with the standardized variable

$$Z = \frac{Xm - Xf}{\sqrt{\Delta^2(Xm) - \Delta^2(Xf)}}$$

such that (ii)

$$f(Z) = \frac{1}{\sqrt{2\pi}} e^{-z^2/2}$$

where Xm, Xf represent the measured and fitted track parameters. Equation (ii) thus implies that for variables having Gaussianly distributed errors, Z has a normal distribution centred on zero and a standard deviation of one. Since the parameters($\frac{1}{p}$, λ, ϕ,) had nearly Gaussian errors, a realistic estimate of errors was obtained by examining the stretch distributions in four-constraint fits. These are illustrated in Fig. 3.4.

c) The next step was to test various hypotheses corresponding to the topology of the event. The track parameters were varied, within errors, to obtain a fit which satisfied the energy-momentum constraints to a preset accuracy. A chi-squared probability for the fit, which reflected the required amount of variation of the parameters, was then computed. More details of the fitting sequence for a two pronged event with a charged decay (kink) are given below.

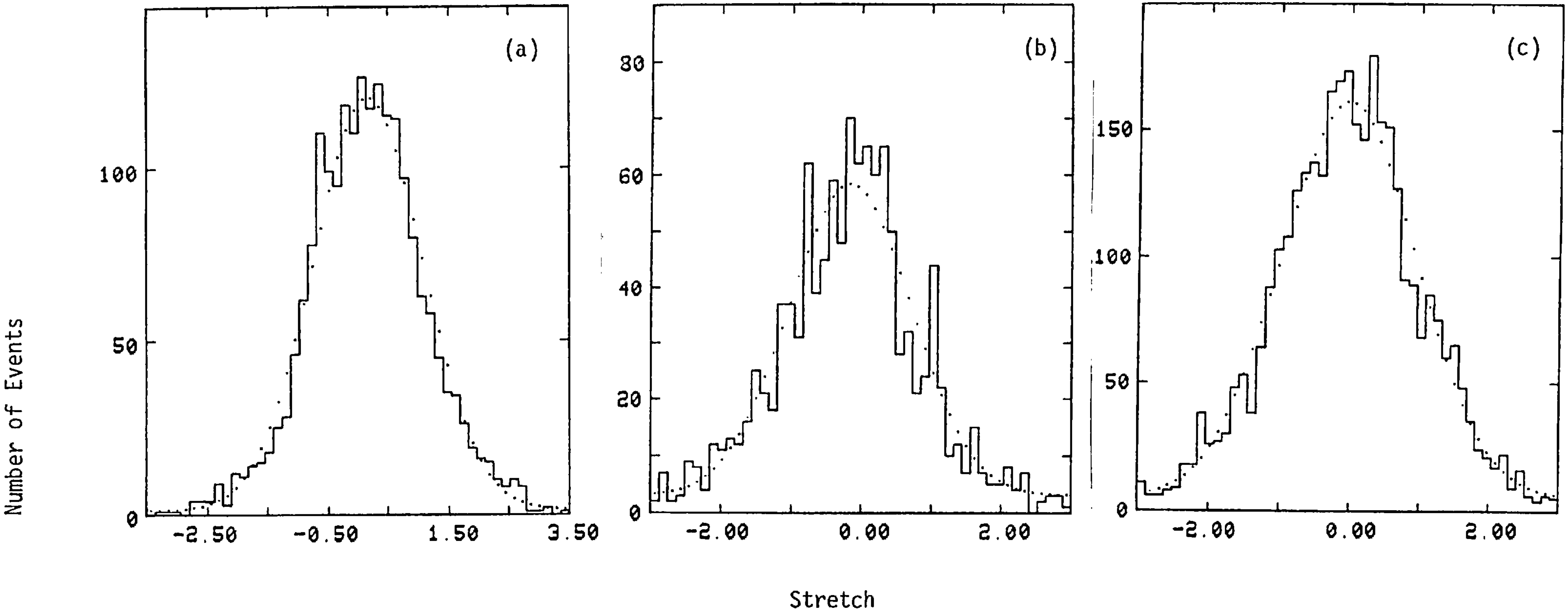

Fig. 3.4 Some sample stretch distributions

(a) $K^-p \rightarrow \pi^-\Sigma^+$ Fast track $\frac{1}{p}$ stretch.

(b) $\pi^+p \rightarrow 4$ prongs, unique 4C fits. Beam track λ stretch.

(c) $\pi^+p \rightarrow 4$ prongs, unique 4C fits. Slow tracks (< 2.5 Gev/c) ϕ stretch

d) Finally, the results of the fits were written onto a tape (the GRIND Library Tape, GLT) which served as input to AUTOGRIND, a hypothesis selection program.

3.4.3 The Fitting Sequence for a 2-Prong event with a Charged Decay

The fitting sequence for a two pronged event with a charged decay (Fig. 3.5)

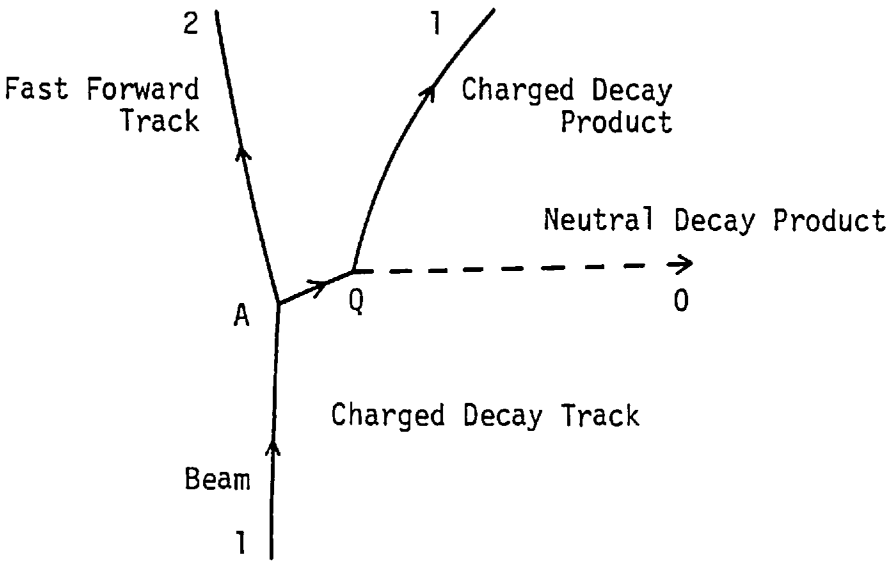

Fig. 3.5 A 2-prong event with a charged decay.

proceeded as follows:

a) a Mono-vertex fit at Q

There were two categories to be considered. Firstly when AQ was short and straight implying that the momentum was not measured and secondly when AQ was long and curved such that all three parameters ($\frac{1}{p}$, λ, ϕ,) were measured.

In the former case, which often occurred for the Σ^+ decays, the unmeasured parameters at vertex Q were 4 (3 for the neutral decay track Q0 and 1 for the momentum of the parent track AQ). Thus with 4 unknown parameters and with 4 constraint equations, only a solution for the unknown parameters was possible. This is referred to as a zero-constraint fit (0 C-fit).

In the latter case all but the Q0 track parameters were known resulting in a 1C-fit.

b) a mono-vertex fit at A

The results of the mono-vertex fit at Q, if successful, for the track AQ were now used as starting values to obtain a 4 C-fit at the production vertex, providing the beam and the fast track (A2) were well measured.

c) a multi-vertex fit at A and Q

Upon success in the mono-vertex at A, a simultaneous fit at both vertices A and Q, using the local energy-momentum constraints was carried out.

3.5 Modifications to GRIND

A systematic failure of events with short Σ^+s to achieve satisfactory mono-vertex fits at point Q neccessitated modifications to the fitting sequence outlined above.

The errors on the dip (λ) and azimuthal angle (ϕ) of a straight track connecting two points A and B with errors $\Delta\underline{x}_A$, $\Delta\underline{x}_B$ are given by

$$(\Delta\lambda)^2 = \frac{1}{L^2} \sin^2\lambda(\sigma_{xx} + \sigma_{yy}) + \cos^2\lambda\, \sigma_{zz}$$

$$(\Delta\phi)^2 = \frac{1}{L^2\cos^2\lambda} \sin^2\phi\sigma_{xx} + \cos^2\phi\sigma_{yy}$$

where L is the length of the track

and $\underline{\sigma}_{rr}$ $r = x, y, z$ are $(\Delta\underline{r}_A)^2 + (\Delta\underline{r}_B)^2$

These errors will be large if

(i) the connecting track is short

(ii) one or both of the points are badly measured.

The vertex A was usually well determined. Its point reconstruction involved a good rough measurement of the clearly defined production vertex at the measurement table and well determined tracks A1 and A2. In general, this was not true for vertex Q. Here, with a relatively suspect rough measurement of point Q (especially for the protonic Σ^+ decay mode) and with only one good track (Q1), Q point reconstruction tended to be inaccurate.

Over three-quarters of the eventual $\pi^+p \rightarrow K^+ \Sigma^+$ and $K^- p \rightarrow \pi^- \Sigma^+$ events on the DST had Σ^+ length below 2 cm as is illustrated in Fig 3.10. Thus the two conditions (i) and (ii) meant that the majority of Σ^+ tracks (AQ) were badly determined. This, as is shown below, affected fitting at vertex Q.

3.5.1. Details of the OC fit of a charged decay (eg. Σ^+) [248]

The object of the OC fit is to ascertain the momentum of the short Σ^+ track. Energy-momentum conservation yields a quadratic equation in P_Σ, the sigma momentum, of the form (with ref. to Fig. 3.6) given overleaf.

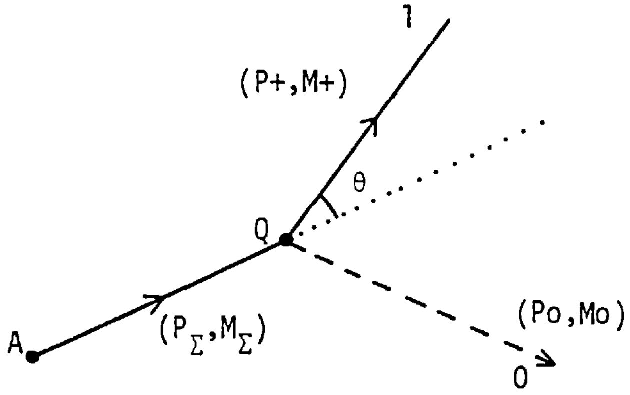

Fig. 3.6 Kinematics of Σ decay.

$$4(P_+^2 \cos^2\theta - E_+^2)P_\Sigma^2 +$$
$$4\,\Delta P_+ \cos\theta\, P_\Sigma - 4\,E^2\,M_\Sigma^2 + \Delta^2 = 0$$

where $\Delta = (M_\Sigma^2 + M_+^2 - M_0^2)$

and (P,M) are momentum and mass of $(\Sigma,+,0)$ the sigma, positive and neutral decay products respectively.

There are two types of solutions possible:

(i) the physical one: here the discriminant is positive yielding two values for P_Σ

(ii) the unphysical one: here the discriminant is negative yielding complex values for P_Σ.

In the physical case, both values of P_Σ are tried in the production mono-vertex fits. The starting values of AQ in these fits are the parameters obtained in the OC fit, modified for energy loss.

The unphysical solution arises primarily due to measurement errors on track AQ. The negative discriminant leads to

$$P_+^2 \sin^2\theta > \frac{\Delta^2 - 4M_+^2\,M_\Sigma^2}{4M_\Sigma^2} = P^{*2}$$

where P* is the momentum of the decay product in Σ^+ rest frame. Thus the unphysical solution implies that the measured transverse momentum of the positive decay track (w.r.t. Σ^+ track) is greater than the maximum allowed one.

This defect is recognised in standard GRIND and a recovery procedure (E SUBCL)[24c] is incorporated. Both the AQ and Q1 track parameters are altered so as to pull the transverse momentum of Q1 below the maximum allowed value by a least squares method. As remarked earlier, this procedure was not adequate in getting satisfactory 0 C fits, especially when dealing with the very short AQ tracks.

The reason is that the measured parameters of both AQ and Q1 are changed while the error is predominantly in the AQ track as was discussed earlier. In order to reflect this, the fitting sequence outlined in 3.4.3. was changed.

3.5.2 The New Fitting Sequence for $\pi^+ p \rightarrow K^+ \Sigma^+$ and $K^- p \rightarrow \pi^- \Sigma^+$

The changes to the fitting sequence were only valid for $\pi^+ p \rightarrow K^+ \Sigma^+$ and $K^- p \rightarrow \pi^- \Sigma^+$ reaction channels (i.e. no missing particles were involved).

Each two prong kinked event was processed at least twice and sometimes three times. The first pass was the GRIND pass with normal geometry input. A pass was taken to be from the stage of geometry input being read in to the results of fits written onto the G.L.T.

In the second pass, the geometry input record was modified such that tracks AQ and Q1 became totally unmeasured. The state shown in Fig. 3.7, with only the beam and the fast track now existed.

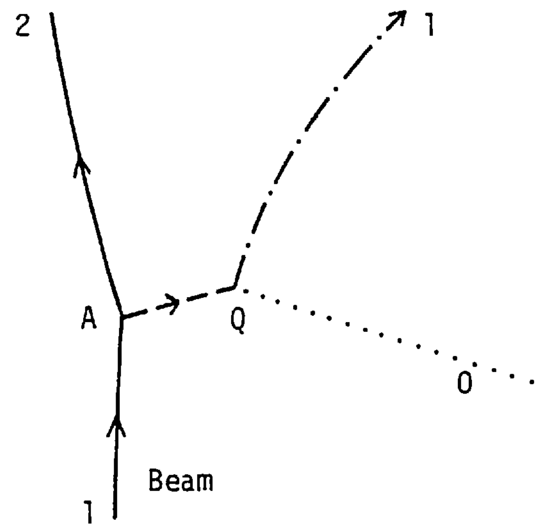

Fig. 3.7 A 2-prong 'kinked' event in second pass.

Therefore no mono-vertex fitting at Q could take place. Thus the only useful fits were 1C fits at the production vertex. Almost all of the eventual $\pi^+ p \rightarrow K^+ \Sigma^+$ and $K^- p \rightarrow \pi^- \Sigma^+$ events on the DST had track A2 hybridised. As stated earlier, this meant that it most probably was a kaon or a proton in the π^+ induced reactions and a pion in the K^- ones. Over half of the beam tracks were also hybridised. As shown in Fig. 3.3 the track parameter errors on hybridised tracks were considerably smaller than those expected from a bare bubble chamber. Thus the error on the missing mass against the K^+ in the π^+ exposure and the π^- in the K^- exposure was relatively small. This coupled with the ability to identify the A2 particle meant that the 1C $\pi^+ p \rightarrow K^+ \Sigma^+$ and $K^- p \rightarrow \pi^- \Sigma^+$ fits could be regarded with high confidence, particularly as the slow track was known to decay. The only serious contamination would have arisen from events which really were $\pi^+p \rightarrow K^+ \Sigma^+ \pi^o$ / $K^- p \rightarrow \pi^- \Sigma^+ \pi^o$ eg. if a Y* (1385) recoiled against the fast particle which then decayed to give a Σ^+ or if the final state originated from $K^*(890)$ Σ^+ intermediate state.

For the events of the type $\pi^+p \rightarrow K^+ \Sigma^+/K^- p \rightarrow \pi^- \Sigma^+$ that reached the DST, the recoil mass (against the K^+ and π^- respectively) distributions were examined. As can be seen from Fig. 3.8 no evidence for a significant Y*(1385) can be seen.

To examine the contamination from K* (890) $\Sigma^+/\rho^-\Sigma^+$ channel, Monte Carlo events of the reactions were generated. The decay angular distribution of the vector meson corresponded to that for a natural parity exchange process. The $(\Sigma^+\pi^o)$ effective mass distribution was then examined (in conjunction with Fig. 3.8). The mass distributions illustrated in Fig. 3.9 do not suggest that any sizeable contamination would arise from vector meson production.

No further processing of the event was undertaken if a successful 1C fit had not been obtained.

The 1C fit direction parameters with errors for the Σ^+ were now used as starting values for the track AQ. In mono-vertex fits, the track parameters used were the ones at that particular vertex. So, for the monovertex fit at Q, the Σ^+ track parameters were modified for energy loss and curvature using the momentum as determined in the 1C-fit. In the fitting itself, the Σ^+

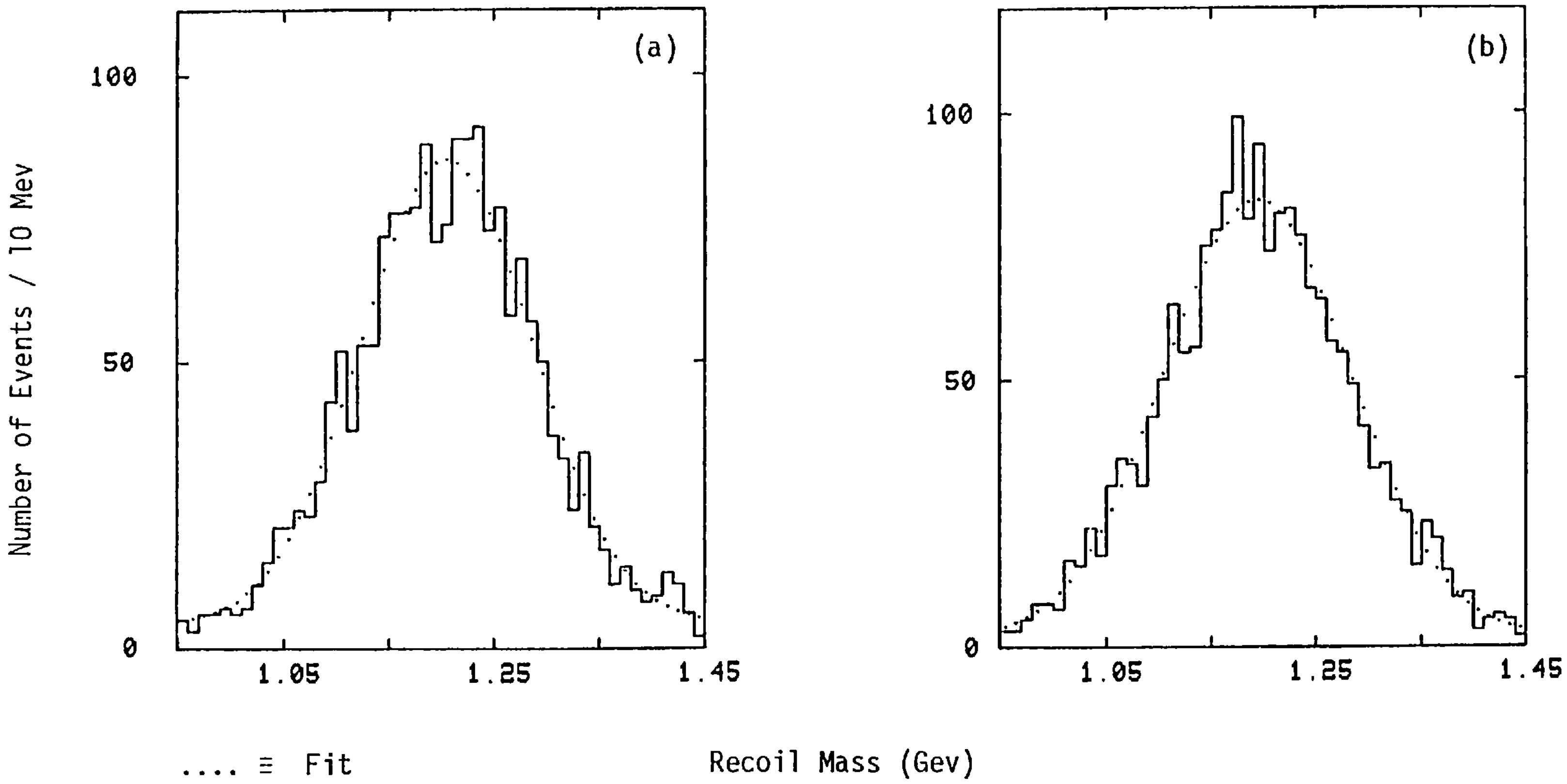

Fig. 3.8 The Recoil Mass Specturm against the Trigger Particle

a) Channel: $\pi^+ p \rightarrow K^+ \Sigma^+$ Parameters of Fit: $\langle M \rangle = 1194.0 \pm 3.1$, $\sigma = 88.0 \pm 3.0$ Mev

b) Channel: $K^- p \rightarrow \pi^- \Sigma^+$ Parameters of Fit: $\langle M \rangle = 1201.0 \pm 4.2$, $\sigma = 81.0 \pm 3.0$ Mev

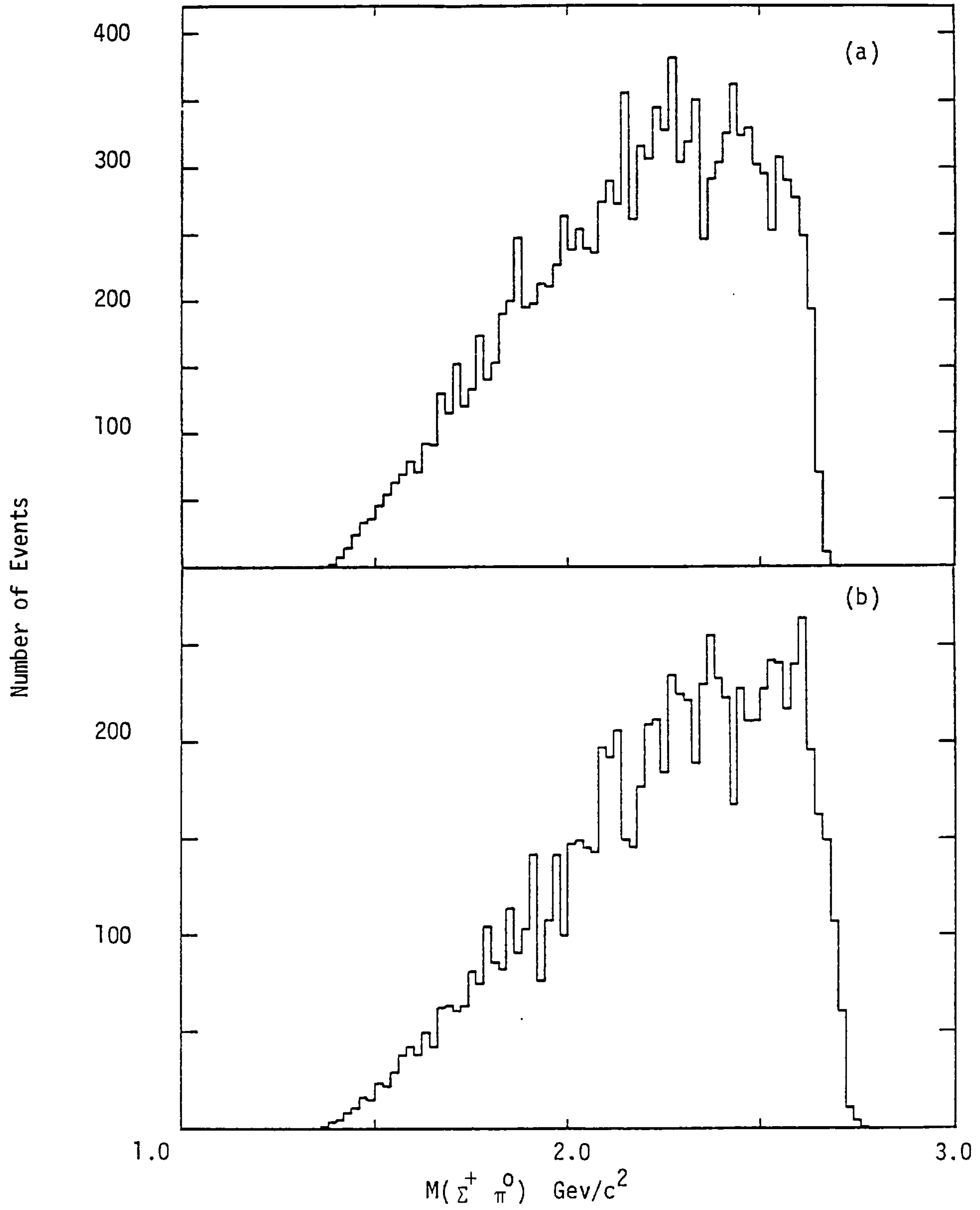

Fig. 3.9 The ($\Sigma^+\pi^0$) effective mass distributions.

(a) $\pi^+ p \rightarrow K^{*+} \Sigma^+$: Final State $K^+ \pi^0 \Sigma^+$

(b) $K^- p \rightarrow \rho^- \Sigma^+$: Final State $\pi^- \pi^0 \Sigma^+$

40,000 Monte Carlo events were generated. The plots contain events which had geometrically acceptable K^+/π^- tracks.

momentum was set as unknown. Thus all the modifications took place in the geometry input record. The subsequent fitting procedure was identical to the one used in the first pass. Therefore, fits at both vertices Q and A still had to be obtained before the final multivertex fit was tried. This meant that almost certain $\pi^+p \rightarrow K^+ \Sigma^+$ / $K^- p \rightarrow \pi^- \Sigma^+$ at the end of the third pass.

As a check on the new procedure, the results of multivertex fits for events which had successful first and third pass fits were compared. The differences in the final fitted parameters were very small.

The beneficial effect of this new procedure is illustrated in Fig. 3.10. As can be seen, most of the recovered events had Σ^+ length smaller than 1 cm. The throughput efficiency for reactions $\pi^+p \rightarrow K^+ \Sigma^+$ and $K^- p \rightarrow \pi^- \Sigma^+$ was considerably improved, especially in the low $|t|$ region (c.f. Fig. 3.11) where experiments using purely electronic counters experience difficulties.

With a few modifications this procedure was also used to recover events where the Σ^+ decay had been missed by the scanners so that the events were wrongly classified as two prongs. An example of such an event is illustrated in Fig. 3.2. As mentioned in 3.2, only on a small part ($\sim$20%) of the π^+ exposure were all the events

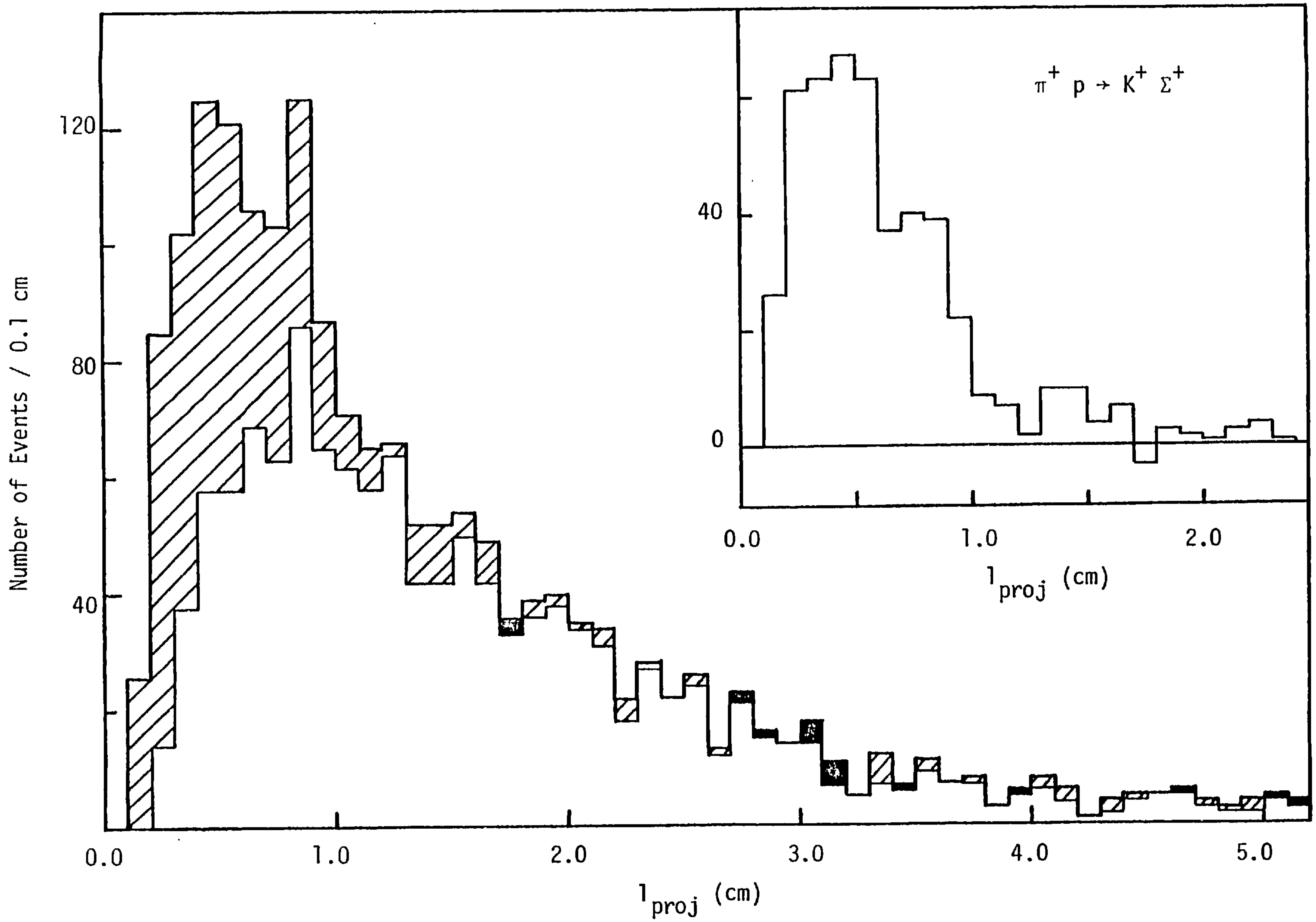

Fig. 3.10 The Σ^+ projected length distribution for first (unshaded) and third pass events (see text). The inset shows the recovered events (lined shaded in main plot). The solid shading shows events which did not get a fit in the third pass.

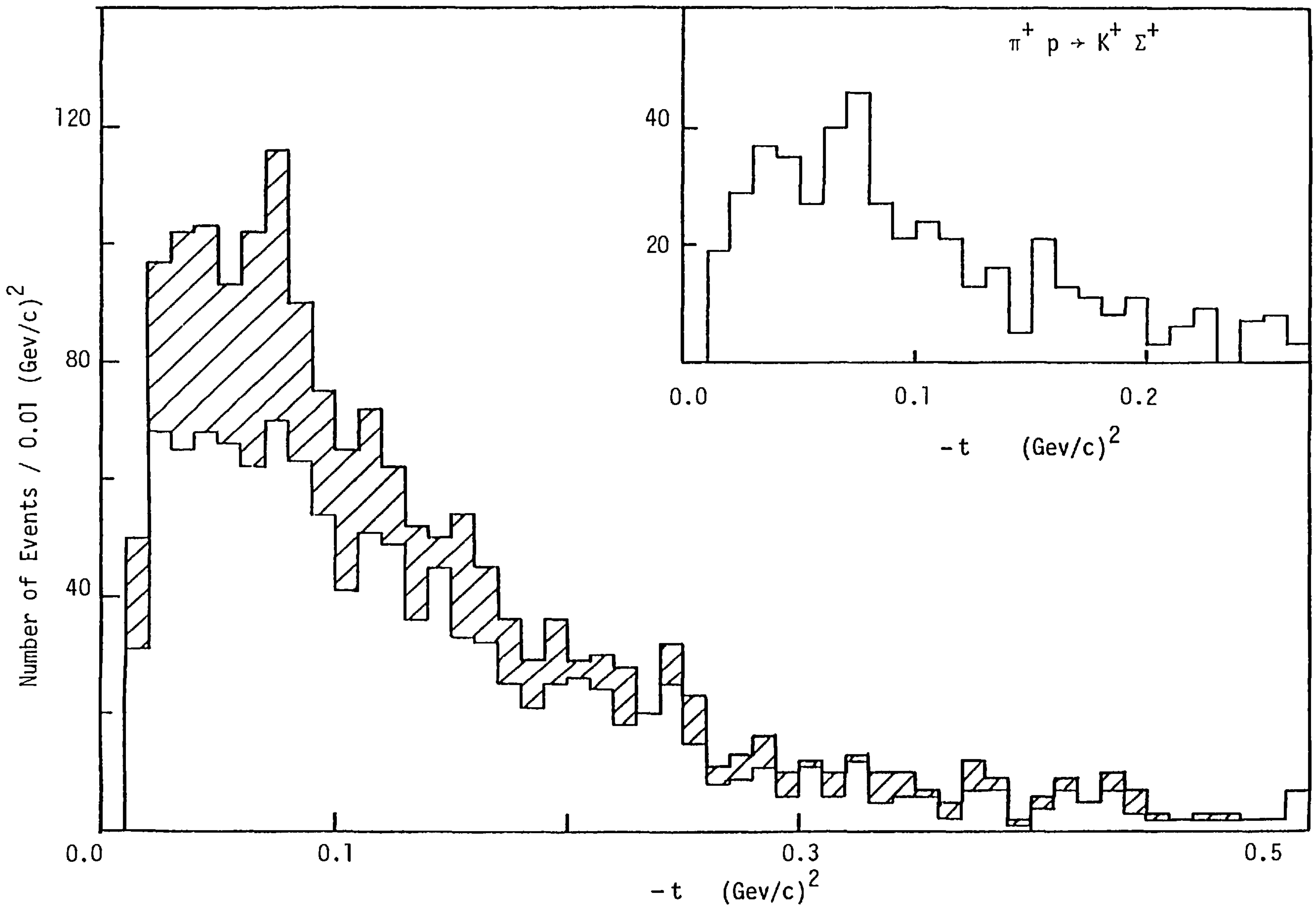

Fig. 3.11 The t distribution for first (unshaded) and third pass events (see text). The inset shows the recovered events (line shaded in main plot).

measured. On the K^- exposure only the events with visible strangeness were measured. Thus, due to systematic problems and the small number of events that were recovered from the two prongs data sample, no attempt to merge the recovered events and the events with a visible kink was made.

3.6 AUTOGRIND[25] - Hypothesis Selection to DST

Due to their peculiar configuration, hypothesis selection for the two prong events with a charged decay relied mainly on kinematic fits. This was due to the fact that the ionisation measurements were only useful in identifying the decay mode.

An automatic decision in AUTOGRIND was made if,

a) the non-decaying track had a momentum greater than 3.0 Gev/$_c$ in the π^+ exposure and 3.5 Gev/$_c$ in the K^- exposure. Downstream hybridisation of the track was also required.

b) the measurement of the event was acceptable. This was done by examining the mass-fit residuals of the participating tracks.

c) a good unique 4-C multi-vertex fit was present in the third pass.

d) no ambiguities in the decay mode existed.

All remaining events were examined on the scanning table. Most of the ambiguities arose in the decay mode which were easily resolved by ionisation and residuals information on track Q1. The level of ambiguity was considerably reduced when the fast outgoing track hybridised. Thus the fast forward track could be identified with high confidence (cf. 3.3), something which is not possible to do in a bare bubble chamber. In the events where the ambiguities could not be resolved, all the kinematic fits consistent with the ionisation and residuals information were accepted.

For each event the decision was output in the form of a card image (the SLICE card). Essentially, this had the roll/frame/event number, the hypothesis identification number and the event status information eg. remeasure, reject event etc. These cards were now used, in conjunction with the G.L.T. and the Master-List to prepare a DST for physics analysis.

CHAPTER 4

Corrections I

4.1 Introduction

This chapter deals with three kinds of geometrical and/or kinematical losses, namely:

a. scanning losses

b. geometric acceptance

c. algorithm acceptance.

These losses are systematic and ways of correcting for them are discussed. Briefly the corrections are made by weighting the events which are left after certain cuts on the data are made. The cuts are such that the remaining events are in a region where the detection efficiency is known. The weight is then the inverse of the detection probability. In this way a truer number of events in the data sample is obtained.

4.2 Scanning Losses - Length

Almost all the events of reaction types I and II have a 'kink' on the hyperon track. The scanning losses are due to certain geometrical or kinematical configurations of the 'kink' which make the recognition of this topology difficult on the part of the scanner.

The main reasons that the scanner misses events are:

a) the length of the Σ^+ track is short. It may also happen, though rarely, that the decay of the Σ^+ occurs outside the visible volume of the chamber

b) the observed decay angle between the Σ^+ track and its charged decay product is small. Σ^+ decays with slow charged decay products may also be missed.

The cuts on the data can be applied in two ways:

a) in some cases a cut on the appropriate parameter is made such that the chosen events are assumed to have 100% detection efficiency

b) alternatively, an efficiency function may be defined when the detection probability is parameterised in regions where it is no longer 100%.

The errors on measurements such as differential cross-sections are inversely proportional to the square root of the number of events actually used. Thus it is important to optimize to a maximum the number of events used for weighting.

Although fewer events are discarded when using method (b), the efficiency function is poorly determined unless one has high statistics at low detection probabilities. In general one has limited number of events. This introduces errors in the final results which are dependent on the choice of the efficiency function. The poor determination of an efficiency function is illustrated by the inset to fig 4.2.

To correct for the above mentioned losses, the most straightforward method is to make the cuts on the space variables such as Σ^+ length. Since the scanning is done using projections of the tracks, a more realistic method makes cuts on the projected variables. The projection onto the x - y plane in the bubble chamber frame is normally used.

The method using cuts on projected variables was found to be the most suitable and was thus used.

4.2.1 Length weighting

The length correction was applied by cutting away all the events where the projected length of the Σ^+ track was smaller than lmin, the minimum cutoff length, or greater than lmax, the maximum cutoff length.

The weight was given by (see Appendix 1.1).

$$Wi = \frac{1}{e^{\left(-\frac{l\min}{\eta(p)\cos\lambda}\right)} - e^{\left(-\frac{l\max}{\eta(p)\cos\lambda}\right)}} \qquad \text{(i)}$$

where $\eta(p)$ is the mean free path length.

lmin was determined in two ways:

a) it was given by the minimum value of the projected length cut at which the total weighted number of events became independent of the position of the cut. (cf Fig. 4.1). A plateau was not obtained in channel $K^-p \to \pi^-\Sigma^+$ with $\Sigma^+ \to n\pi^+$. Some $\Sigma^+ \to n\pi^+$ decay mode data were re-examined but no serious mis-assignments were noticed. On event to event basis a probability cut of 2% as to whether the Σ^+ would have decayed with a length greater than the length it had was imposed and the plateau behaviour was then observed as in Fig. 4.1.

b) the data sample was split into small Σ^+ momentum intervals and the number of events which had Σ^+ lengths in the range

$$1.0\text{cm} < l\text{proj} < 6.0 \text{ cm} \qquad \text{(ii)}$$

in each interval was determined.[20] The method described above showed that the detection probability in this range was one. Then events were generated for each interval such that the momentum was equal to the average momentum of the interval, and the number falling in the range (ii) was equal to that determined from the data sample. Summing the Monte-Carlo Σ^+ projected length distributions for all intervals gave an expected length distribution normalized to the range (ii). This is shown as the solid line in Fig. 4.2. The cutoff was taken to be the point where the experimental distribution started deviating from the theoretical one. This is better illustrated by the inset to Fig. 4.2.

Fig. 4.3 shows the length weight distribution w.r.t. the Σ^+ momentum.

Table 4.2 shows the Σ^+ projected length cutoffs that were used.

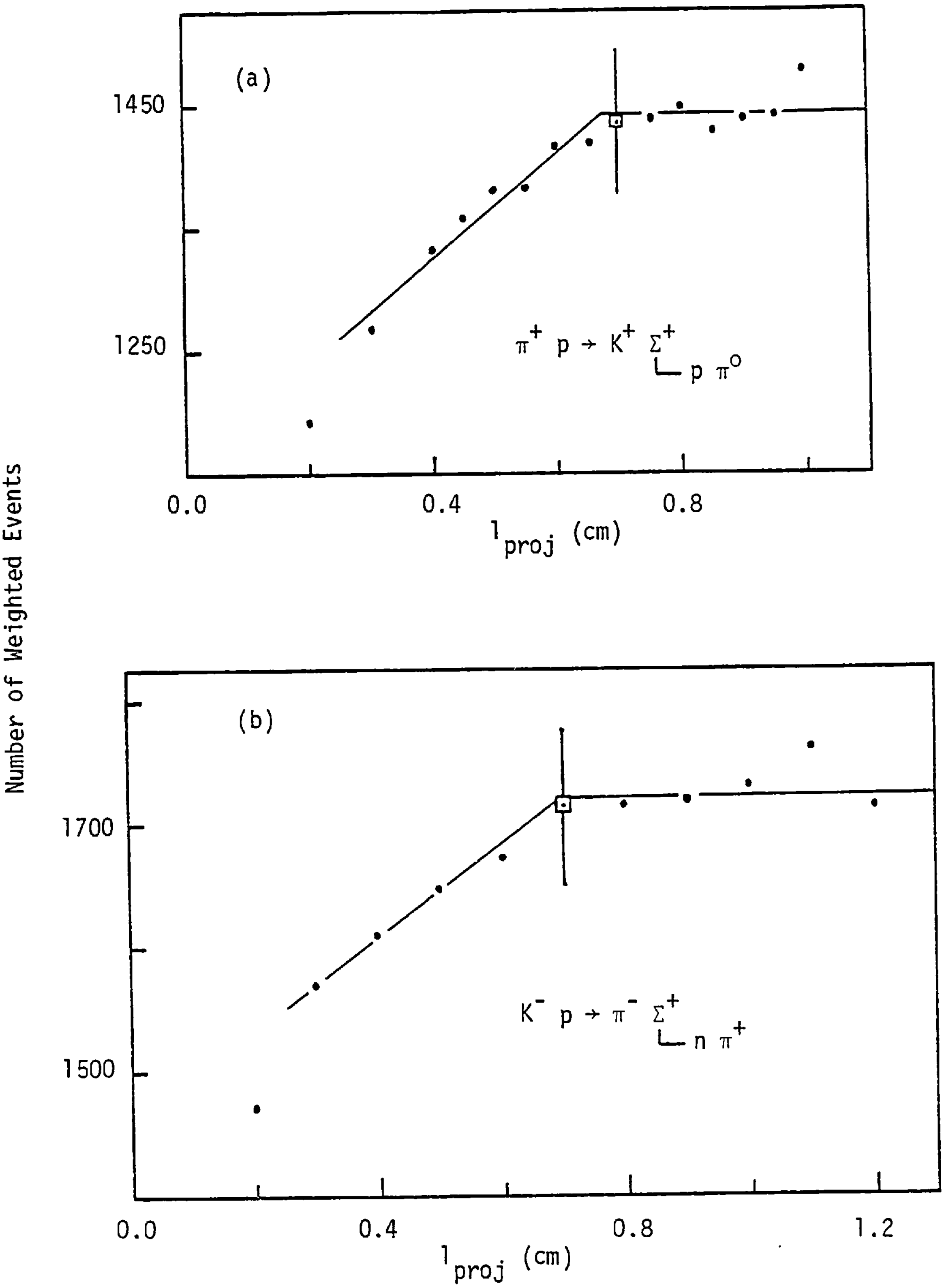

Fig 4.1 The Length Weighting

The weighted number of events as a function of the Σ^+ projected length.

Solid line is to guide the eye.

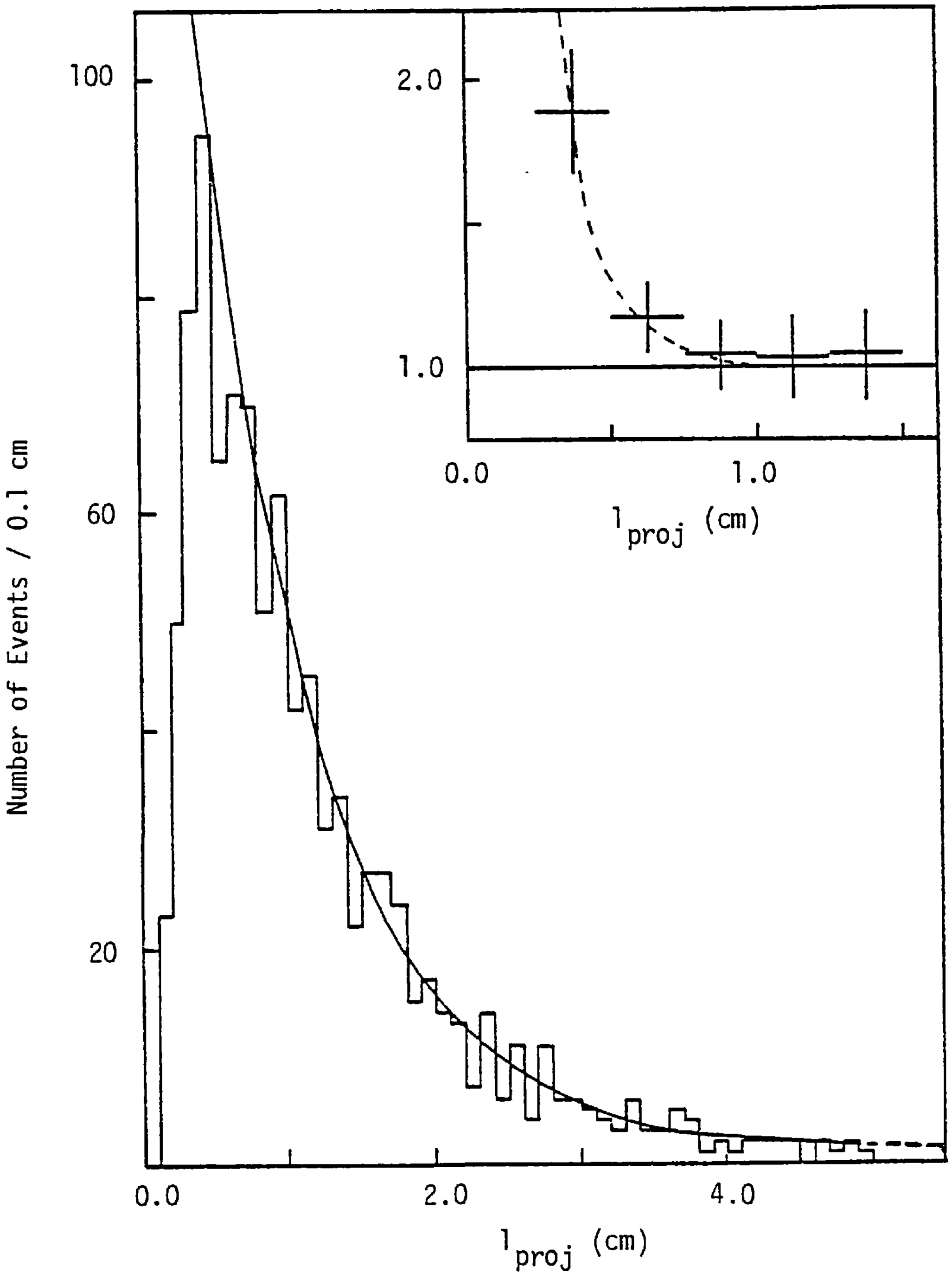

Fig 4.2 Σ^+ Projected Length Distribution

Channel: $\pi^+ p \rightarrow K^+ \Sigma^+$ ($\Sigma^+ \rightarrow n \pi^+$)

The curve is described in section 4.2.1.b.

The inset is the weight given by (integrated curve/data).

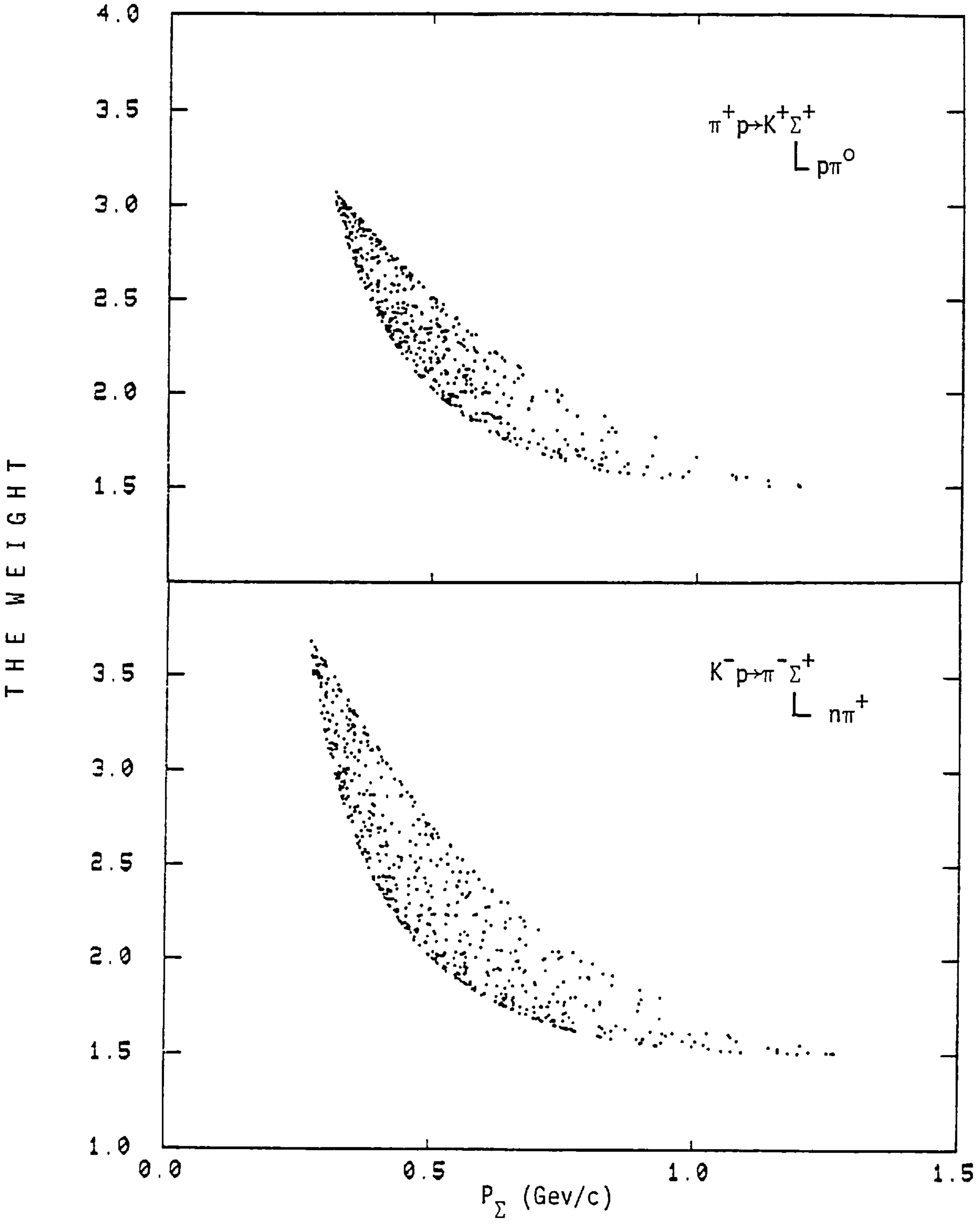

Fig. 4.3 The Length Weight distribution

4.3 Scanning Losses - Small Angle [17]

The isotropy of the cosine of the decay angle in the Σ^+ rest frame is used to calculate the small angle weight. It is given by (see Appendix 1.2)

$$Ws = \frac{\pi}{\Psi} \cdot \frac{2}{\cos\Theta^*_{max} - \cos\Theta^*_{min}}$$

where Θ^*_{min} and Θ^*_{max} are the minimum and maximum decay angles corresponding to a given cut-off value of the laboratory projected decay angle Θ_c. The π/Ψ factor accounts for the loss of events in which the Σ decay plane is nearly perpendicular to the x - y plane in the BC frame. Here again the assumption is that events having a laboratory projected angle greater than Θ_c will have detection probability of one. This loss, expected to be for $\Psi = 0^0$ and 180^0 is seen in Fig. 4.4a. Fig. 4.4b shows the raw $\cos\theta^*$ distribution . The losses around $\cos\theta^* = \pm 1$ can be seen especially in the protonic decay mode.

These losses are not so pronounced in the neutron decay mode because:

a) the C.M. angle, Θ^*, corresponded to a much larger angle (Fig.4.5) in laboratory for the $\Sigma^+ \rightarrow n\,\pi^+$ mode than for the $\Sigma^+ \rightarrow p\,\pi^0$ mode

b) even some small angle $\Sigma^+ \rightarrow n\,\pi^+$ decays could be seen due to the ionisation change at the decay vertex since the π^+ was usually minimally ionising while the Σ^+ was usually highly ionising.

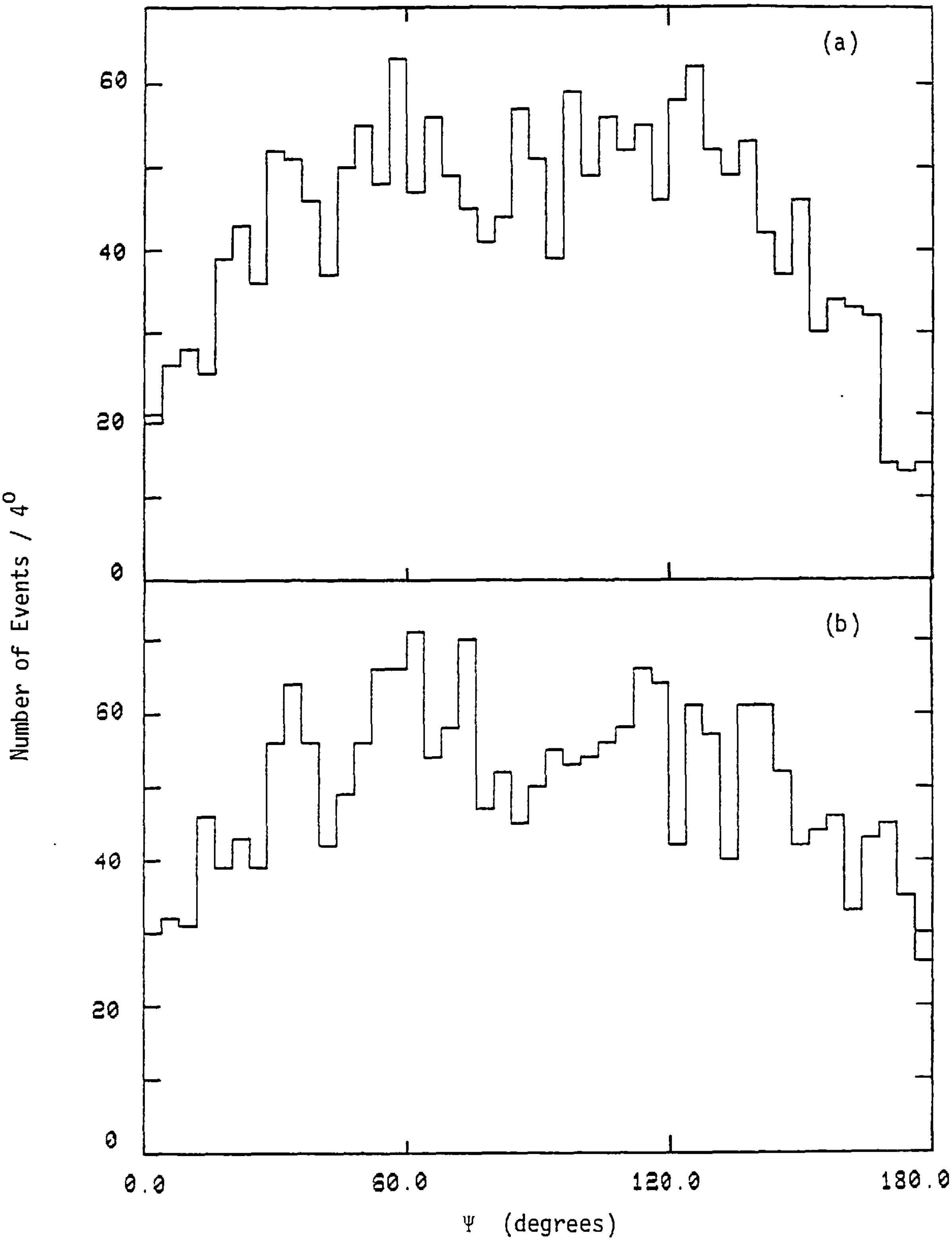

Fig 4.4a The Ψ distribution (see App. 1)

(a) $\Sigma^+ \rightarrow p\pi^0$ $(\pi^+ + K^-)$

(b) $\Sigma^+ \rightarrow n\pi^+$ $(\pi^+ + K^-)$

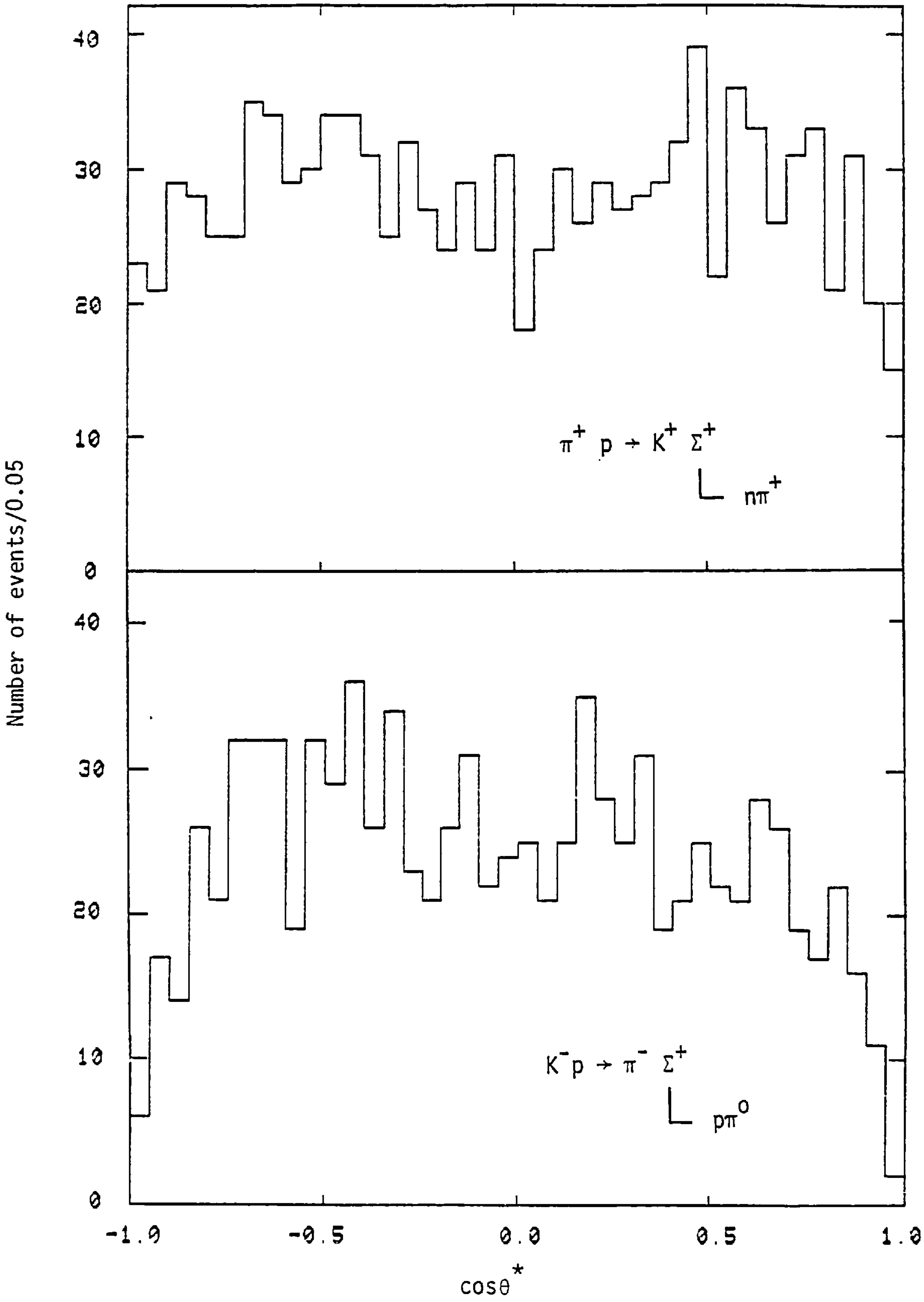

Fig. 4.4b $\cos\theta^*$ Distribution in the Σ^+ rest frame

Fig 4.5 shows the maximum laboratory decay angle for the decay modes of the Σ^+. It can be seen that the cut-off angle cannot be large, especially for the protonic decay mode. This limits the validity of these corrections for the protonic decay mode to low Σ^+ momenta.

Hence the protonic decay mode data with $|t| < 0.6$ $(\text{Gev}/c)^2$ was subjected to small angle corrections. The maximum decay angle for $\Sigma^+ \to p\,\pi^0$ mode at $t = -0.6$ $\text{Gev}/_c$ $(P_{\Sigma^+} = 0.98$ $\text{Gev}/c)$ is 14.2^0. The determination of the cut-off angle was carried out using the method described in 4.2.1(a). A plateau starting at $\Theta\text{cut} = 8^0$ can clearly be seen in Fig 4.6a. Eight degrees is sufficiently below the maximum allowed angle for the Σ^+ at the t cutoff of -0.6 $(\text{Gev}/_c)^2$ to make the weighting reliable. For the last t bin i.e. $0.6 < |t| < 1.0$ $(\text{Gev}/_c)^2$, only the $\Sigma^+ \to n\,\pi^+$ data was used and scaled appropriately.

Events in which the Σ^+ decays into a slow charged product (such that the length of the decay product is small) tend to get lost or mis-assigned. To account for the loss of these events, a cut on the laboratory momentum for the pion or proton decay product of 55 or 180 $\text{Mev}/_c$ respectively was applied (c.f. App. 1).

Fig 4.7 shows the small angle weight distributions w. r. t. the Σ^+ momentum.

Fig 4.8 compares the $\Sigma^+ \to p\,\pi^0 / \Sigma^+ \to n\,\pi^+$ ratio for the raw and weighted events after applying both the length and small angle corrections. Table 4.1 shows that the ratio after weighting compares

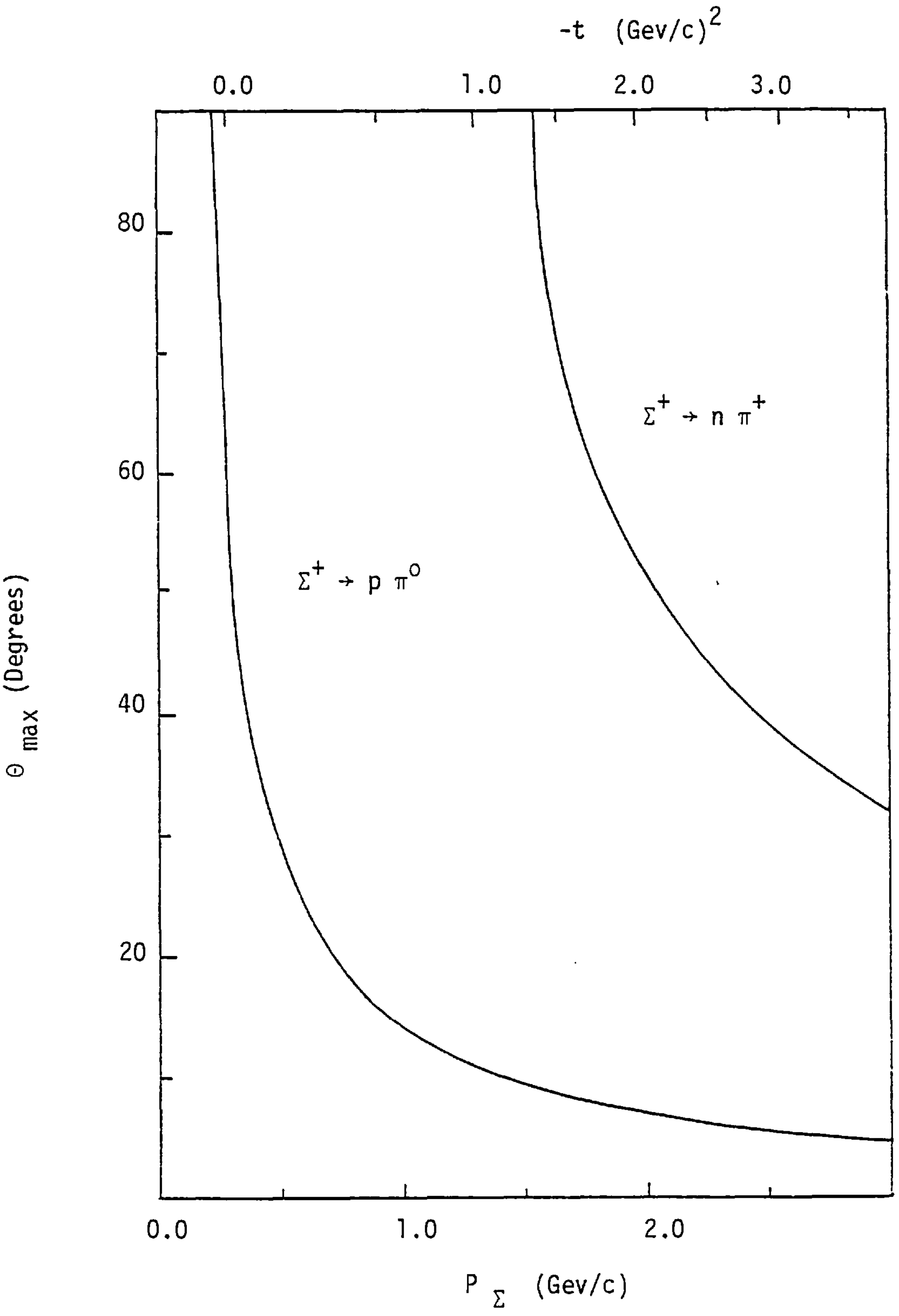

Fig. 4.5 Maximum Laboratory Decay Angle for Σ^+

The top scale is for $\pi^+ p \rightarrow K^+ \Sigma^+$ with beam momentum of 7.0 Gev/c.

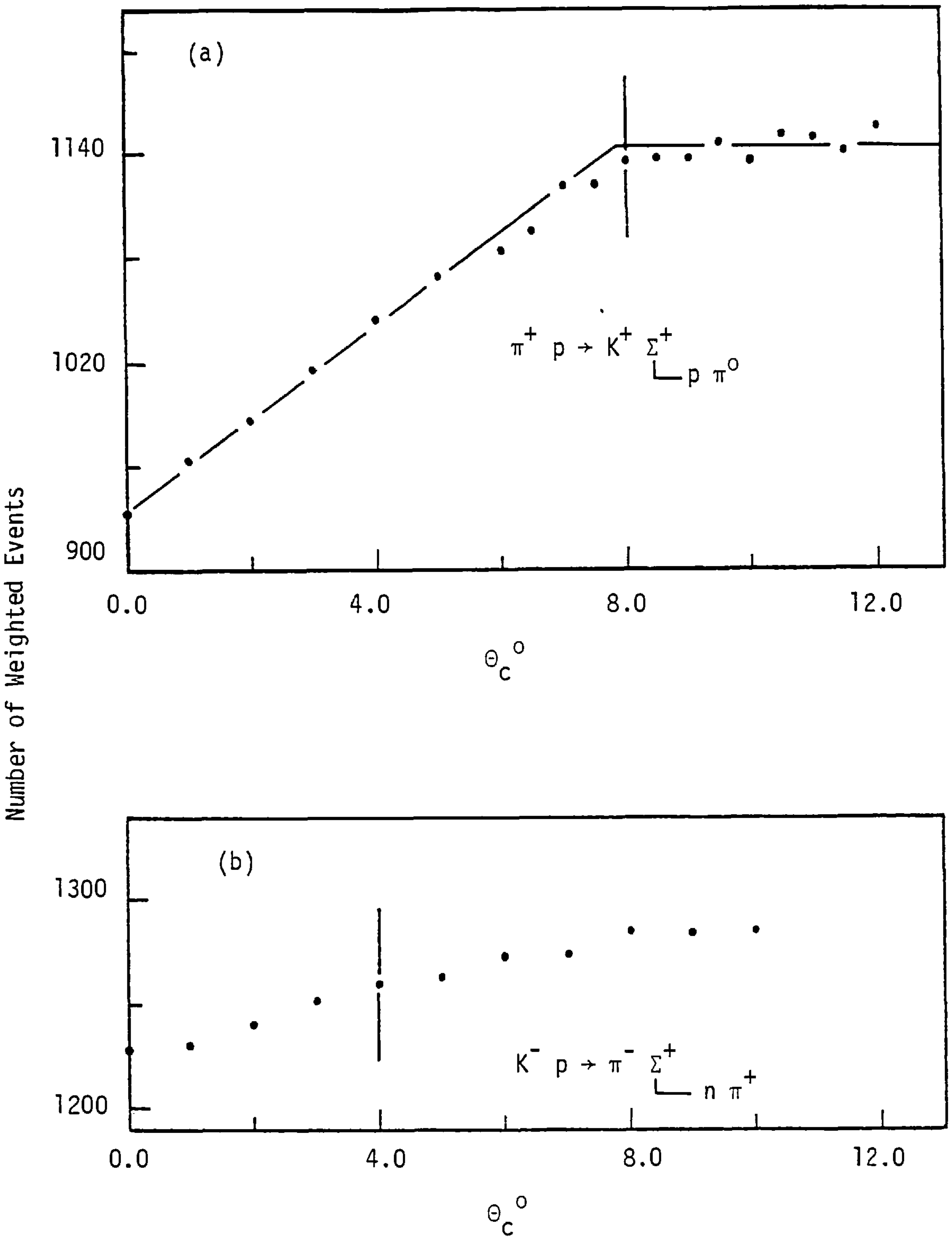

Fig. 4.6 The Small Angle Weighting

The weighted number of Σ^+ events as a function of the laboratory cutoff angle Θ_c

The solid line is to guide the eye.

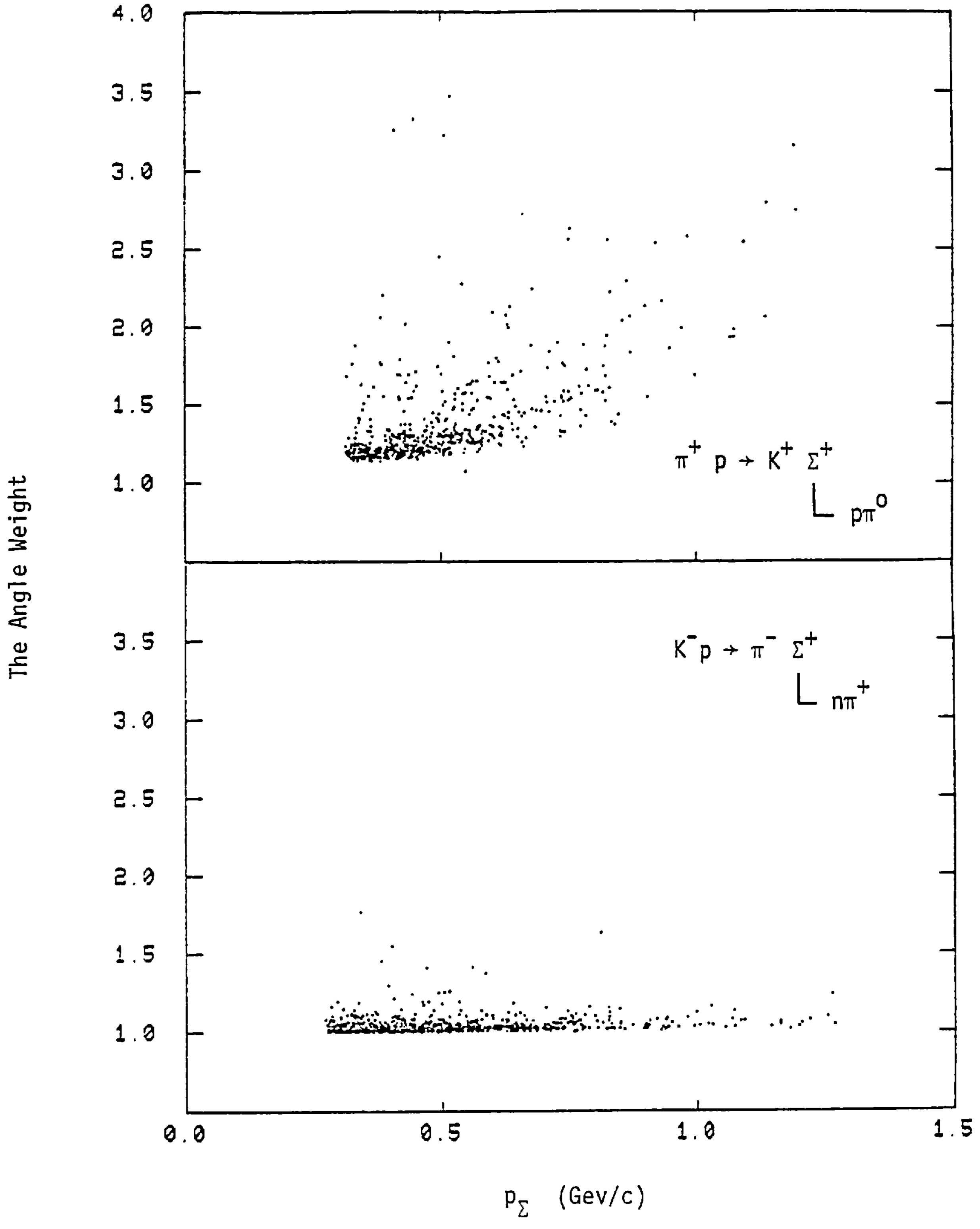

Fig. 4.7 The Angle Weight Distribution

favourably with the P. D. G value of 1.066 for Σ^+ branching ratio into the p π^0 as compared with the n π^+ decay mode.

Table 4.2 gives the cuts that were made in length and small angle weighting.

CHANNEL	$\pi^+ p \rightarrow K^+ \Sigma^+$		$K^- p \rightarrow \pi^- \Sigma^+$	
Σ^+ DECAY MODE	$n\pi^+$	$p\pi^0$	$n\pi^+$	$p\pi^0$
Projected Min	0.6	0.7	0.7	0.5
Length (cm) Max	6.0	6.0	6.0	6.0
Projected Angle	4^o	8^o	4^o	8^o
Charged Decay track momentum (Mev)	55	180	55	180
$p\pi^o/n\pi^+$ raw	0.89 ±	0.04	0.90 ±	0.04
ratio wtd	1.08	0.06	1.00	0.06

Table 4.2 Various cutoffs used in length and small angle weighting.

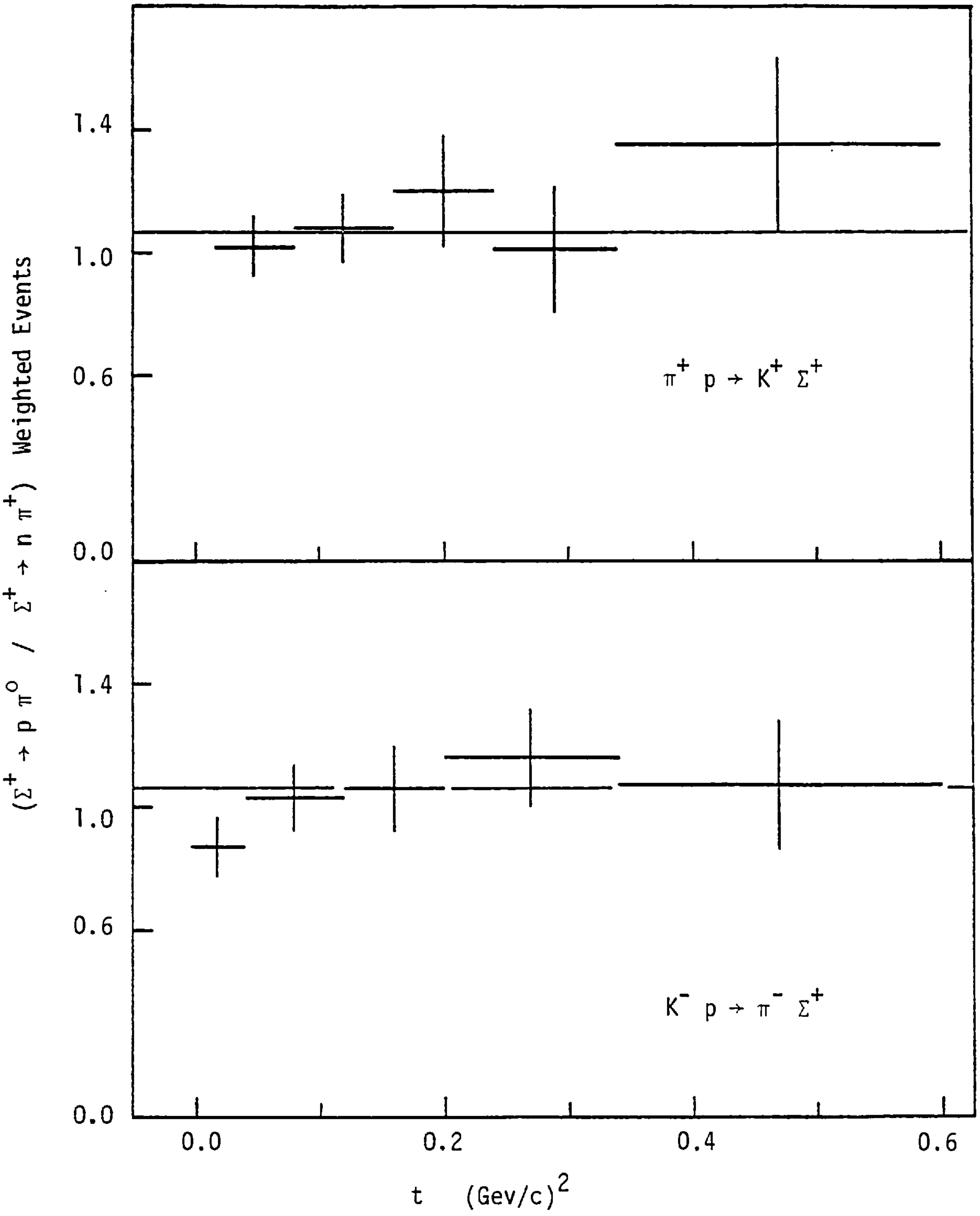

Fig. 4.8 The ratio $\Sigma^+ \to p\,\pi^0$ / $\Sigma^+ \to n\,\pi^+$ for weighted events

The solid line at 1.066 corresponds to P.D.G. value for this ratio.

4.4 Geometric Acceptance of the SLAC Hybrid System

To trigger the flash lamps and take a picture, the trigger particle had to get through the downstream detection system. The geometric acceptance is given by the probability, Pg, that the triggering particle in a given kinematical configuration will swim through the downstream system without obstruction. Fig 4.9 illustrates the BC exit aperture up to PWC Y.

The geometric weight was estimated individually for each event that reached the DST. This was achieved by swimming tracks with parameters p, λ and ϕ identical to those of the triggering track, originating from various points within the fiducial volume. The angle ϕ was computed for each x value, since ϕ changed with x due to the magnetic field. The x, y, z co-ordinates were generated such that x was random within the fiducial volume, y and z were Gaussians as given by the beam profile. The outgoing track was randomly rotated about the beam direction keeping the scattering angle constant for the given event. Pg was then simply given by ratio of the events in which the fast track was swum successfully through the downstream system and the number generated.

Trigger tracks were swum up to the downstream hodoscope in the π^+ exposure and the middle of CANUTE for the K^- exposure.

A cut on $|t| < 1.0\ (\mathrm{Gev}/_c)^2$ was imposed on the data to keep the geometric acceptance weights low. Fig 4.10 illustrates the distribution of weights w. r. t. the momentum transfer.

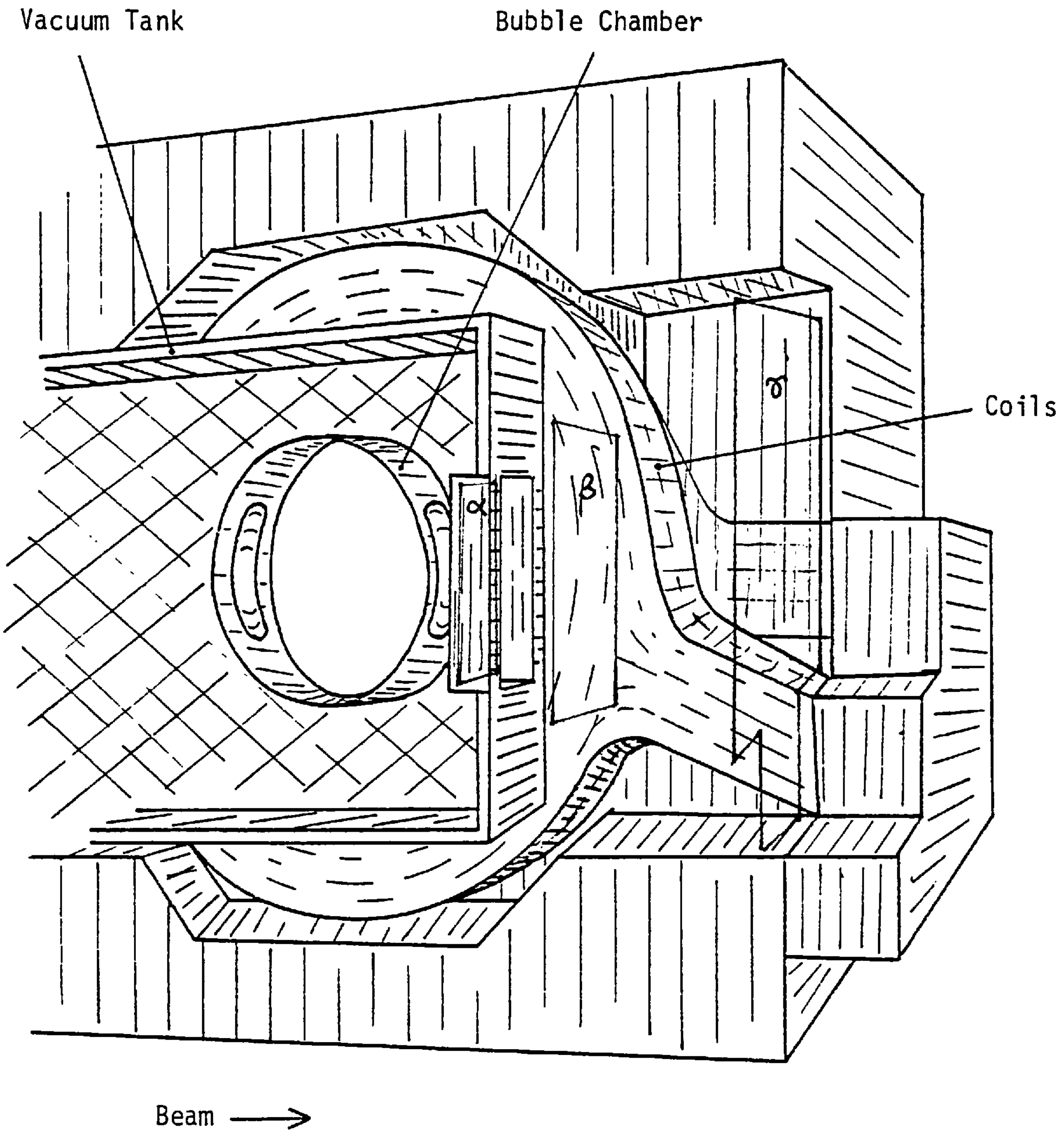

Fig. 4.9 The Bubble Chamber Exit Aperture

The figure shows the relationship of PWC's α, β and γ w.r.t. the exit aperture. The face shown is the further one w.r.t. film plane.

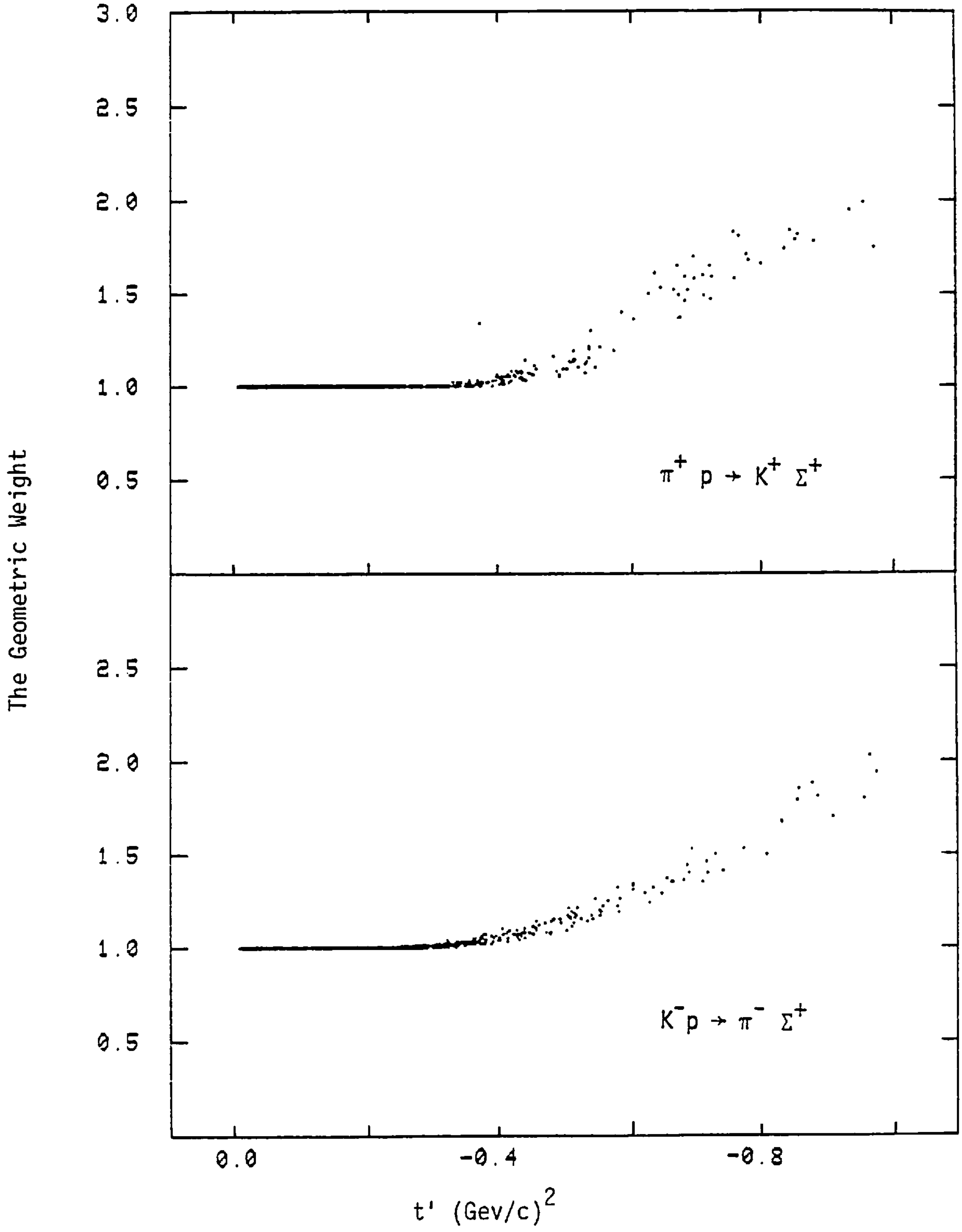

Fig 4.10 The Geometric Weight Distribution

4.5 The Software Trigger Alogrithm Acceptance

As noted in 2.3.2, the part of the software algorithm which rejects non-interacting beam tracks behaves like a small beam veto which moves for each beam track. This will reject very low |t| events. The effect of the veto was studied by generating beam and triggering track pairs using events on the DST in the manner similar to the one described in 4.4. The veto was parameterised in terms of the difference in wire numbers (2 wire numbers =1 wire separation) between the trigger track and the would have been beam track at PWC's α and γ.

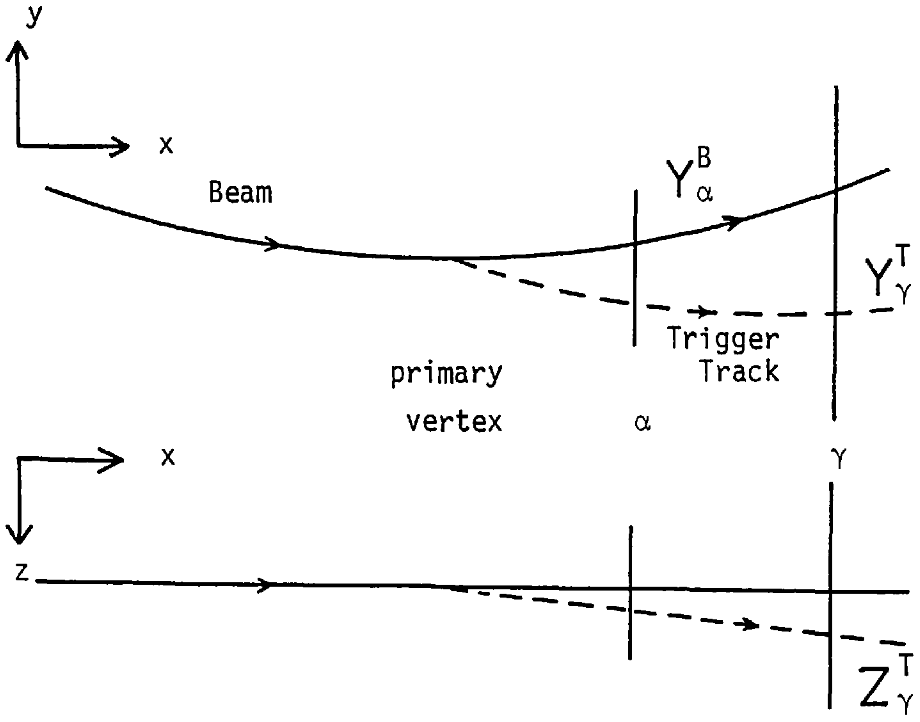

Fig. 4.11 Beam and Trigger track to illustrate the method used to determine algorithm acceptance.

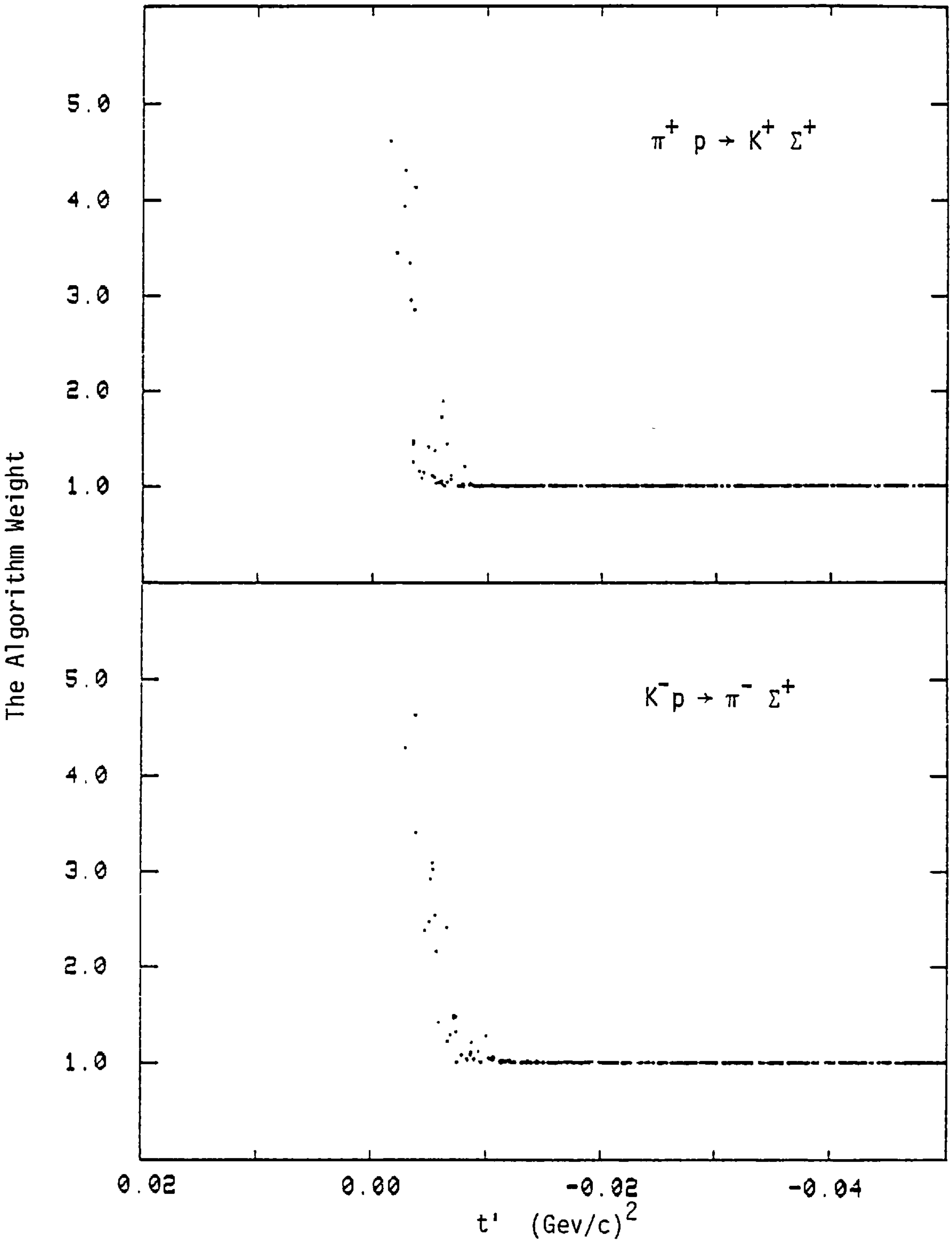

Fig. 4.12 The Algorithm Weight Distribution

Both beam and trigger tracks were swum downstream and the event was taken to have vetoed if all the following tests were satisfied (see Fig. 4.11):

		π^+	K^-
		WIRE	NOS
$\lvert Y_\alpha^T - Y_\alpha^B \rvert$	$\leqslant$	10	14
$\lvert Z_\gamma^T - Z_\gamma^B \rvert$	$\leqslant$	17	20
$\lvert Y_\gamma^T - Y_\gamma^B \rvert$	$\leqslant$	14	20
$\Big\lvert \lvert Y_\gamma^T - Y_\alpha^T \rvert - \lvert Y_\gamma^T - Y_\alpha^B \rvert \Big\rvert$	$\leqslant$	8	12

where Y_a^b (co-ordinate)
T = Trigger, B = Beam Track
PWC Station

A cut on t such that $t_c = t_{min} - 0.005$ was made to keep the alogrithm acceptance weight small. The distribution of weights w.r.t. t is illustrated by Fig. 4.12.

4.6 Summary

The overall distribution of weights (length . small angle . geometric . algorithm) for the two decay modes of Σ^+ are shown in Fig. 4.13.

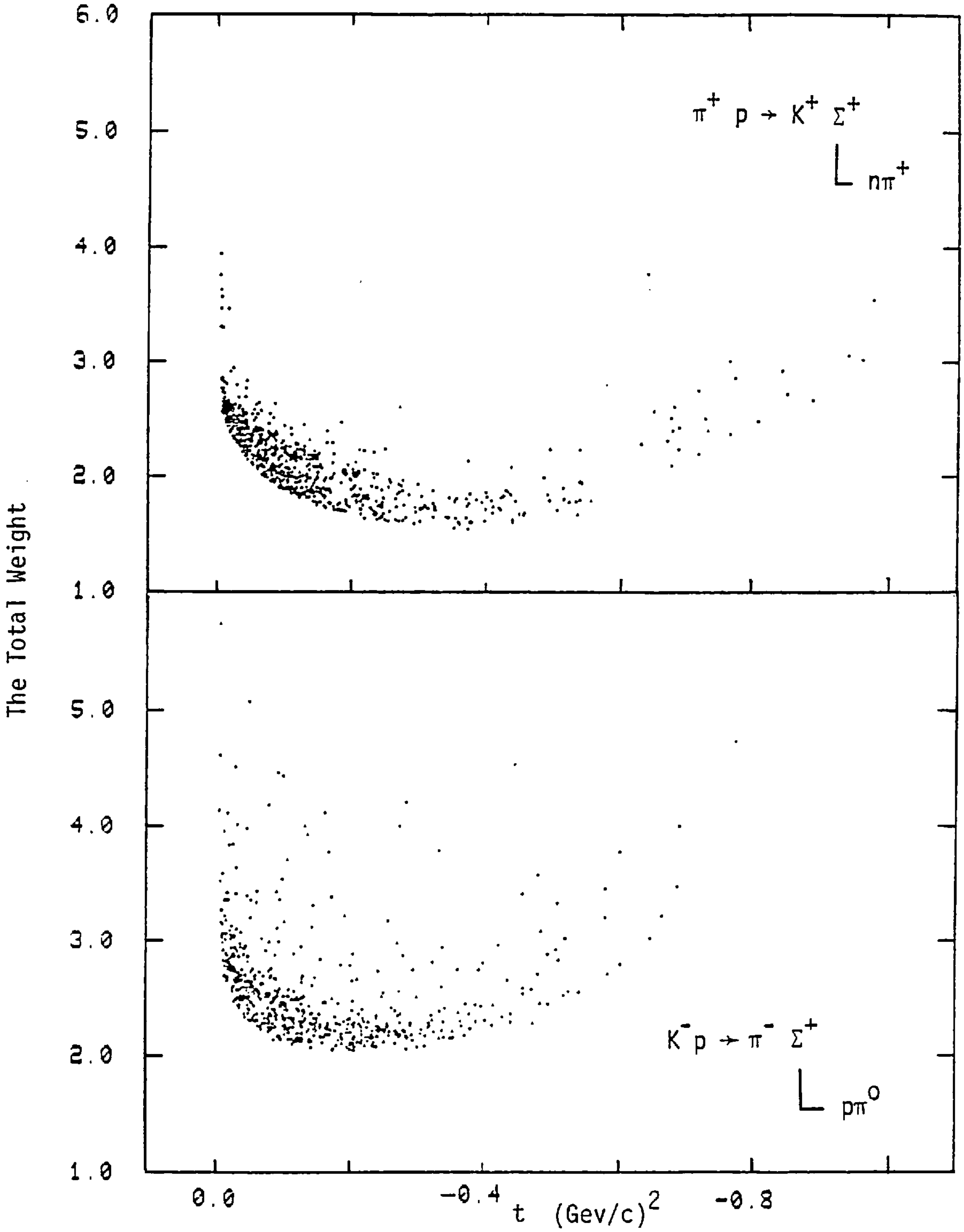

Fig. 4.13 The Total Weight Distribution

Total Length . Small Angle . Geometric . Algorithm

CHAPTER 5

Normalization And Further Corrections

5.1 Introduction

Unlike a conventional bubble chamber experiment, the pictures were taken in a biased way. The use of external electronic counter information to influence picture-taking introduced the necessity for corrections which are normally associated with purely counters experiments. In this chapter, these and some other corrections are described. The numbers obtained for the described corrections are summarized in Table 5. 3 at the end of this chapter.

5.2 The Scanning Correction

This was obtained by the 'double scan' method which is outlined below.

Assuming that N_T are the true (unknown) number of events and N_1, N_2 are the number of events found by the first and second scans respectively, the individual scanning efficiencies are then given by

$$\lambda_1 = \frac{N_1}{N_T} \qquad \lambda_2 = \frac{N_2}{N_T} \qquad \text{(i)}$$

If we also assume that $\lambda_1 . \lambda_2$ is the probability that an event of interest is selected on both scans, then the number of events common to both scans N_{12} is

$$N_{12} = \lambda_1 . \lambda_2 . N_T$$

$$\lambda_1 = \frac{N_{12}}{N_2} \text{ and } \lambda_2 = \frac{N_{12}}{N_1} \qquad \text{(ii)}$$

The probability that both scans will miss an event is then given by

$$(1 - \lambda_1).(1 - \lambda_2) \qquad \text{(iii)}$$

The scanning correction then ((ii) and (iii)) is

$$W_1 = \frac{1}{1 - (1-\lambda_1).(1-\lambda_2)} = \frac{N_1 . N_2}{N_{12}(N_1 + N_2 + N_{12})}$$

This method is only valid if the event configuration does not lead to the event being systematically missed by both scans. An example of such a systematic loss is in the short decay length kinked topologies. Ideally the scanning efficiency should thus be calculated with kinked events which fall in the region of no systematic losses. A small sample of data was double scanned. Due to the consequent lack of statistics, the scanning efficiency for two pronged events was used.

5.3 Analysis System Throughput Correction

This correction is for events lost in the event analysis chain shown in Fig. 3.1. The major causes of this loss are:

a) unmeasurable events: these are events having configurations on film which are unfavourable to measurement.

b) bad HPD measurements which may lead to track or point reconstruction failure in HYDRA geometry and this failure in GRIND kinematics.

The losses are expected to be random for any particular topology.

The correction factor was essentially given by

$$W_2 = \frac{N + R}{N}$$

where N are the number of events of the type

$\pi^+ p \rightarrow K^+ \Sigma^+ \, / \, K^- p \rightarrow \pi^- \Sigma^+$ on the DST

and R are the number of events of the above type which are unmeasurable or to be remeasured.

5.4 Fast Trigger Losses

A period of about 180 nsec after the first trigger, was required to temporarily store the PWC hits information in electronics. Another fast trigger occuring within this period was rejected. Another cause for the loss of fast triggers was due to the fact that no more than two fast triggers were permitted in any one beam pulse. This meant that the imposed deadtime after the second fast trigger was extended to the remaining duration of the pulse. A spill with two fast triggers is illustrated in Fig. 5.1.

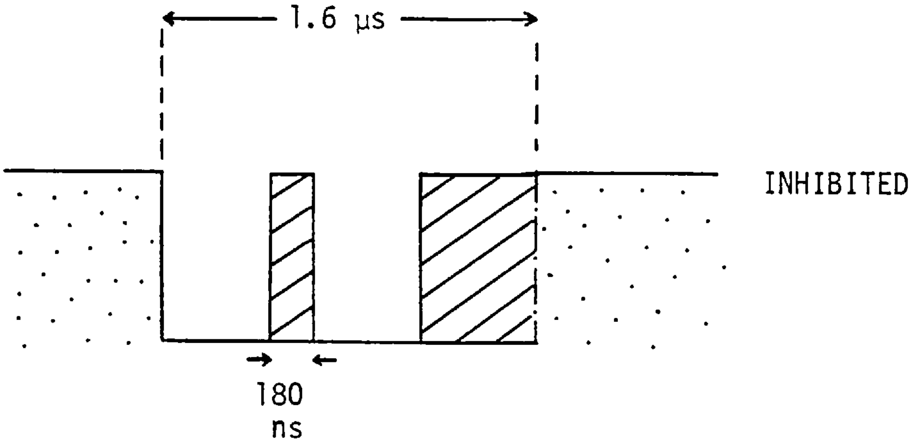

Fig. 5.1 A spill with two fast triggers.

Essentially, the result of the fast trigger losses is a reduction in the effective flux.

The losses were estimated by using first fast triggers (T1's) only.

The loss of statistics is not significant because only about 10% of the events came from second fast triggers (T2's).

Suppose that,

a) the fast-trigger probability per incident beam π (K) is p,

b) the mean number of beam π (K)'s per spill is μ,

c) in M spills there are N_1 events occuring on N_{T1} T1's,

then the observed number of events, correcting for the loss of events on fast triggers T_2, T_3,......etc, corresponding to μM beam π (K)'s has to be multiplied by the factor

$$W_{12} = \frac{\mu p}{(1-e^{-\mu p})}$$

where

$$p = \frac{\text{No. of fast triggers}}{\text{No. of beam } \pi\text{'s(k's)}}$$

$$\mu = \frac{\text{No. of beam } \pi\text{'s(K's)}}{\text{No. of pulses}}$$

5.5 PWC Inefficiencies

As outlined in Chapter 2, a successful software trigger required:

a) both y and z planes to be hit, resulting in a matching hit in either BPWC1 or BPWC2.

b) all three planes (y, z and u) to be hit resulting in a matching hit in two out of the three downstream PWC's plus a confirmatory hit in any one of the three planes of the third PWC.

This meant that inefficiencies in the PWC's resulted in failure to obtain triggers.

The method used to determine PWC efficiencies was as follows:

an offline program, which used the PWC hits information on the counter data tape, reconstructed the beam and the outgoing track. Acceptable track reconstructions were required to have a hit on at least 11 out of the possible 13 planes. The missing hits, if any, were thus determined and the plane efficiencies were given by

$$\frac{\text{hits}}{\text{hits} + \text{misses}}$$

Table 5.1 shows the plane and PWC efficiencies for the π^+ and K^- exposures.

If P_i, where $i \equiv$ PWC's 1,2, α, β, γ, were the PWC efficiencies, then the overall efficiency for the upstream PWC's was given by (with reference to Table 5.1),

$$P_1.P_2 \quad + \quad P_1.(1-P_2) + P_2.(1-P_1)$$

as only one of the two upstream PWC's was required to have the full complement of hits (cf 2.3.2).

As outlined in 2.3.2, a successful trigger required a full complement of matching hits in two of the downstream PWC's plus a confirmatory hit in any one plane of the third PWC. Thus the overall efficiency of the downstram PWC system was given by

$$P_\alpha P_\beta P_\gamma + P_\alpha P_\beta P'_\gamma + P_\alpha P'_\beta P_\gamma + P_\beta P_\gamma P'_\alpha$$

where P'_i ($i = \alpha,\beta,\gamma,$)represents the efficiency that the third plane has at least one but no more than two confirmatory hits. Therefore

$$P'_i = \sum_{\substack{\text{cyclic} \\ \text{in } y,\ z,\ u}} P_y P_z (1-P_u) + P_y\ (1-P_z)\ (1-P_u)$$

where y, z and u are the wire planes making up a downstream PWC.

5.6 Triggering Track Interaction/Decay

The events in which the fast forward triggering particle interacts or decays may not trigger the system and hence be lost. The loss due to interactions can be estimated from the knowledge of the amount of material through which the particle had to pass. Table 5.2 shows the material in the beam downstream of S1. The distance used for these corrections was taken to be from the primary vertex to the middle of the Cerenkov CANUTE. To avoid double counting only events which obtained a hybrid fit downstream were used for this correction. As can be seen from Table 5.2, the main sources of

RUN	π^+				K^-			
WIRE PLANE PWC	y	u	z	OVERALL	y	u	z	OVERALL
BPWC 1	90		90	81	89		88	78
BPWC 2	95		97	92	91		90	82
α	97	93	95	86	85	94	93	83
β	97	95	95	87	96	94	95	86
γ	94	92	95	83	94	96	95	86

Table 5.1 PWC efficiencies for the π^+ and K^- runs at 7 Gev/c.

Element	Position	Material	t	$100L/L_{coll}$	% not interacting
S_1	- 899	Scintillator	1/4"	1.15	98.8
Air	--	Air	28.5cm	.06	
BPWC1	- 865	$.15gm/cm^2$	5 cm	.3	98.5
Air	--	Air	335.5cm	.67	97.8
C window	-527.5	Al	.007"	.07	
Freon	--	1 atm Freon	134 cm	.97	96.8
Mirror	-393.5	Lucite	.9 cm	1.80	95
Freon	--	1 atm Freon	18.5 cm	.13	
C window	-375	Al	.007"	.07	
Air	--	Air	9.5	.02	
BH	-365.5	Scintillator	1/4"	1.15	93.8
Air	--	Air	38 cm	.08	
BPWC2	-325	$.15gm/cm^2$	5 cm	.3	
Air	--	Air	6.5 cm	.013	
Vac Window	-316.	Al	.06"	.6	
BC window	-57.5	St Steel	.058"	1.44	92
Hydrogen	0	H_2	115 cm	9.9	83.4
BC window	+57.5	St Steel	.07"	1.74	
Vac window	75	St Steel	.063"	1.57	80.7
Air	--	Air	10 cm	.02	
α	77.0	$.465gm/cm^2$	15	.8	
Air	--	Air	26	.052	
β	118.6	$.465gm/cm^2$	15	.8	
Air	--	Air	67	.134	
γ	200.	$.835gm/cm^2$	15	1.4	
Air	--	Air	68	.136	78
CANUTE window	275.5	Al	1/4"	2.5	76
Freon	--	2.5 atm	290 cm	3.15	73.7
Mirror	565.5	Lucite	1/4"	1.3	
Freon	--	2.5 atm	10 cm	.11	
Window	575.5	Al	1/4"	2.5	71

Table 5.2 Material in SLAC Beamline 14

secondary interactions were:

a) the liquid hydrogen downstream of the primary interaction

b) the stainless steel BC and vacuum tank exit windows

c) the material in the downstream PWC's

d) the entrance window and the freon in CANUTE.

Elastic interactions downstream of γ were not taken to veto the trigger. The loss due to decay was more important in the π^+ exposure where the fast forward K^+ could decay into a lighter particle which would veto the fast trigger by giving light in CANUTE.

To account for the fact that triggering particle cannot both decay and interact, the number of triggers had to be multiplied by a factor

$$W_5 = e^{P} \cdot e^{x/\lambda} \cdot e^{-Px/\lambda}$$

where P is the probability of interaction,

$$x = (x_{\frac{1}{2}\mathrm{CANUTE}} - x_{\mathrm{pri\ vtx}})$$

$$\lambda = \frac{p' c\ \tau}{m}$$ and p',τ,m, are momentum, mean lifetime and mass of the decaying particle.

The average value of W was found to be 1.20 in the π^+ exposure and 1.14 in the K^- exposure.

5.7 Beam Track Interaction/Decay

In Section 5.4 the total count of $S1 \cdot CB \cdot BH$ or $S1 \cdot \overline{CB} \cdot BH$ was used as the number of beam π's or K's respectively. Some of beam particles may interact or decay between 40cm upstream of CB and the primary interaction vertex resulting in the loss of flux. The main sources of interactions are:

a) the beam hodoscope

b) the vacuum-tank and BC entrance windows

c) the liquid hydrogen upstream of the primary interaction vertex.

As in 5.6, the total flux had to be multiplied by a factor

$$W_{10} = e^{p} \; e^{x/\lambda} \; e^{-px/\lambda}$$

with the same definitions as above.

The average value of W was found to be 1.08 in the π^+ exposure and 1.18 in the K^- exposure.

5.8 Muon Counter Punch Through

Some triggering π^-'s in the K^- exposure may have punched through the muon counter and so veto the trigger. To determine the punch through some incident π^- film was taken. A fast outgoing non beam particle was required for the picture to be taken. For events in which the fast forward track from an interaction hybridised, the muon counter was examined. Since the probability that the outgoing particle was a muon was extremely low, the punch through was simply given by the percentage of particles that gave a signal in the μ - veto hodoscope consistent for a muon.

5.9 Beam Contamination

In the π^+ exposure, an acceptable beam required light to be emitted in the beam Cerenkov. Particles of pion or lower mass would thus satisfy the upstream part of the fast trigger logic. A lead filter at the first focus removed the positrons leaving muons as the source of beam contamination in the π^+ exposure.

To estimate the beam contamination, the data tapes of a special π^+ exposure were used to examine non-interacting beam tracks. The percentage of beam tracks that passed through the muon counter was determined. The muon contamination of the beam in the π^+ exposure was then given by

Beam punch through in the special π^+ exposure	—	Punch through by the fast forward track from an interaction in the π^- exposure (cf 5.8).

$$\Rightarrow (10.3 \pm 0.8 - 5.7 \pm 1.0) = 4.6 \pm 1.3 \%$$

The $\bar{p}$ contamination in the K^- exposure was estimated to be about 2%.

5.10 Multiplicity Cuts in PWC's

Any fast trigger which occurred when there were more than 2 intime beam tracks in the upstream PWC's was rejected (cf. 2.3.2.). Also any spill which had S1.BH>12 was rejected since higher beam intensity leads to higher deadtime losses.

These cuts were made in the software algorithm. Since data from all hardware triggers was written on the data tapes, the effects of these cuts were easily determined.

5.11 Pile up In CANUTE

In the π^+ exposure, since no light was required in CANUTE, a fast trigger would have been rejected if a non-interacting beam were in time with the beam that initiated the trigger. Such a problem does not arise for the K^- exposure.

5.12 Overall Normalisation

For overall normalisation rolls which did not have suspect scaler data were used. A fiducial length of 65 cms was used.

The channel cross-section is given by:

$$\sigma = \frac{Ne\ t}{N_B\ L} \qquad \mu b$$

where N_e is the corrected number of events for the channel

N_B is the corrected number of beam tracks

t is the thickness of hydrogen (m^3)

L is the fiducial length (metres)

If the number of observed events was N_e^o, then the corrected number of events N_e was given by (Table 5.4).

$$N_e = W_G \cdot W_{BR} \cdot \left(\prod_{i = 1, 9} W_i \right) \cdot N_e^o$$

where W_G represents the Σ^+ length geometric algorithm correction for reactions $\pi^+ p \rightarrow K^+ \Sigma^+$ and $K^- p \rightarrow \pi^- \Sigma^+$ as described in Chapter 4, and $W_{BR} = 2.066$ is the reciprocal of the branching ratio of $\Sigma^+ \rightarrow n\pi^+$ decay mode since only these events were used for overall normalization.

If N_B^o were the total number of observed beam tracks, the corrected number was given by

$$N_B = W_{10} \cdot W_{11} \cdot W_{12} \cdot N_B^o$$

Table 5.3 gives the average numbers for various corrections described in this chapter. The overall normalization uncertainty was estimated to be less than 10%. In normalizing, the main differences between the π^+ and K^- runs were:

a) pileup in CANUTE

b) muon counter punch through

c) beam contamination

d) beam/trigger track interaction and decay.

The relative normalization uncertainty was estimated to be about 7%.

A large part of this chapter is not the author's work. It has been included for completeness.

	Correction		Weight	
			π^+	K^-
W_1	Scanning		1.06	1.07
W_2	Throughout		1.14	1.19
W_3	PWC Inefficiencies	Upstream	1.08	1.10
W_4		Downstream	1.06	1.06
W_5	Trigger Track intn. or decay		1.20	1.14
W_6	Muon Counter Punch Through		1.00	1.06
W_7	Multiplicity Cuts	$N_{Beam} > 2$	1.06	1.07
W_8	S1.BH>12	S1.BH>12	1.02	1.02
W_9	Pileup in CANUTE		1.04	1.00
W_{10}	Beam Track intn. or decay		1/1.08	1/1.18
W_{11}	Beam Contamination		0.85	0.98
W_{12}	Fast Trigger Losses		0.94	0.88
W_G	Σ^+ length. Geometric. algorithm		1.61	1.58

Table 5.3 Average Numbers for various corrections.

CHAPTER 6

The Results

6.1 Introduction

The results of the total and differential cross-sections and polarization measurements for channels

$$\pi^+ p \rightarrow K^+ \Sigma^+ \qquad (I)$$

$$K^- p \rightarrow \pi^- \Sigma^+ \qquad (II)$$

are presented in this chapter. The discussion and the implication of the results are in the next chapter.

6.2 The Total Cross-section Measurement

The total cross-sections were determined by using the expression obtained in section 5.12. Only $\Sigma^+ \rightarrow n \pi^+$ decay mode events were used. The integrated cross-sections for

$$tmin - 0.005 < t < -1.0 \ (Gev/c)^2$$

were obtained. The total cross-section was found to be 40.1 ± 4.5 for the channel $\pi^+ p \rightarrow K^+ \Sigma^+$ and 60.6 ± 6.8 for $K^- p \rightarrow \pi^- \Sigma^+$.

6.3 The Differential Cross-section Measurement

The differential cross-sections were determined by using data from both $\Sigma^+ \rightarrow n\pi^+$ and $\Sigma^+ \rightarrow p\pi^0$ decay modes. Each decay mode sample was normalized separately. The normalized differential cross-section was determined by the expression

$$\frac{d\sigma}{dt} = \frac{n'}{\Delta t}\,\frac{\sigma}{N} \qquad \mu b/(Gev/c)^2$$

where n' is the weighted number of events in a bin of width Δt $(Gev/c)^2$ and N is the total weighted number of events corresponding to a total cross-section of σ μb. The error on the differential cross-section is then given by

$$\Delta\,\frac{d\sigma}{dt} = \frac{1}{\sqrt{n'}}\,\frac{d\sigma}{dt}$$

where n' is the number of events actually used in the weighting. The data samples were then merged taking due account of the errors. For the last t bin, $0.6 < |t| < 1.0$, the $d\sigma/dt$ obtained from the $\Sigma^+ \rightarrow n\pi^+$ decay mode data was used, multiplied by 2.066 (cf 4.3). Figs 6.1 and 6.2 show the individually normalized differential cross-sections. Fig 6.3 shows the merged differential cross-sections. As can be seen, the data confirm earlier results in showing a simple exponential behaviour for $|t| < 0.4\ (Gev/c)^2$. There is no evidence of a turnover in the forward direction.

Fits to the differential cross-section of the form

$$\frac{d\sigma}{dt} = A\,e^{bt}$$

were made in the low $|t|$ region.

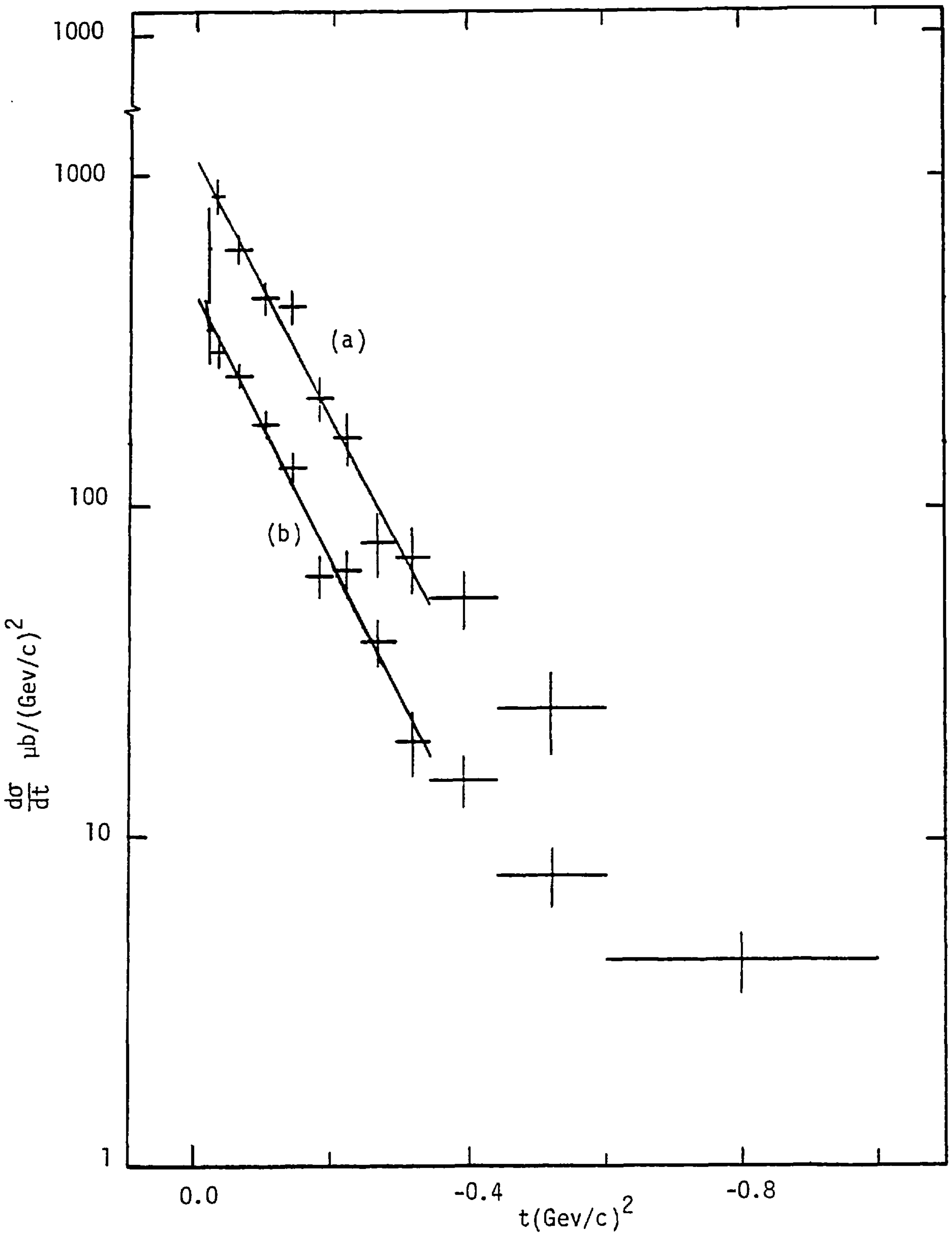

Fig. 6.1 The differential cross-sections for $\pi^+ p \to K^+ \Sigma^+$

The fit (solid lines) parameters are

a) $\Sigma^+ \to p\pi^0$ slope = 9.11 ± 0.59/ intercept = 389.7 ± 32.3

b) $\Sigma^+ \to n\pi^+$ slope = 9.35 ± 0.53/ intercept = 402.7 ± 30.9

Errors are statistical.

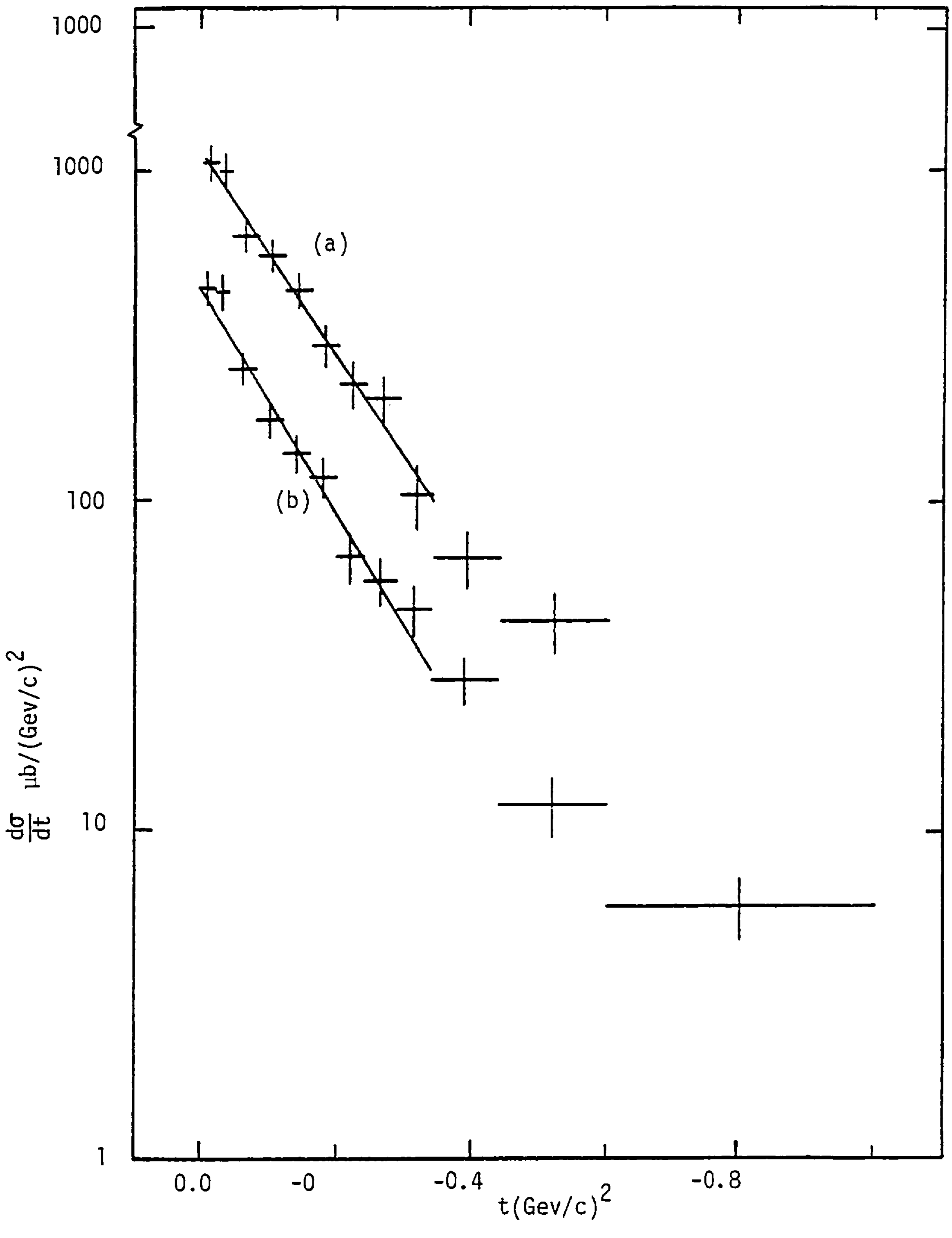

Fig. 6.2 The differential cross-sections for $K^- p \rightarrow \pi^- \Sigma^+$

The fit parameters are:

a) $\Sigma^+ \rightarrow p\pi^0$ slope = 7.01 ± 0.50/ intercept = 396.0 ± 27.8

b) $\Sigma^+ \rightarrow n\pi^+$ slope = 7.84 ± 0.55/ intercept = 429.8 ± 33.0

Errors are statistical.

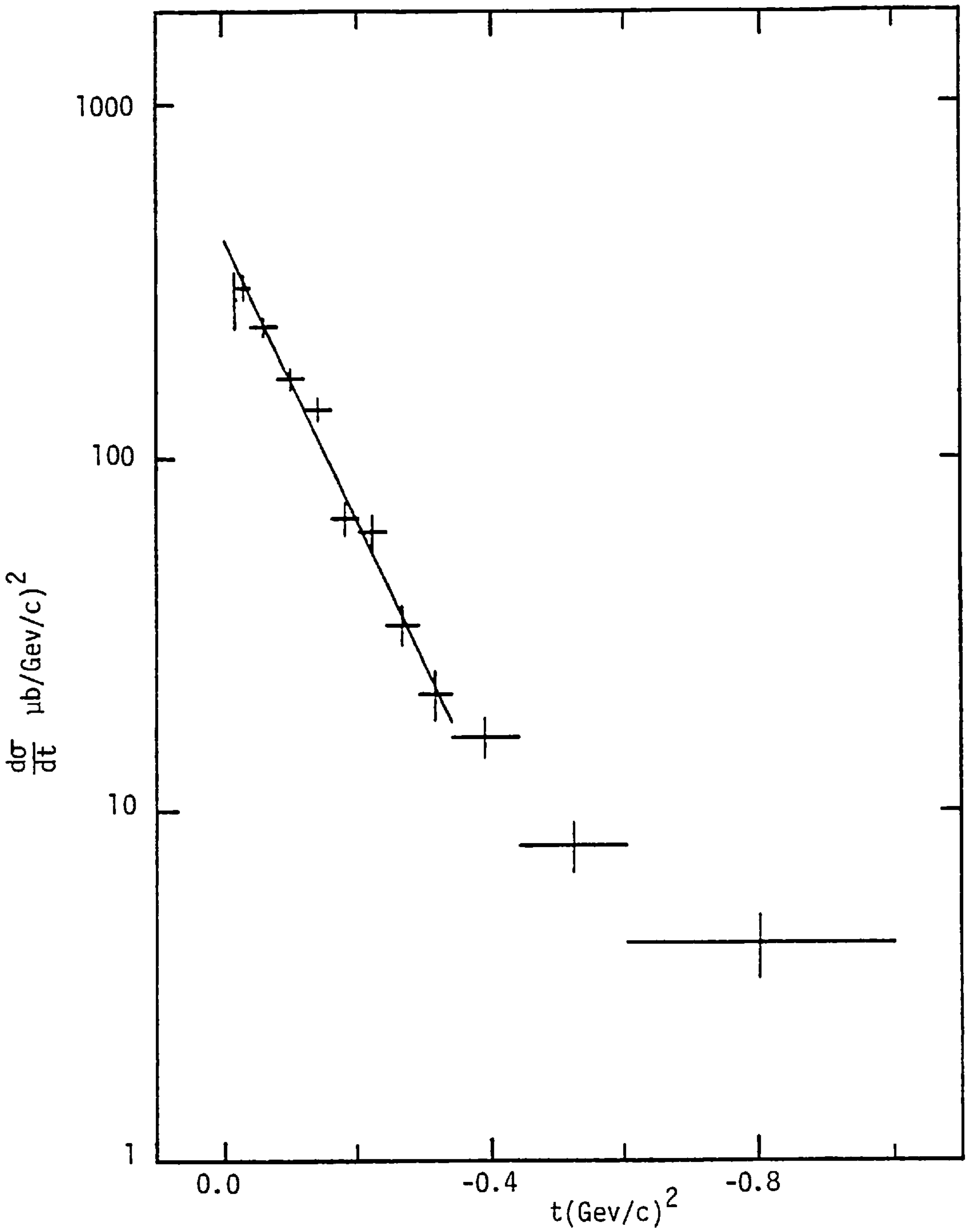

Fig. 6.3a The Merged differential cross-sections for $\pi^+ p \rightarrow K^+ \Sigma^+$
The fit parameters are
slope = 9.25 ± 0.38
intercept = 397.1 ± 21.4
Errors are statistical.

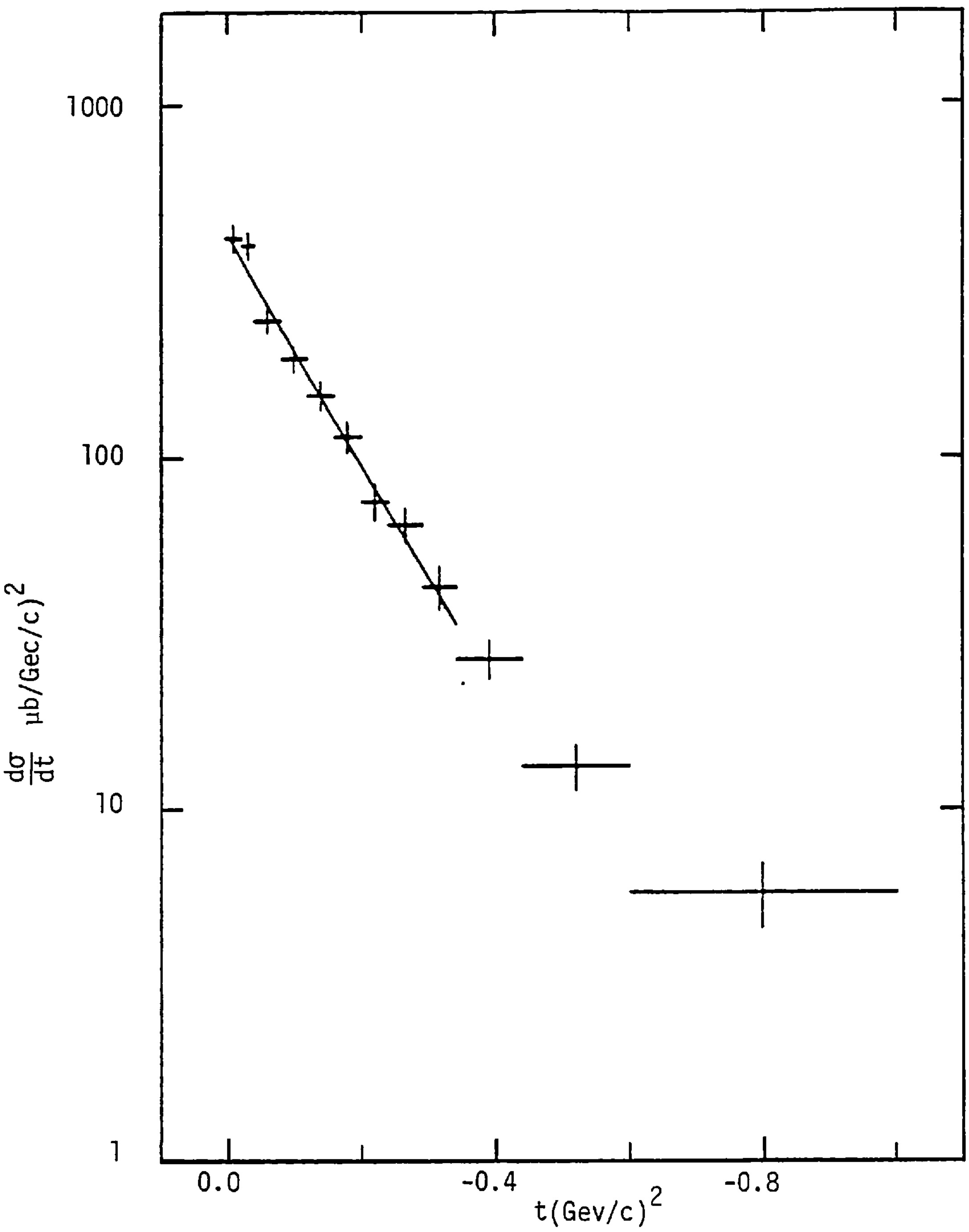

Fig. 6.3b The Merged Differential Cross-Section for $K^- p \rightarrow \pi^- \Sigma^+$

The fit parameters are:

slope = 7.42 ± 0.22

intercept = 411.1 ± 12.7

Errors are statistical.

The slope (b) and intercept (A) parameters were determined from the merged data and are given in Table. 6.1. These were determined by fitting the data in the intervals,

$$-0.02 > t > -0.34 \qquad (\pi^+ p \to K^+ \Sigma^+)$$

and

$$t\,\mathrm{min} - .005 > t > -0.34 \quad (K^- p \to \pi^- \Sigma^+)$$

The differential cross-section results are listed in Table. 6.2.

Reaction	Decay Mode	Raw No. of events	Slope	Intercept*	Total* Cross-section
$\pi^+ p \to K^+ \Sigma^+$	$n\pi^+$ $p\pi^0$	1406 1151	9.25 ± 0.38	397.1 ± 45.1	40.1 ± 4.5
$K^- p \to \pi^- \Sigma^+$	$n\pi^+$ $p\pi^0$	1348 1137	7.42 ± 0.22	411.1 ± 43.0	60.6 ± 6.8

Table 6.1 The cross-section parameters.

*Errors include a 10% systematic error.

DIFFERENTIAL CROSS SECTION

		$\pi^+ p \rightarrow K^+ \Sigma^+$		$K^- p \rightarrow \pi^- \Sigma^+$	
-t $(Gev/c)^2$		$\frac{d\sigma}{dt}$ $\mu b/(Gev/c)^2$	Δ $\pm$	$\frac{d\sigma}{dt}$ $\mu b/Gev/c)^2$	Δ $\pm$
tmin -0.005	0.020	269.7	47.9	407.3	34.1
0.020	0.040	290.5	22.9	388.6	33.0
0.040	0.080	224.9	13.8	239.1	17.5
0.080	0.120	160.7	11.1	186.9	15.0
0.120	0.160	131.5	10.0	147.4	13.0
0.160	0.200	64.9	6.7	112.4	11.0
0.200	0.240	59.6	6.5	73.7	8.7
0.240	0.290	32.3	4.2	63.4	7.3
0.290	0.340	20.5	3.3	42.1	5.8
0.340	0.440	15.5	2.0	26.3	3.2
0.440	0.600	7.59	1.24	12.9	1.9
0.600	1.000	4.04	0.82	5.66	1.18

Table 6.2 The Differential Cross-sections.

Errors are statistical.

6.4 The Polarization Measurement

In reactions (I) and (II) the Σ^+ can be spin polarized. In such strong interactions, parity conservation implies that the hyperons must be polarized with spin transverse to the production plane. As the Σ^+ decays weakly, parity non-conservation in the decay enables the polarization to be determined.

If θ is the angle between the decay nucleon in Σ rest frame and the normal to the production plane p (beam) X $\underline{p}$ (outgoing meson), then the decay angular distribution is given by [40]

$$f(\theta) = \tfrac{1}{2}(1 + \alpha P \cos\theta) \qquad \text{(I)}$$

where α is the decay asymmetry parameter and P the polarization parameter. Thus the parity violation in the Σ^+ decay is manifest as an up-down asymmetry of the decay nucleon relative to the production plane.

The polarization was determined by two different methods, the up-down asymmetry method and the method of moments.

6.4.1 The Up-Down Asymmetry Method

By integrating the decay angular distribution given by eqn. 6.i, the number of events with the decay nucleon going into the upper hemisphere (w.r.t. the production plane) is

$$\text{Nup} = \int_0^1 f(\theta)\ d(\cos\theta) = \tfrac{1}{2}\left(1 + \frac{\alpha P}{2}\right)$$

and similarly for the lower hemisphere

$$\mathrm{Ndn} = \int_{-1}^{0} f\ (\theta)\ \ d\ (\cos\theta) \ = \ \tfrac{1}{2}\ (1 - \frac{\alpha P}{2})$$

Then the polarization parameter is simply given by

$$P \ = \frac{2}{\alpha} \quad \left(\frac{\mathrm{Nup - Ndn}}{\mathrm{Nup + Ndn}}\right) \qquad 6.\mathrm{ii}$$

The error in P is given by

$$\frac{\Delta P}{P} = \frac{2\ \mathrm{Nup\ Ndn}}{\mathrm{Nup}^2 - \mathrm{Ndn}^2} \sqrt{\frac{1}{\mathrm{Nup}} + \frac{1}{\mathrm{Ndn}}}$$

Because of the smallness of the α parameter ($\alpha = 0.066$) for the $\Sigma^+ \to n\pi^+$ decay mode, only $\Sigma^+ \to p\pi^0$ decay mode data ($\alpha = 0.979$) could be used to determine P.

6.4.2 The Method of Moments

The first moment in cosθ of the angular distribution 6.i yields

$$<\cos\theta> \ = \frac{\alpha P}{3} \qquad 6.\ \mathrm{iii}$$

hence determining P. If P is determined by this method, the error in P is given by

$$\Delta P = \frac{1}{\alpha} \sqrt{\frac{1}{n}\left[3 - (\alpha P)^2\right]}$$

where n is the number of events used to determine P.

It was stated in Chapter 4 that the $\Sigma^+ \to p\ \pi^0$ decay mode suffered from losses not only due to short Σ^+ length but also from small angle decays. These losses tend to be symmetric about zero in $\cos\theta^*$ as is illustrated by Fig. 6.4.

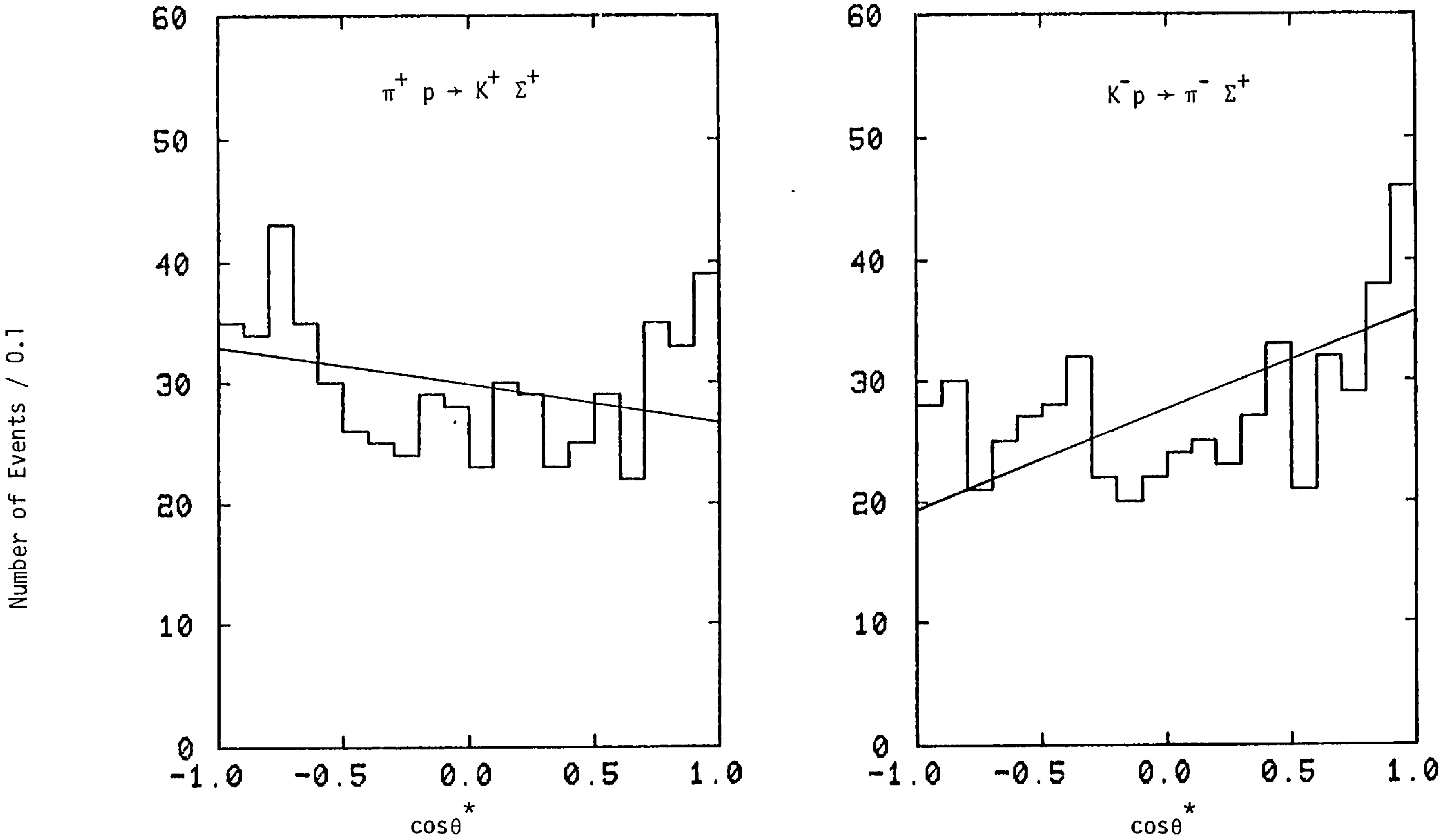

Fig. 6.4 $\cos\theta^*$ distribution for $\Sigma^+ \rightarrow p\pi^0$ decay in Σ rest frame for $|t| < 0.1$ Gev/c.

The solid line represents the polarization as determined by the weighted method of moments.

These losses can be corrected for by taking the second moment of the decay angular distribution which yields,

$$<\cos^2\theta> = 1/3$$

Eqn. 6.iii can now be rewritten as

$$P = \frac{1}{\alpha} \frac{<\cos\theta>}{<\cos^2\theta>} \qquad 6.\text{iv}$$

and

$$\Delta P = \frac{3}{\alpha} \sqrt{\frac{<\cos^2\theta> - <\cos\theta>}{n}}$$

This method for obtaining polarization values was preferred to the others. In fact all methods gave results which were consistent with each other. The polarization values that were obtained are listed in Table 6.3 and are illustrated in Fig. 6.5.

POLARIZATION

		$\pi^+ p \rightarrow K^+ \Sigma^+$		$K^- p \rightarrow \pi^- \Sigma^+$	
-t $(Gev/c)^2$		P	ΔP	P	ΔP
-0.0	0.01			0.02	0.17
0.01	0.05	0.02	0.12	-0.10	0.10
0.05	0.10	0.10	0.10	-0.25	0.13
0.10	0.20	0.12	0.10	-0.25	0.11
0.20	0.30	0.30	0.15	-0.38	0.13
0.30	0.50	0.55	0.17	-0.39	0.17
0.50	1.00	0.49	0.25	-0.62	0.28

Table 6.3 The Hyperon Polarization.

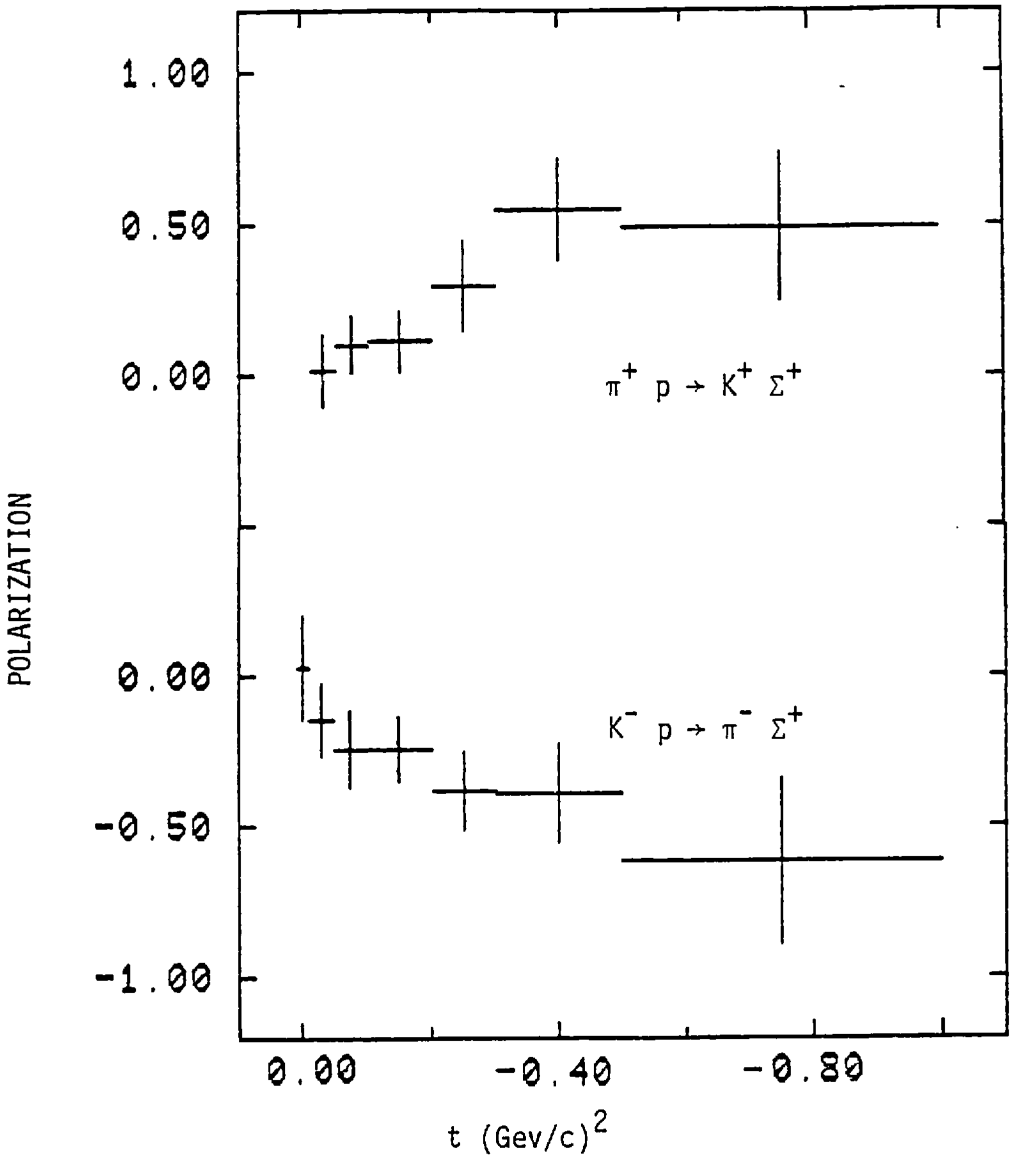

Fig. 6.5 The Σ^+ Polarization

CHAPTER 7

Discussion and the Implication of the Results

7.1 Introduction: $0^- \frac{1}{2}^+ \rightarrow 0^- \frac{1}{2}^+$ Scattering

In relativistic interactions involving particles with spin, it is advantageous to use the helicity representation for angular momentum. Helicity is the component of spin of a particle along its direction of motion.

In the two body scattering processes we are studying, namely,

$$0^- \tfrac{1}{2}^+ \rightarrow 0^- \tfrac{1}{2}^+$$

there are four helicity amplitudes

$$H_{++},\ H_{+-},\ H_{-+},\ H_{--}$$

Where the first and second subscripts represent the baryon helicity ($\pm \frac{1}{2}$) before and after the interaction respectively. Since strong interactions conserve parity, H_{++} and H_{--}, H_{+-} and H_{-+} are related. Thus we are left with two independent helicity amplitudes:

H_{++} the helicity non-flip amplitude

and

H_{+-} the helicity flip amplitude

In general these amplitudes are complex. In this experiment we can only determine two independent quantities which, in terms of the helicity amplitudes, are

$$\frac{d\sigma}{dt} = \left|H_{++}\right|^2 + \left|H_{+-}\right|^2 \qquad 7.i$$

and

$$P\,\frac{d\sigma}{dt} = -\,2\ \mathrm{Im}\,(H_{++}\,H_{+-}^{\,*}) \qquad 7.ii$$

Thus to estimate the amplitudes up to an overall phase we have to do an "amplitude analysis" based on some plausible assumptions.

The Regge description of high energy two-body scattering processes provides us with a parameterization of the amplitudes. This is introduced in the next section.

7.2 The Regge Pole Parameterization [4]

Asymptotically, the contribution of a single t - channel Regge pole at $\alpha(t)$ to an s-channel helicity amplitude for the process (Fig. 7.1)

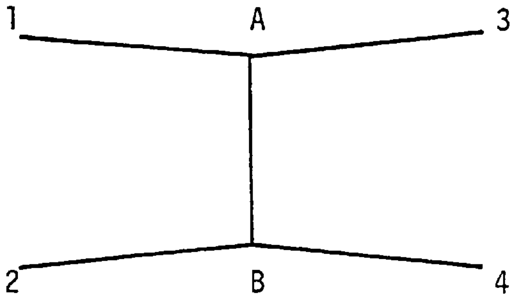

Fig. 7.1

is given by:

$$T(s,t) = g_A(t)\ g_B(t)\ (\sqrt{t - t_{min}})^n\ \frac{1 + \tau\, e^{-i\pi\alpha(t)}}{\sin \pi\alpha(t)} \left(\frac{S}{So}\right)^{\alpha(t)} \qquad 7.iii$$

where

s is the c.m. energy and s_o is a constant scale factor,

$\alpha(t)$ is the Regge trajectory function,

$\tau(= \pm 1)$ is the signature of the pole,

$(t - tmin)^n$ is the kinematic factor taking account of particle spins with n being the net helicity flip,

and the product $g_A(t)\ g_B(t) = \beta(t)$ is the Regge pole residue which factorises into the two vertex functions.

Some features of the data presented in Chapter 6 are now discussed and comparisons with predictions of Regge phenomenology are also made.

7.3 Energy Dependence of the Differential Cross-sections

At high energies, the s-channel differential cross-section for reaction 1 + 2 → 3 + 4 (Fig. 7.2) may be expressed as

$$\frac{d\sigma}{dt} = \frac{d\sigma}{d\Omega}\ \frac{d\Omega}{dt}$$

where

$$d\Omega = 2\pi\ d(\cos\theta_s)$$

and

$$\cos\theta_s \sim \frac{t}{s}$$

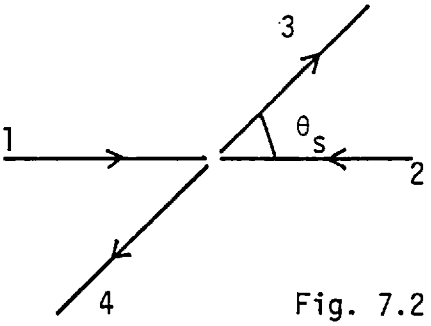

Fig. 7.2

In terms of the invariant scattering amplitude

$$\frac{d\sigma}{d\Omega} \sim \left| \frac{1}{\sqrt{s}} \; T(s,t) \right|^2$$

implying

$$\frac{d\sigma}{dt} \sim \frac{1}{s^2} \left|T(s,t)\right|^2$$

Assuming a single dominant Regge pole exchange, and by substituting for T(s,t) from Eqn. 7.iii, we obtain

$$\frac{d\sigma}{dt} \sim f(t) \; s^{2\alpha(t) - 2}$$

To make tests of Regge energy dependence, dσ/dt can be parameterized in terms of an effective trajectory, $\alpha\mathrm{eff}(t)$,

$$\frac{d\sigma}{dt} \sim f(t) \; s^{2\alpha\mathrm{eff}(t) - 2} \qquad 7.\mathrm{iv}$$

As extracted from the data, $\alpha\mathrm{eff}$ should lie close to the trajectory of the dominant exchanged singularity as a fuction of t. Taking the logarithm of eqn. 7.iv we obtain:

$$\ln\left(\frac{d\sigma}{dt}\right) = \ln \; f(t) + (2\,\alpha\mathrm{eff}(t) - 2)\,\ln s$$

The difference in differential cross-section at two energies allows us to extract $\alpha\mathrm{eff}(t)$, which has the form

$$\alpha\mathrm{eff}(t) = 1 + \frac{1}{2} \; \frac{\ln\left[\left(d\sigma/_{dt}\right)_2 \;\; / \;\; d\sigma/_{dt}\right)_1\Big]}{\ln\,(S_2/S_1)} \qquad 7.\mathrm{v}$$

For another energy, we have used data from an experiment at 11.5 Gev/c which also studied reactions I to IV. This experiment was carried out by the SLAC Bubble Chamber Group on the same apparatus. Data at both momenta, 7 and 11.5 Gev/c, were taken in collaboration but were analysed independently. Consequently relative systematics were smaller than if the experiments were completely independent. Hence no other data was used to extract αeff(t). Fig. 7.3 shows αeff(t) as determined by reactions I and II. The solid line is drawn such that it passes through the particles $K^*(890)$ and $K^*(1420)$. Both are not inconsistent with a linear trajectory (solid line) passing through the $K^*(890)$ and $K^{**}(1420)$ poles. This is to be expected for reactions dominated by vector (K^*) and tensor (K^{**}) Regge pole exchanges.

7.4 Energy Dependence of Total Cross-sections

Unequal mass kinematics lead to corrections when comparing the measured cross-sections for reactions (I) and (II). In both cases tmin approaches zero as the energy increases, but this increases the low t phase space available for the K^- reaction and decreases it for the π^+ reaction. To account for this kinematic effect the exponential fit has been used to correct for the measured cross-sections by

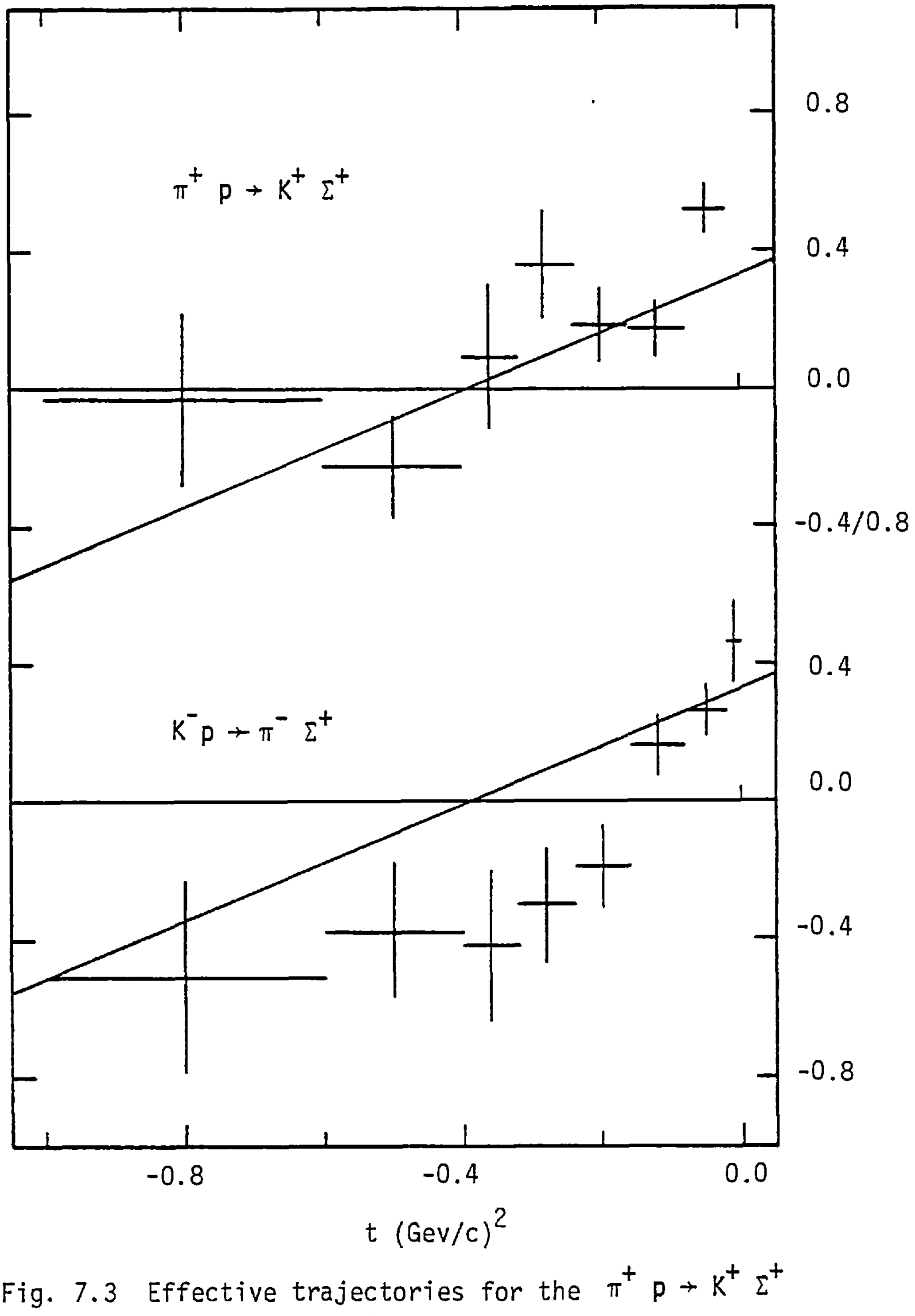

Fig. 7.3 Effective trajectories for the $\pi^+ p \rightarrow K^+ \Sigma^+$ and $K^- p \rightarrow \pi^- \Sigma^+$ reactions between 7 and 11.5 Gev/c.

$$\int_{tmin}^{0} A\, e^{bt}\, dt$$

This correction increases the π^+ cross-sections and decreases the K^- ones.

Fig. 7.4 illustrates the integrated ($-t<1.0$) cross-sections for reactions I and II. Data from high statistics and low systematic uncertainty experiments were used wherever possible.[26-35] The K^- cross-section is higher than π^+ but the difference is getting smaller with P_{lab} as the K^- cross-section is falling more rapidly than the π^+. To quantify this behaviour the conventional parameterization $\sigma \propto P_{lab}^{-n}$ has been used. Neglecting the preliminary point at 70[26] Gev/c we find $n = 0.99 \pm 0.05$ for $\pi^+ p \rightarrow K^+ \Sigma^+$ and $n = 1.34 \pm 0.06$ for $K^- p \rightarrow \pi^- \Sigma^+$.

The point at 70 Gev/c seems to suggest that the π^+ cross-section starts falling as rapidly as the K^- when equality of the two cross-sections is obtained. Further results should clarify the situation since reaction $K^- p \rightarrow \pi^- \Sigma^+$ has also been studied in the same experiment.

7.5 Shrinkage [2]

Since $\frac{d\sigma}{dt}$ seems to fall roughly exponentially for small $|t|$ in many processes we can approximate the residue by an exponential so that eqn. 7.iii becomes :

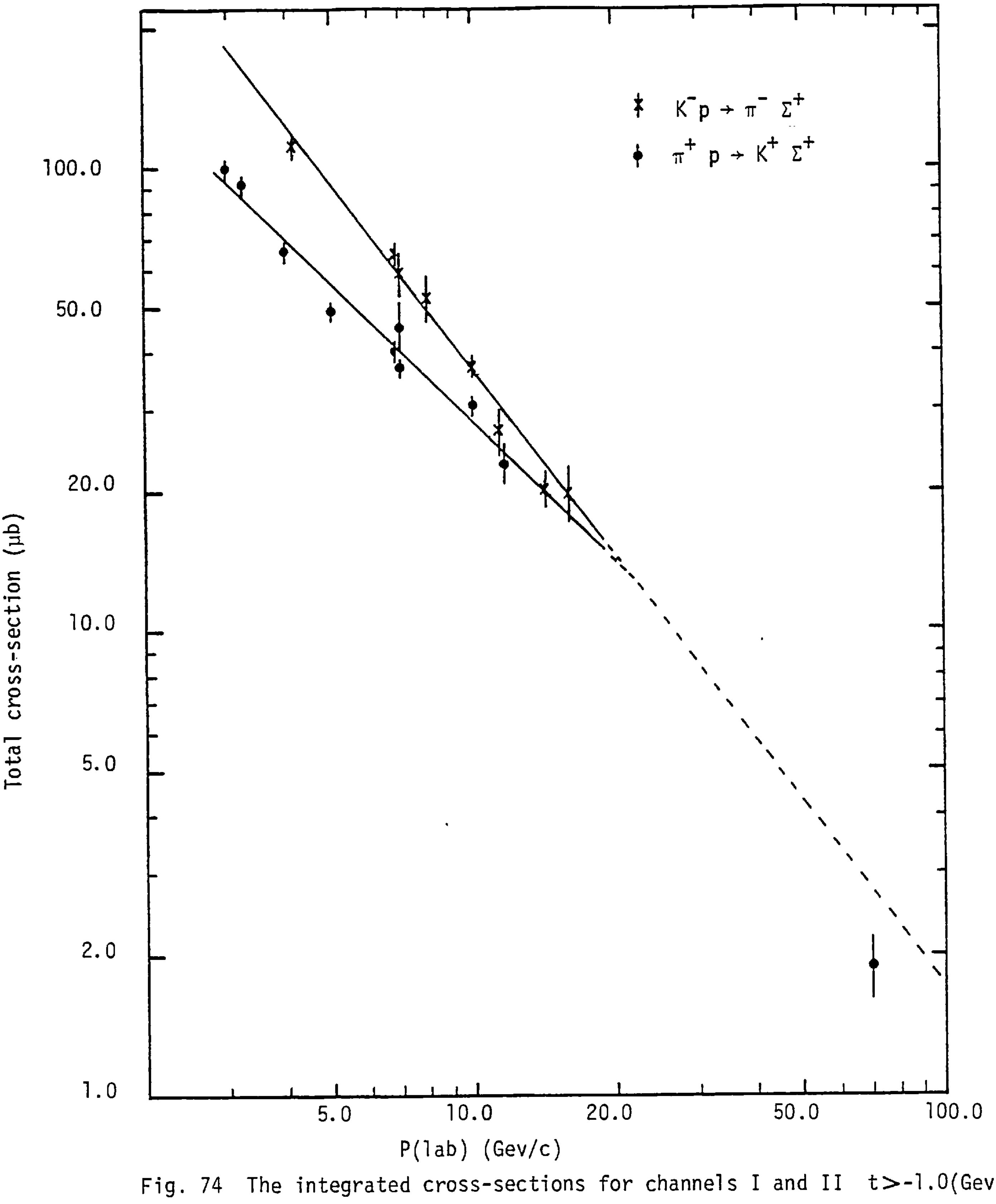

Fig. 74 The integrated cross-sections for channels I and II $t > -1.0(\mathrm{Gev}/c)^2$

The fit (solid line) parameters are:
$n(\pi^+) = 0.99 \pm 0.05$
$n(K^-) = 1.34 \pm 0.06$

The point at 70 Gev/c was not part of the fit.

$$T\ (s,t) = G\ e^{at} \left(\frac{s}{so}\right)^{\alpha(t)} \qquad 7.vi$$

Assuming there exists an approximately linear trajectory of the form

$$\alpha\ (t) = \alpha\ (o) + \alpha\ t$$

7.vi may be rewritten as

$$T(s,t) \sim G \left(\frac{s}{so}\right)^{\alpha(o)} e^{\left[a + \alpha' \ \ell n\left(\frac{s}{s_o}\right)\right]t}$$

$$= G \left(\frac{s}{so}\right)^{\alpha\ (o)} e^{bt}$$

where $b = a + \alpha' \ \ell n \left(\frac{s}{so}\right)$ is the slope parameter. Thus the slope increases with s. This is known as shrinkage and Fig. 7.5 shows that reactions I and II do exhibit shrinkage.

It may be interpreted as an increase in the effective size of the target, but as the cross-sections do not increase the target is evidently becoming more 'transparent' as the energy increases.

However some reactions do not exhibit shrinkage.

7.6 Factorisation and Line Reversal [2]

It is expected that Regge pole residues will factorize into a contribution to each vertex so that for a t - channel pole

$$\beta_{12 \rightarrow 34}(t) = \beta_{13}(t).\beta_{24}(t)$$

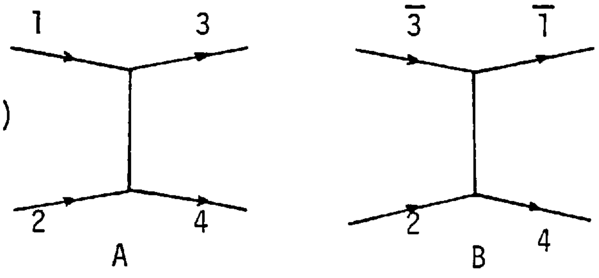

Fig 7.6

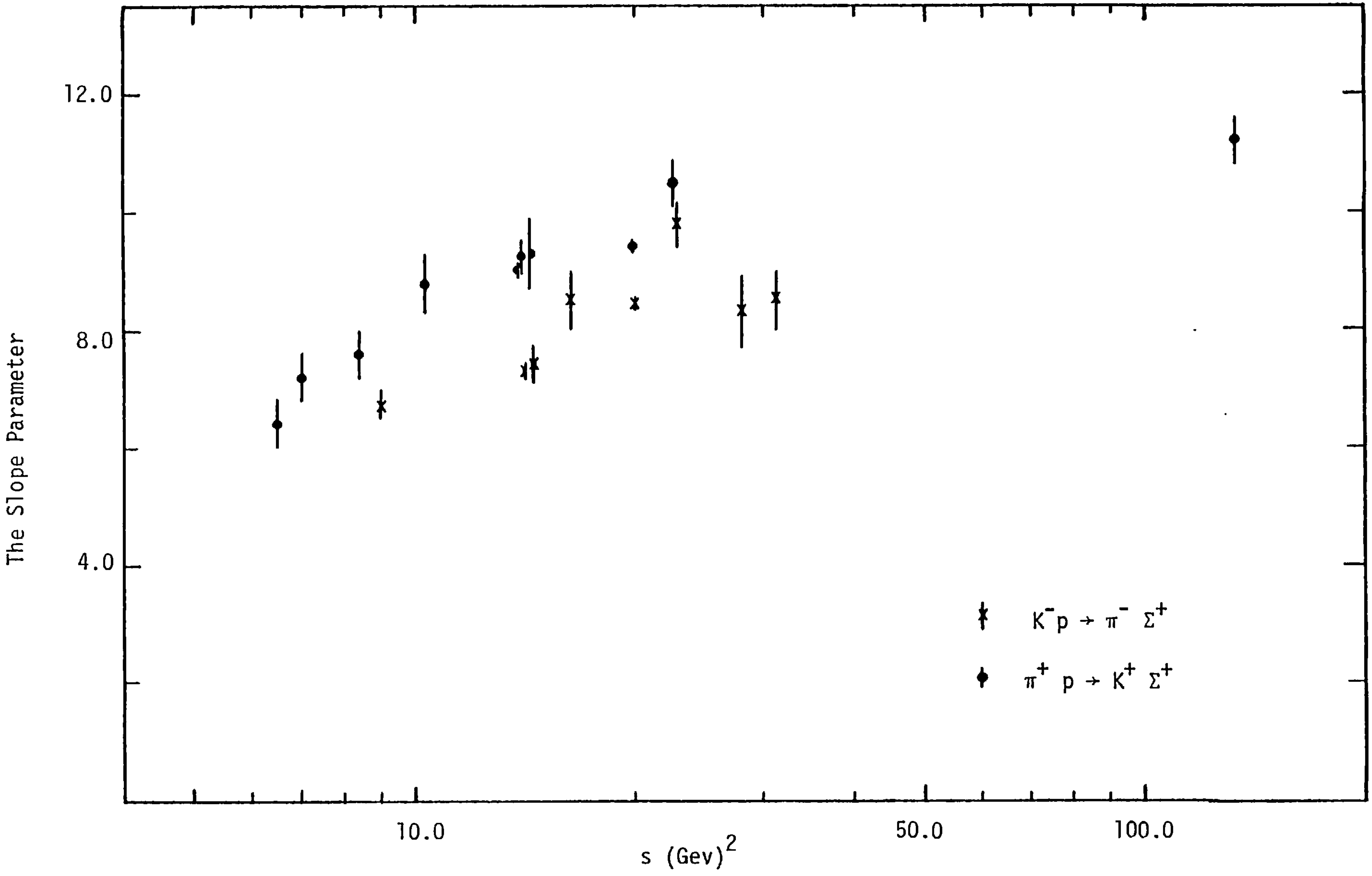

Fig. 7.5 The slope parameter.[25 – 36]

An important consequence of factorization is line reversal symmetry. Consider reactions

$$1 + 2 \rightarrow 3 + 4 \qquad \text{(A)}$$

and $$\bar{3} + 2 \rightarrow \bar{1} + 4 \qquad \text{(B)}$$

They differ only by a rotation and time reversal at the 1 - 3 vertex. Strong interactions are invariant under these changes. Thus the latter process will have exactly the same Regge pole exchanges, with the same couplings. In fact process (B) is the u - channel of process (A). Thus line reversal symmetry is equivalent to crossing from the s - channel to the u - channel.

In our experiment, where $1 = \pi^+$, $2 = p$, $3 = K^+$ and $4 = \Sigma^+$, the possible exchanges are $K^*(890)$ and $K^{**}(1420)$ poles which have odd and even signatures respectively. Thus the Regge pole exchanges for processes I and II, up to a relative sign, can be written as

$$K^{**} \pm K^* \qquad \text{7.vii}$$

7.7 Exchange Degeneracy (EXD)

EXD was introduced in Section 1.5. A somewhat more detailed description is now given.

The occurrence of exchange degenerate pairs of Regge poles was related to the exoticity of the direct channel. In our case neither reaction I nor II has an exotic direct channel.

Consider $\pi^+ K^+$ backward scattering.[6] The Feynman diagram of the process is

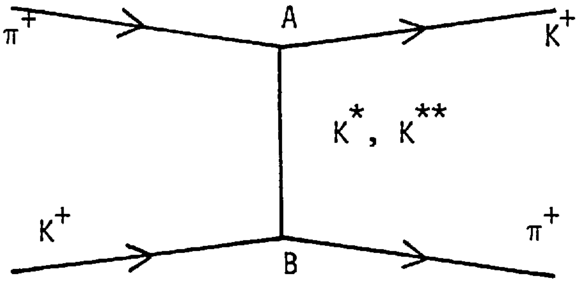

Fig. 7.7

The allowed exchanges are K^* and K^{**} Regge poles. The Regge amplitude may be written as

$$A \sim K^* + K^{**}$$

Since the s - channel for the above process is exotic, the s - channel amplitude has to be purely real. This will only happen if the K^* and K^{**} contributions cancel each other in the imaginary part i.e. K^* and K^{**} trajectories are exchange degenerate and the residues have equal modulii.

In reaction channel I, since the allowed exchanges are the same, vertex A in Fig. 7.7 is identical to vertex A in Fig. 7.8

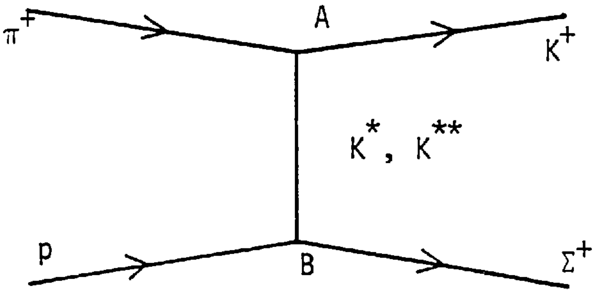

Fig. 7.8

Similarly by considering $p\Sigma^+$ backward scattering, where the s - channel is also exotic, p and Σ^+ at vertex B in Fig. 7.8 will also couple to exchange degenerate K^* and K^{**}.

Factorization now tells us that the allowed exchanges in channels I and II, K^* and K^{**}, should be exchange degenerate.

If we parametrise the K^* and K^{**} Regge poles as

$$K^* = \beta(t)\left(1 - e^{-i\pi\alpha_1(t)}\right)\left(\frac{s}{so}\right)^{\alpha_1(t)}$$

and

$$K^{**} = \beta(t)\left(1 + e^{-i\pi\alpha_2(t)}\right)\left(\frac{s}{so}\right)^{\alpha_2(t)}$$

then the EXD prediction, which is that

$$\beta_1(t) = \beta_2(t) = \beta(t)$$

and $\alpha_1(t) = \alpha_2(t) = \alpha(t)$

implies that the amplitudes for processes I and II should be given by, using 7.vii,

$$T(a) = 2\beta(t)\left(\frac{s}{so}\right)^{\alpha(t)}$$

$$T(b) = -2\beta(t)\left(\frac{s}{so}\right)^{\alpha(t)} e^{-i\pi\alpha(t)} \qquad 7.\text{viii}$$

Which process has the purely real amplitude can be ascertained by using duality diagrams.[3] If a certain process cannot be described by an s - t planar diagram (i.e. quark lines do not cross), then the imaginary part of the t - channel exchanges is predicted to vanish. In our case the duality diagrams for processes I and

II are shown in Fig. 7.9.

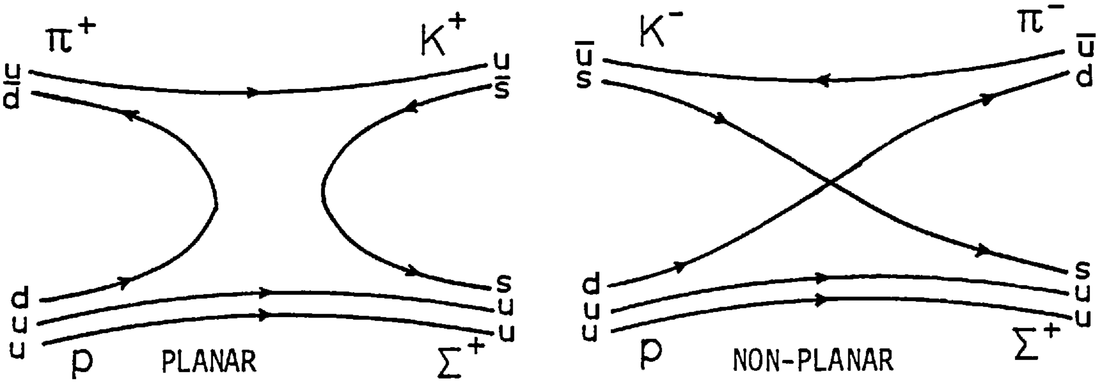

Fig. 7.9

Thus the forward amplitude for $K^- p \rightarrow \pi^- \Sigma^+$ should be real corresponding to T(a).

Since a Regge pole gives the same phase to all helicity amplitudes, the amplitude relations 7.viii give zero hyperon polarization and equal differential cross-sections for reactions I and II.

Clearly our polarization data at both 7.0 and 11.5 Gev/c (Fig. 7.16) are in conflict with this polarization prediction. In fact all polarization data for channels (I) and (II) to date are in conflict with the prediction.

There are two kinematic regions in which EXD can be tested: $t > o$ and $t < o$. The Chew-Frautschi plot for $K^*(890)$, $K^*(1420)$ and $K^*(1780)$ shows degeneracy in $t > o$ region (Fig. 7.10.). However, the polarization data suggest that simple EXD in the scattering region $(t < o)$ seems to be broken.

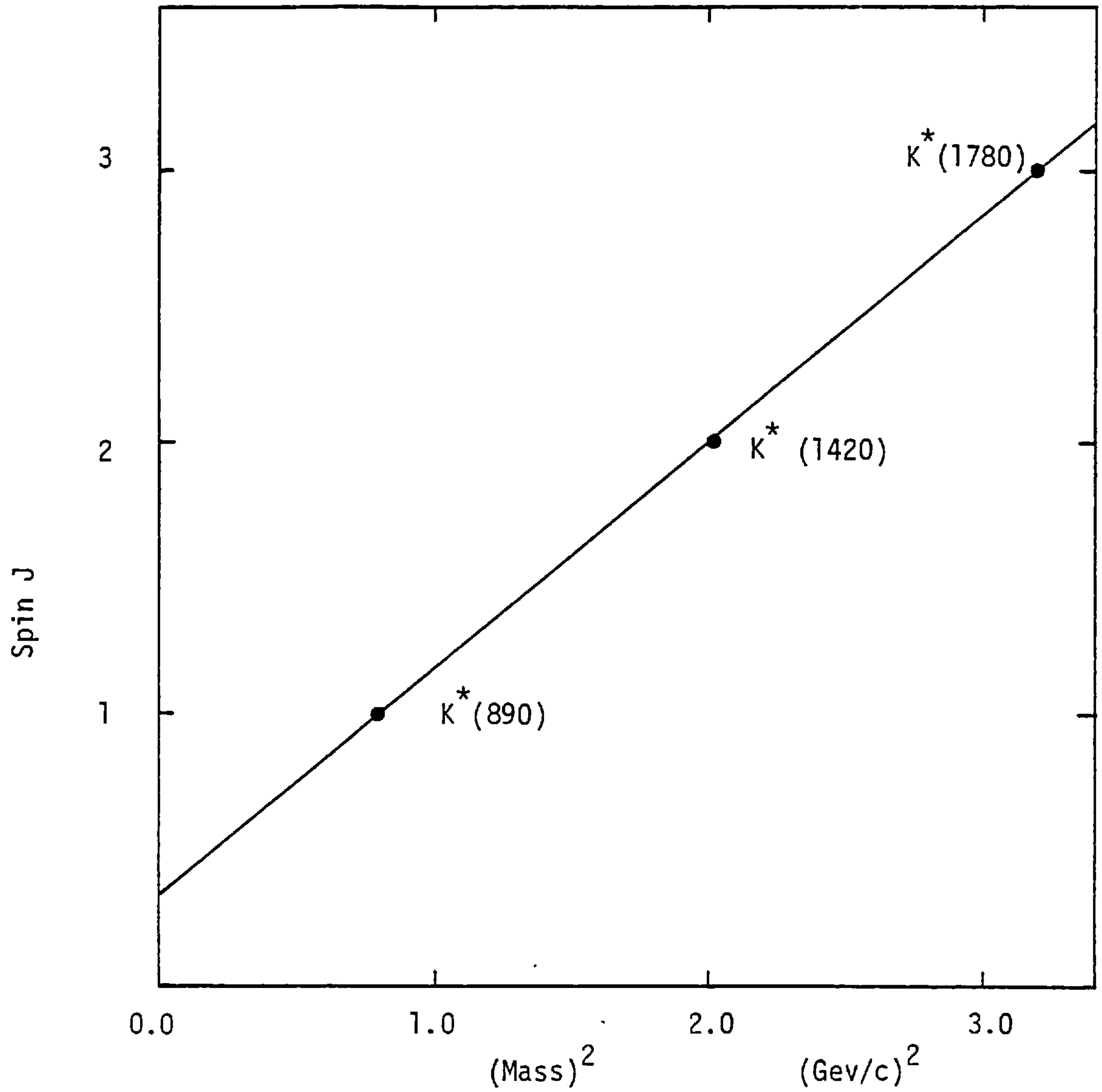

Fig. 7.10 The Chew- Frautschi Plot for the K^*'s in the region $t>0$. The solid line is to guide the eye.

In trying to get agreement with data, there are two distinct models, the names of which ('strong' and 'weak') suggest the amount of absorption (see section 7.9) put in. The predictions of these models based on exchange degeneracy were outlined in section 1.6.

In strong EXD it is assumed that the residues and the trajectory functions are identical for K^* and K^{**} Regge amplitudes. Thus the predictions for polarization and differential cross-sections are the same as for simple EXD, and hence in gross disagreement with data.

In weak EXD only the trajectory functions are assumed to be identical. The polarization is then predicted to be equal in magnitude but opposite in sign for reactions I and II. To examine this polarization prediction we have summed the polarization of the two channels at both energies. Fig. 7.11illustrates that the polarization data at both energies are consistent with zero and thus in agreement with weak EXD.

To test the predicted equality of the differential cross-sections for channels I and II, it is convenient to look at the ratio defined by

$$R = \frac{\frac{d\sigma}{dt}(K^-) - \frac{d\sigma}{dt}(\pi^+)}{\frac{d\sigma}{dt}(K^-) + \frac{d\sigma}{dt}(\pi^+)} \qquad 7.ix$$

as a function of -t. The prediction of strong and weak EXD is that R = 0.

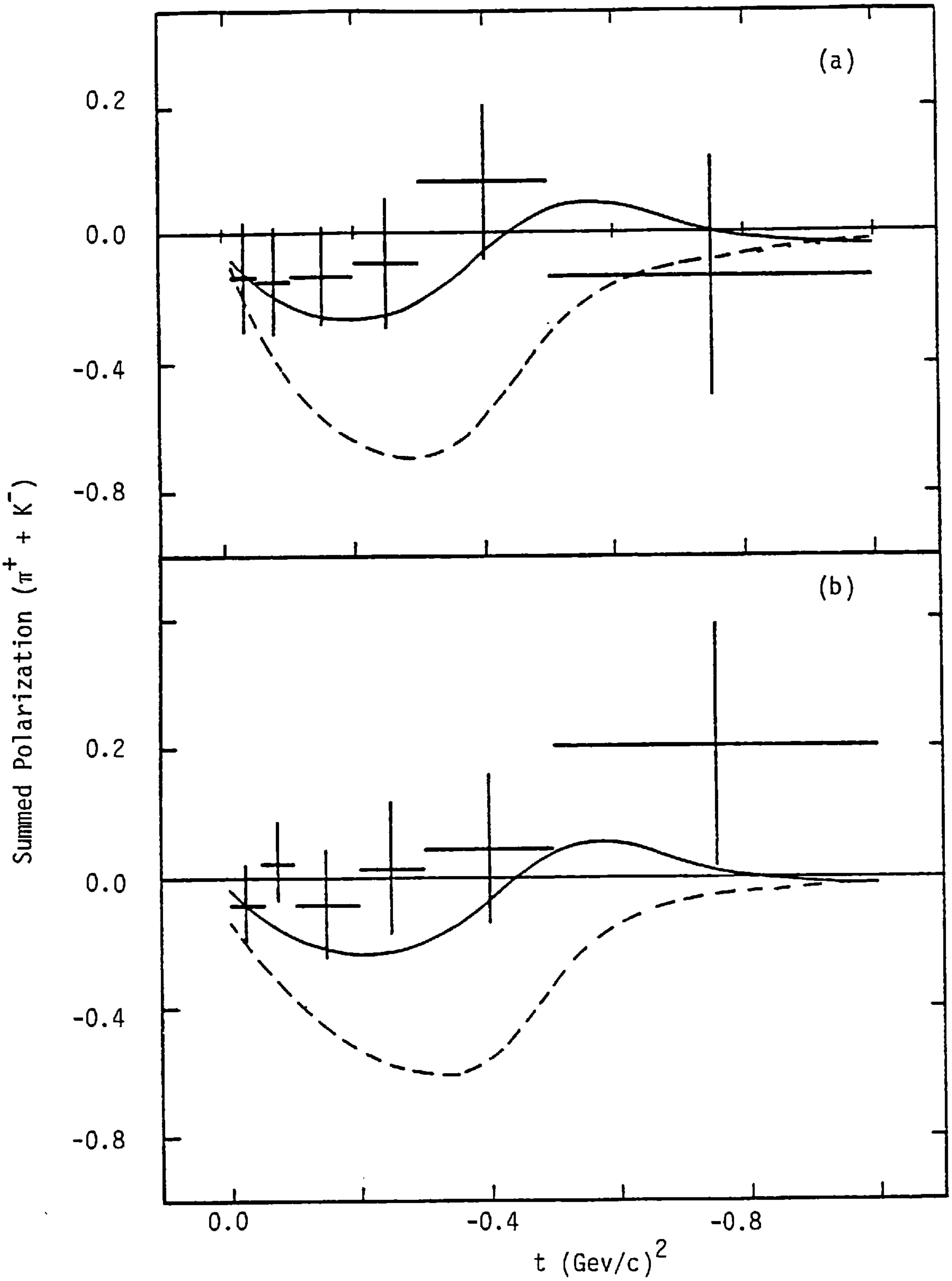

Fig 7.11 Summed Polarization at (a) 7.0 Gev/c and (b) 11.5 Gev/c. The solid curve is the prediction of our fit to $\pi^+ p \rightarrow K^+ \Sigma^+$ and $K^- p \rightarrow \pi^- \Sigma^+$ data above 7.0 Gev/c based on the model of Navelet and Stevens (N-S) Ref. 37. The dashed curve is the prediction of the model of N-S.

Figs 7.12, 13a. illustrate the ratio for I and II at 7.0 and 11.5 Gev/c. The EXD degeneracy violation seems to be decreasing with energy. The only other group which has studied the line reversed reactions I and II is a missing mass experiment of Berglund et al. Their data were taken at 7.0 and 10.1 Gev/c. Although their experiment shows a higher violation of EXD at both energies, within experimental errors both sets of data are consistent.

7.8 EXD Violation

In Chapter 6 it was noticed that the differential cross-sections for reactions I and II did not show any turnover at low t . This indicates that the spin non-flip amplitude is the dominant one, at least at low momentum transfer. However, data on reactions

$$\pi^+ p \to K^+ Y^*(1385) \qquad \text{III}$$

$$K^- p \to \pi^- Y^*(1385) \qquad \text{IV}$$

show a turnover in the forward direction, indicating the dominance of the spin-flip amplitude at low $|t|$. We can use these two pairs of line reversed reactions to establish the spin dependence, if any, of EXD violation.

Figs 7.12, 13b. show R (eqn. 7.ix) as a function of t for III and IV for the SLAC Hybrid Facility experiments at 7.0 (our) and 11.5 Gev/c (SLAC). The data shows a rise at low $|t|$ at both energies. The 11.5 Gev/c data at higher $|t|$ are consistent with R = 0 while the 7.0 Gev/c data is not. Most of the rise at low $|t|$ is of

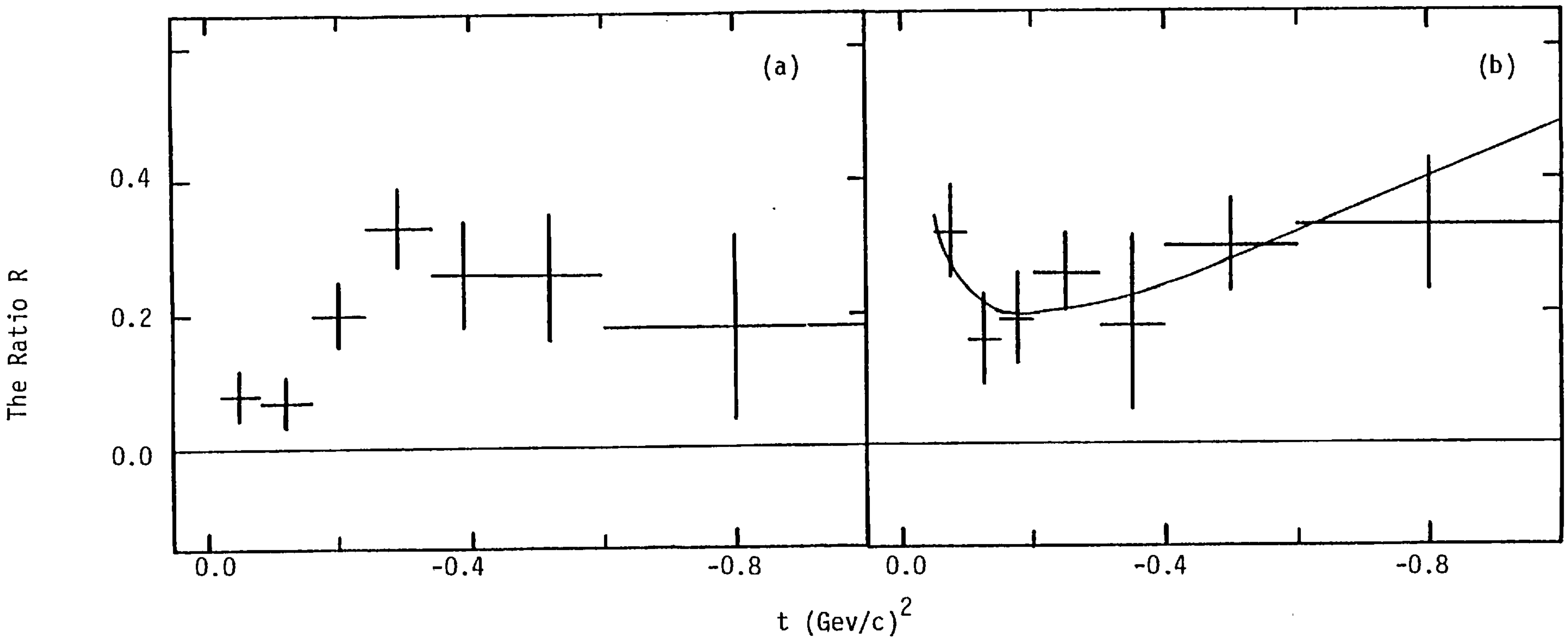

Fig. 7.12 The ratio R at 7.0 Gev/c

(a) $\pi^+ p \rightarrow K^+ \Sigma^+$

(b) $\pi^+ p \rightarrow K^+ Y^*$ (1385)

The solid line has been calculated using the results of fits to the differential cross-sections (see text).

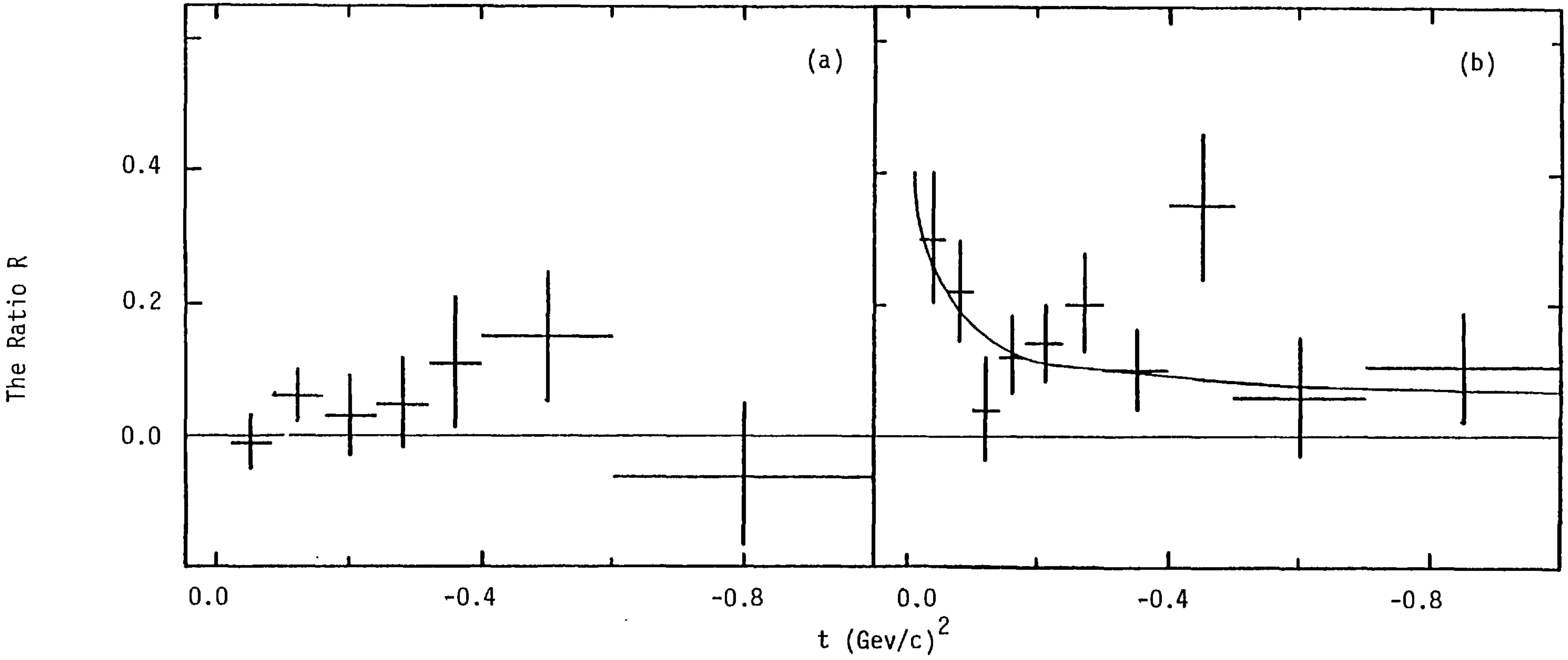

Fig. 7.13 The ratio R at 11·5 Gev/c

(a) and (b) as on Fig. 7.12

kinematic origin. Angular momentum conservation forces the two Y* cross-sections to turn over at different values of momentum transfer thus yielding different cross-sections at low $|t|$. Fits to the differential cross-sections with the form

$$\frac{d\sigma}{dt} = \left[A_1 - A_2(t - tmin)\right] e^{bt}$$

were made. The solid lines in Figs 7.12b and 7.13b have been calculated using the results of the fits.

These results in conjunction with Fig. 7.12 suggest that EXD breaking decreases with energy and that the extent of the breaking is similar for both spin-flip and spin non-flip amplitudes. Most of the results outlined here are consistent with the experiment of Berglund et al., apartfrom their observation of a much larger difference in the Y* differential cross-sections (hence larger R) at 10.1 Gev/c. (Figs 7.12,13). The picture will be clearer when the missing mass experiment of Arenton et al[26], which has studied reactions I to IV at 7 0 Gev/c is completed.

7.9 Amplitude Analysis

As mentioned in section 7.1, in order to extract the helicity amplitudes for processes I and II (when studied on an unpolarized target) an amplitude analysis, with plausible assumptions supplementing the incomplete set of observables, has to be made. Thus the extraction becomes model dependent.

As data on various two body reactions accumulated it was found that the simple Regge pole models using only leading Regge exchanges could not fully describe the data. Polarizations which depend on the interference of helicity flip and non-flip amplitudes and thus provide more sensitive tests of amplitude structure, presented serious problems for these models. As an example, a single Regge pole (ρ) dominates both helicity amplitudes in the reaction $\pi^- p \rightarrow \pi^0 n$ thus predicting that polarization of the recoil nucleon be zero. Experimentally it is not.[38] Corrections to the simple Regge amplitude parameterization (7.iii) were found necessary.

The non-pole corrections are expected to interfere destructively with the Regge pole and have a flatter t - dependence than the pole. In general these corrections tend to sharpen the forward peak in $\frac{d\sigma}{dt}$, thus making the exchange amplitudes more 'peripheral'.[8] Amplitude peripherality can be understood in terms of absorption which is based on the hypothesis that the particles taking part in, say, a hypercharge exchange reaction, being hadrons, may undergo some strong interaction before or after the basic HYCEX reaction. This can be related to Regge cuts which arise from the exchange of two (or more) Reggeons as shown in Fig. 7.14.

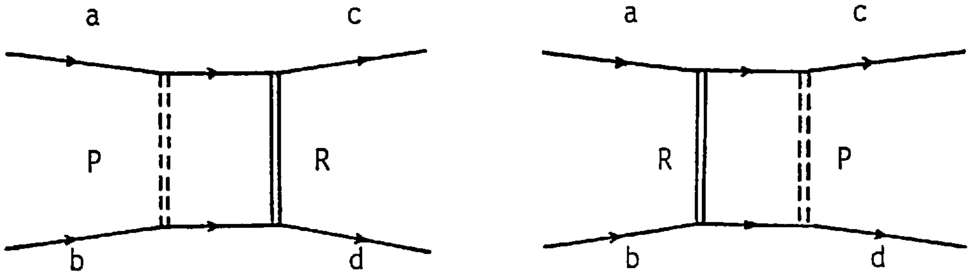

Fig. 7.14

Absorption tends to depress amplitudes at low impact parameters. For a typical helicity non-flip Regge amplitude, N(s,t), the dominant t dependence is roughly exponential. For a given s,

$$N(t) \; \alpha \; e^{at} = e^{-aq^2}$$

where $q = \sqrt{-t}$ and $a > o$.

In the impact parameter (b) space, N(t) transforms into a Gaussian

$$N(b) \; \alpha \; \int_{\infty}^{\infty} e^{-aq^2} \; e^{iqb} \, dq$$

$$= \; e^{-b^2/4a} \int_{\infty}^{\infty} e^{-a(q - ib/2a)^2} \, dq$$

$$\alpha \; e^{-b^2/4a}$$

(by Cauchy's Theorem)

Similarly, the helicity flip amplitude, F(t), of the form transforms to

$$F(t) \; \alpha \; \sqrt{-t} \; e^{at}$$

$$F(b) \; \alpha \; b \, e^{-b^2/4a}$$

The profiles of these amplitudes are illustrated in Fig. 7.15. If absorption is represented by the curve in Fig. 7.15 a, then the helicity non-flip amplitude is greatly modified while the flip amplitude hardly changes, as is illustrated in Fig. 7.15b and 7.15c.

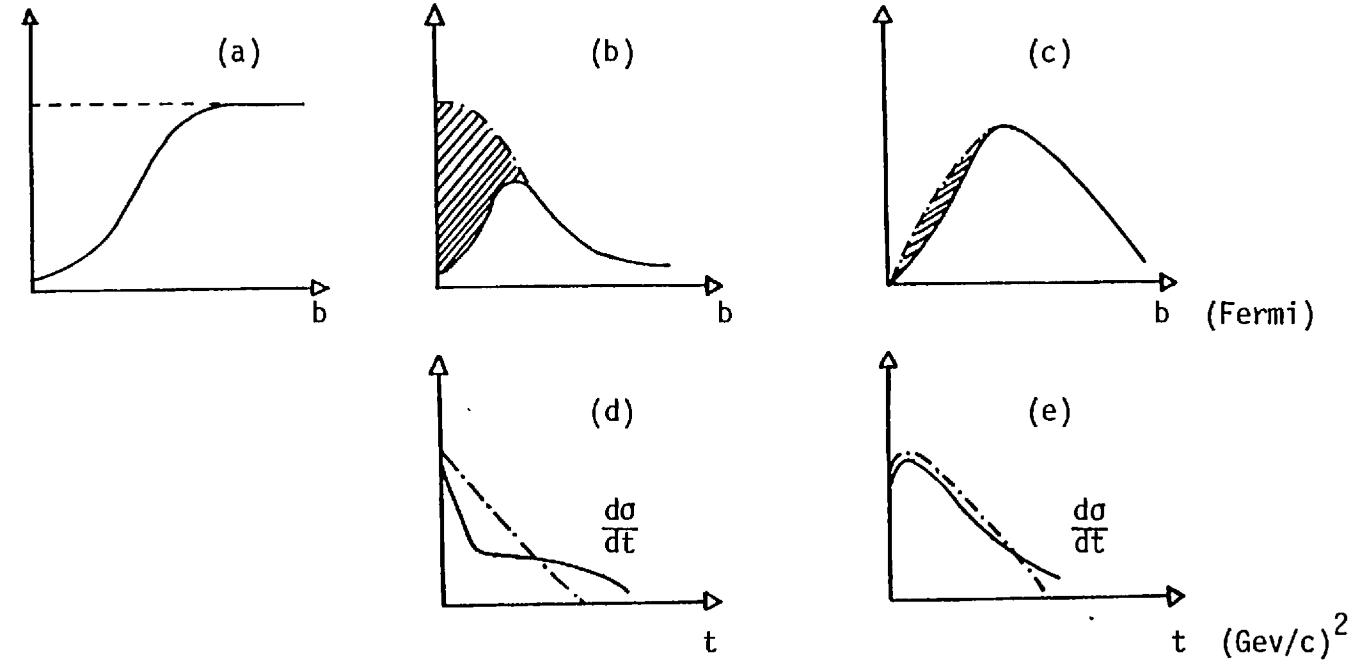

Fig. 7.15 The Effects of Absorption[8] —·—·— before , ——— after absorption.

(a) the absorption function. b is the impact parameter.

(b),(d) non-helicity flip amplitude in b-space.

(c),(e) helecity flip amplitude.

The shaded regions represent absorption. The effect on differential cross-sections is shown in (d) and (e).

Thus in most absorption and cut models, the helicity-flip amplitude is assumed to be Regge pole dominated and corrections are applied to the non-flip amplitude.

We shall now confront our data with a recently performed amplitude analysis of Navelet and Stevens.

7.9.1 The Model of Navelet and Stevens (N-S), (1975)[37].

The model fitted all published $0^- \frac{1}{2}^+ \to 0^- \frac{1}{2}^+$ HYCEX data. They used loosely parameterised Regge poles for flip amplitudes and pole + effective cuts for non-flip amplitudes following the results for ρ and A_2 exchange.

They parameterized the pole amplitudes as

$$H_{++} = K\,\gamma_{++}\left(\tau + e^{-\,i\pi\alpha(t)}\right) S^{\,\alpha(t)}\, e^{a_{++}t}$$

and $H_{+-} = K\sqrt{-t}\;\gamma_{+-}\left(\tau + e^{\,-i\pi\alpha(t)}\right) S^{\alpha(t)}\, e^{a_{+-}t}$

where $K^2 = \dfrac{0.38935\ M^2}{16\pi P_i^2\ S}$ mb/(Gev/c)^2

$$\sqrt{-t} = \sqrt{-(t - t\text{min})}$$

The a's and residues are considered different for Λ and Σ channels.

Their effective cut amplitudes, inspired by cut amplitudes as calculated for a 2-Reggeon cut,[2] read

$$H_{++} = K\,\gamma_{++}\,\gamma^{c}\begin{pmatrix} i \\ -i \end{pmatrix}\left(e^{-i\pi/2}\, S\right)^{\alpha_c(t)}\, e^{a_c t}$$

where i is for vector exchange

- 1 is for tensor exchange

and γ^c is the effective-cut strength relative to the pole.

The calculated cuts have an additional s dependent term given by

$$\frac{1}{\log \frac{s}{so} + d}$$

where d is a constant. Also if the cuts are assumed to be generated by Pomeron exchange (conventional absorption models) then the cut trajectory in the calculation should have the form

$$\alpha_c(t) = \alpha(o)_1 + \alpha(o)_2 - 1 + \frac{\alpha_1' \ \alpha_2'}{\alpha_1' + \alpha_2'} t$$

where α_1' ,α_2' are the slopes of Regge and Pomeron trajectories. Since α_p (0) $\sim$ 1.

$$\alpha_c(o) = \alpha_R(o)$$

and also

$$\alpha_c' < \alpha'_R$$

N-S allowed the parameters in the cut amplitudes to vary in order to examine the nature of the cuts.

The overall sign convention is such that, in the limit of exchange degeneracy, K^*_V - K^*_T would have a positive imaginary part.

Their parameterization describes the low energy (< 7.0 Gev/c) HYCEX data fairly well. Recent polarization data at 5.0 Gev/c for $\pi^- p \rightarrow K^0 \Lambda$,[39] is also in good agreement with the predictions.

Their predictions for polarization in reactions I and II at 7.0 and 11.5 Gev/c are compared with our data in Fig. 7.16. The predictions seem roughly consistent with the data, especially at high $|t|$. However, when the polarizations for channels I and II are summed and then compared with the model predictions (dotted line in Fig. 7.11), the disagreement is obvious especially in the range $-0.1 < t < -0.5$ $(\text{Gev/c})^2$.

The predicted sum is strongly negative because effective cuts were partly used to reproduce polarizations that had the same sign at low $|t|$ for the line reversed reactions, as suggested by the low energy HYCEX data. Our data (7.0 and 11.5 SLAC data for $\pi^+ p \rightarrow K^+ \Sigma^+$ and $K^- p \rightarrow \pi^- \Sigma^+$) do not show this behaviour. Also the observed weak EXD violation is smaller than that predicted by the model. In view of this we performed a fit to data on channels I and II with incident momenta > 7.0 Gev/c. A majority of this data had not been available at the time Navelet and Stevens published their paper. We allowed only the cut and trajectory parameters to vary.

We used 208 data points for the 10 parameters fit and the χ^2 per degree of freedom was found to be 1.21. In our fit we varied the experimental normalisations within the quoted errors.

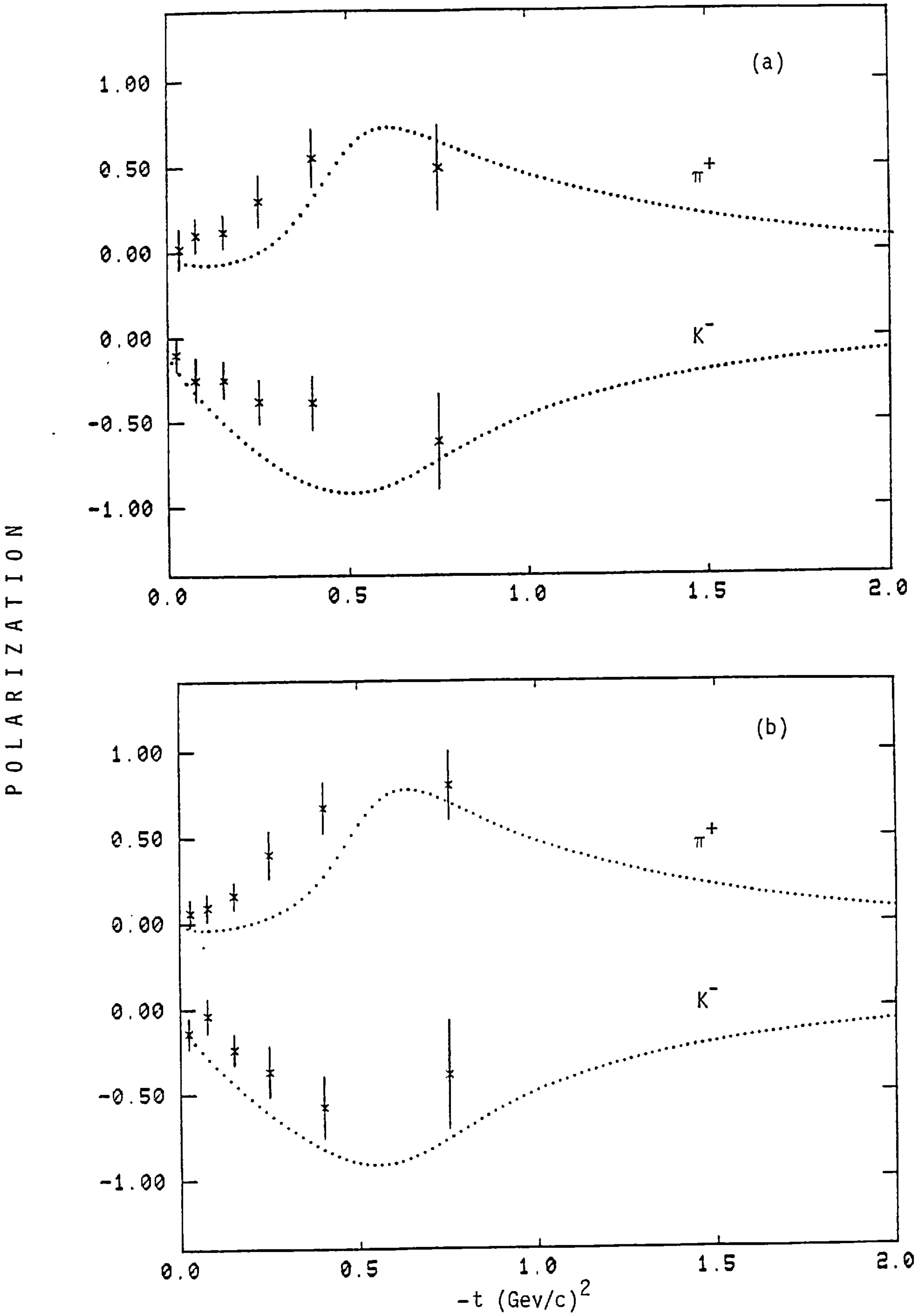

Fig. 7.16 Our polarization data compared with the predictions of the Navelet and Stevens model (Ref. 37).
(a) 7.0 Gev/c
(b) 11.5 Gev/c

Figs 7.17 to 7.20 show that the parameterization describes the differential cross-section and polarization data that were used fairly well. The summed polarization at 7.0 and 11.5 Gev/c compare much more favourably than the predictions of Navelet and Stevens (the solid line in Fig. 7.11). On the summed plot the curves reflect the effect of the cut term.

The values of the parameters obtained are listed in Table 7.1. The differences between the Navelet and Stevens and our sets are outlined. The vector and tensor trajectory intercepts are closer together while the slope has increased towards the value given by $K^*(890)$ and $K^{**}(1420)$ masses (0.79). These signify a smaller EXD violation. The cut trajectories are flatter with slightly lower intercepts. The effective cut strength relative to the pole has almost halved for the vector cut and is down to about two-thirds of the N - S value for the tensor cut amplitude. Thus the significance of the cut term seems to be decreasing with energy.

The amplitude structure is not markedly different from that predicted by the Navelet and Stevens parameterization. The amplitudes as obtained by our fit for $\pi^+ p \to K^+ \Sigma^+$ at 7.0 Gev/c are illustrated in Fig 7.21. The major features are listed below:

a. Helicity flip amplitudes are roughly consistent with Regge pole behaviour.

b. There is a small EXD violation in both the flip and non-flip amplitudes.

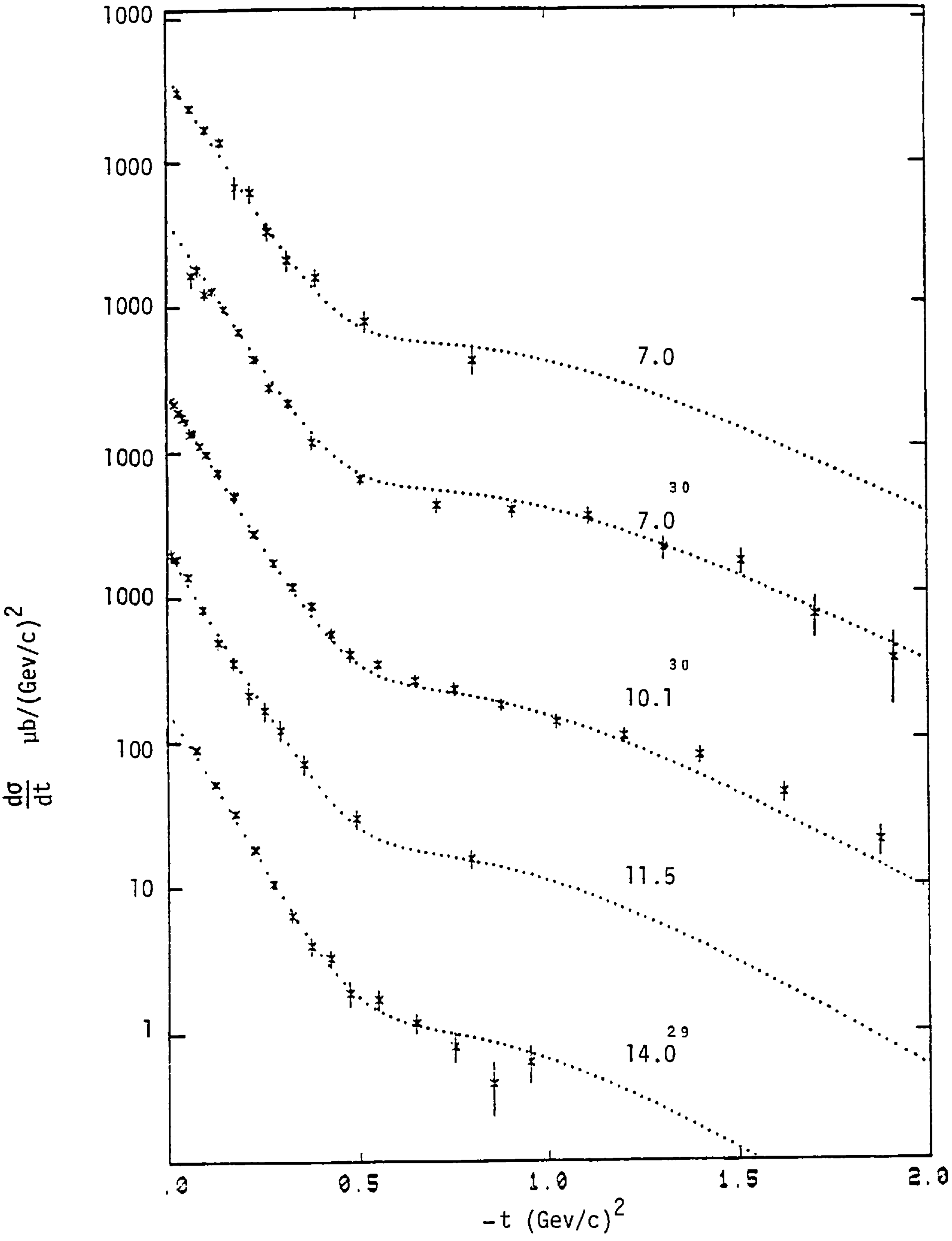

Fig. 7.17 Fits to the differential cross-sections

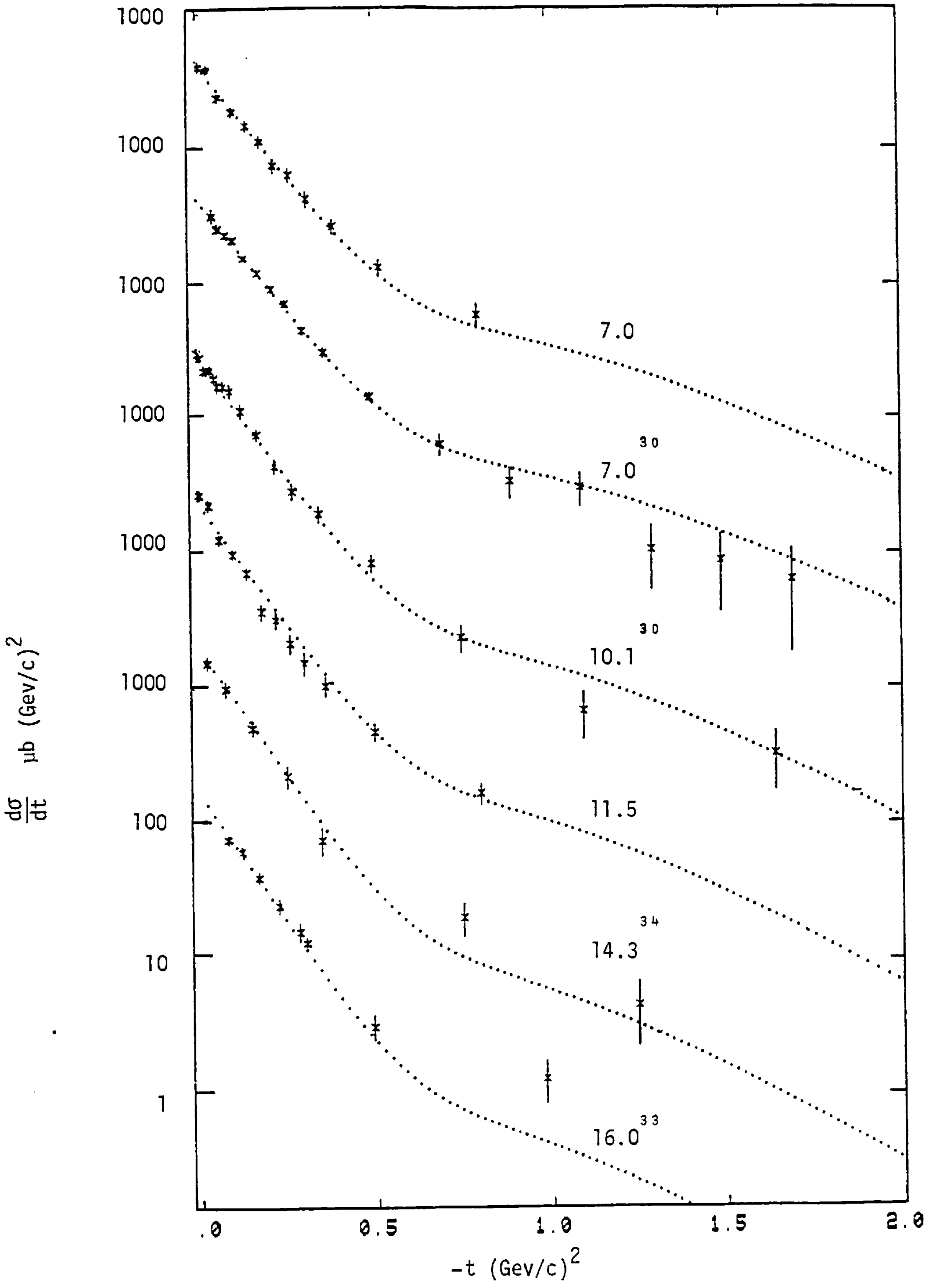

Fig 7.18 Fits to the differential cross-sections $K^- p \to \pi^- \Sigma^+$

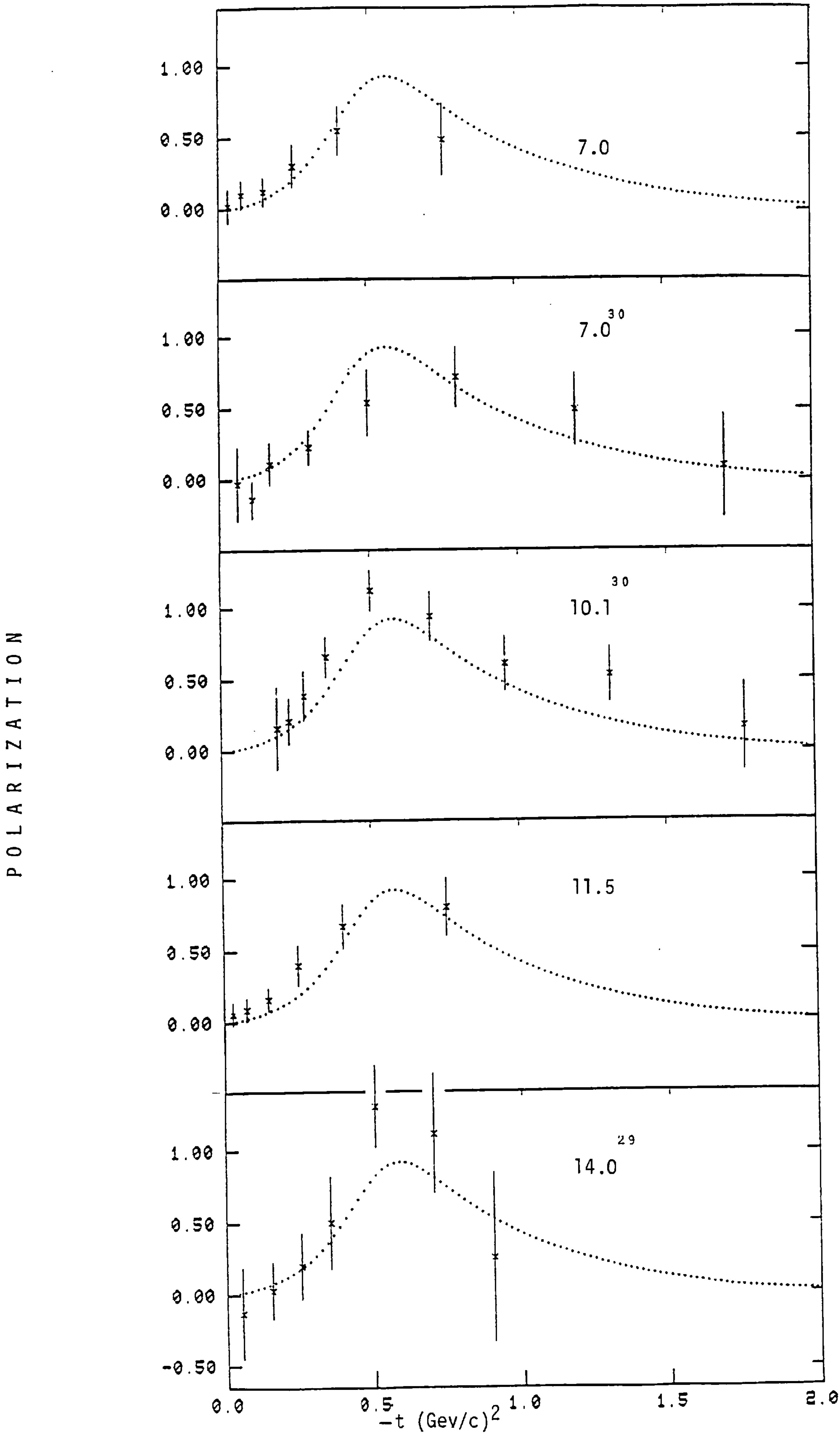

Fig. 7.19

Fits to Polarization $\pi^+ p \rightarrow K^+ \Sigma^+$

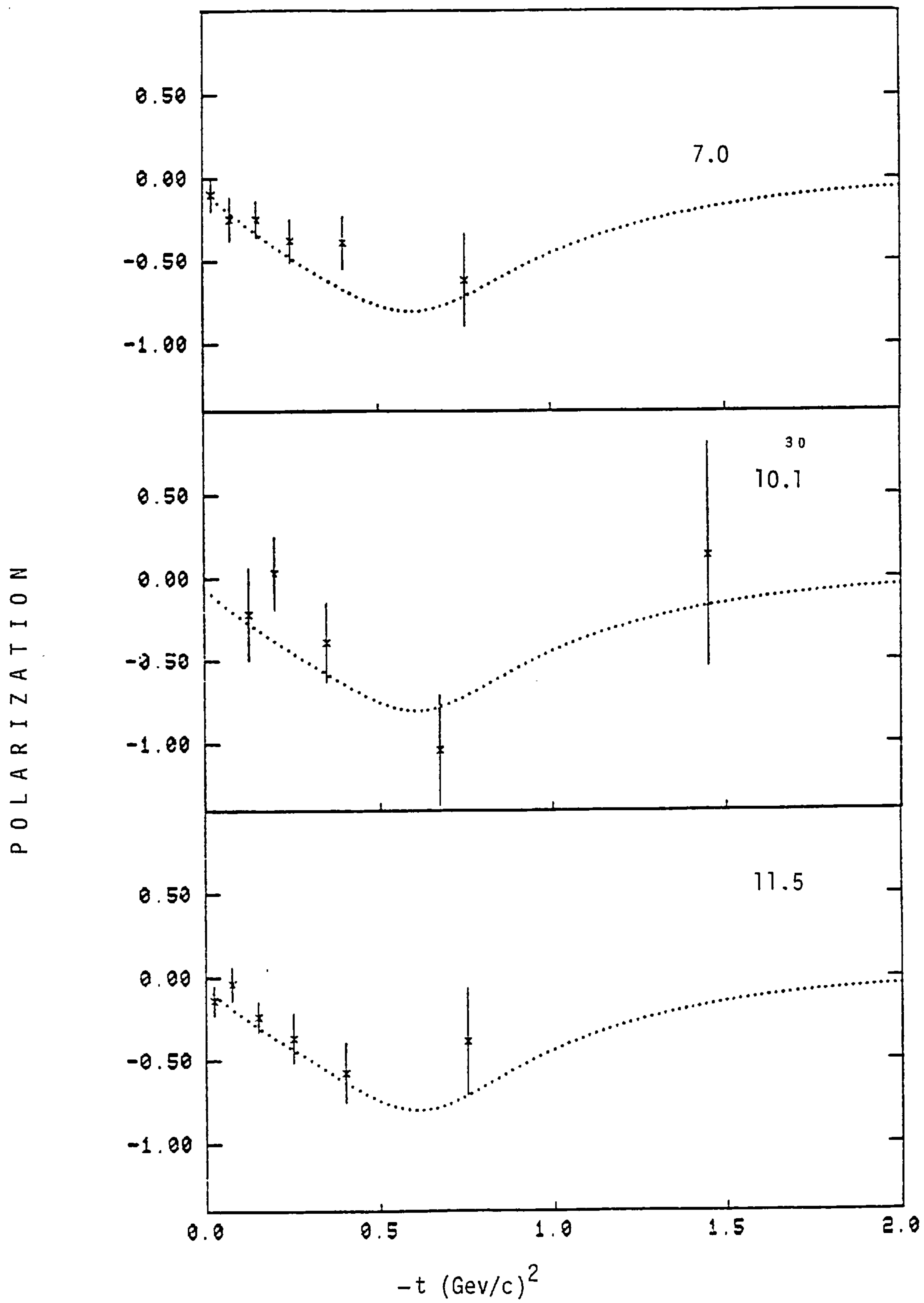

Fig 7.20 Fits to polarization

$K^- p \rightarrow \pi^- \Sigma^+$

```
--- POLE ---
                    γ                        a
    VECTOR          ++ : 10.340              ++ : 2.414
    TENSOR          ++ : 11.150              ++ : 1.331

    VECTOR          +- : -9.862              +- : 1.895
    TENSOR          +- : -7.114              +- : 1.895

      (V) = 0.351 + 0.754*T
      (T) = 0.317 + 0.754*T

--- CUT ---

    VECTOR          ++ : 0.565               +- : 0.053
    TENSOR          ++ : 1.085               +- : 0.200

      (V) = 0.098 + 0.474*T
      (T) = 0.110 + 0.474*T
```

Table 7.1 The values of the parameters obtained in our fit.

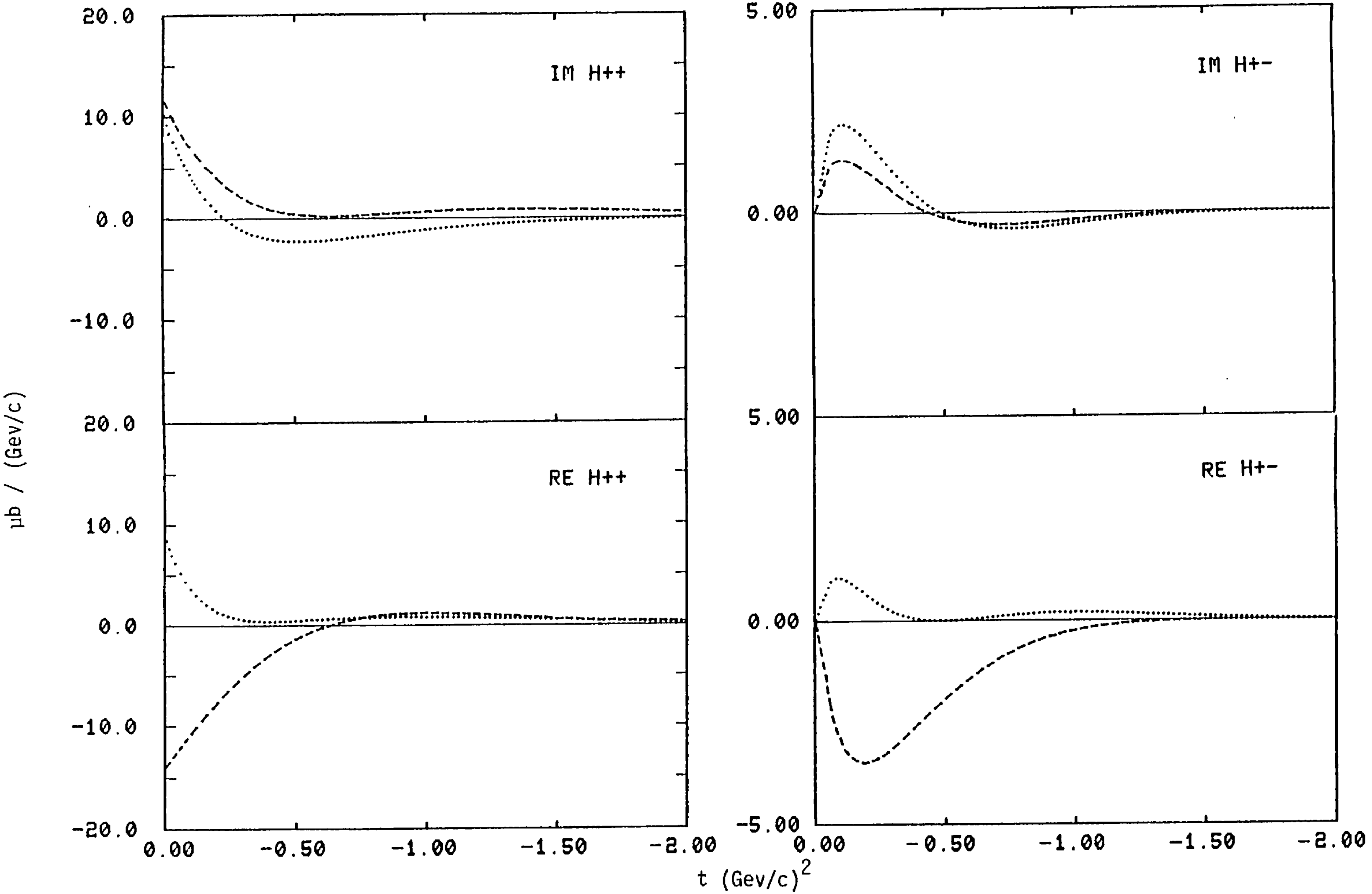

Fig 7.21 The imaginary and real parts of the amplitudes as obtained from our fit at 7.0 Gev/c for the channel

Key: ....K^*_V, ____K^*_T

c. I m K^*_V (non-flip) amplitude is peripheral but Im K^*_T (non-flip) is not.

d. Re K^*_V (non-flip) is consistent with Regge behaviour ($\sim 1 - \cos \pi\alpha$).

e. The effective cuts required have a steep, rather pole-like effective trajectory.

In Fig. 6.3 a flattening in the differential cross-section at $|t| \gtrsim 0.5$ is observed. This can be explained by the large relative contribution of the spin-flip amplitude to the differential cross-section as illustrated by Fig. 7.22.

It is seen that with reasonable assumptions we can deduce the amplitudes from differential cross-section and polarization measurements. Lower energy data on line reversed reactions proceeding via HYCEX show hyperon polarizations having the same sign at low $|t|$. However, our data does not show this behaviour. The model we chose cannot describe, with the same parametrization, all the polarization data on Σ^+ production in channels I and II.

In general, simple Regge picture has failed to describe all two body scattering data in quantitative detail. In attempts to obtain agreement with data, corrections to the simple Regge pole model have been applied. The realisation of these corrections (absorption, cuts etc) is still uncertain. This has led to a proliferation of Regge based models each obtaining agreement with only parts of the data.

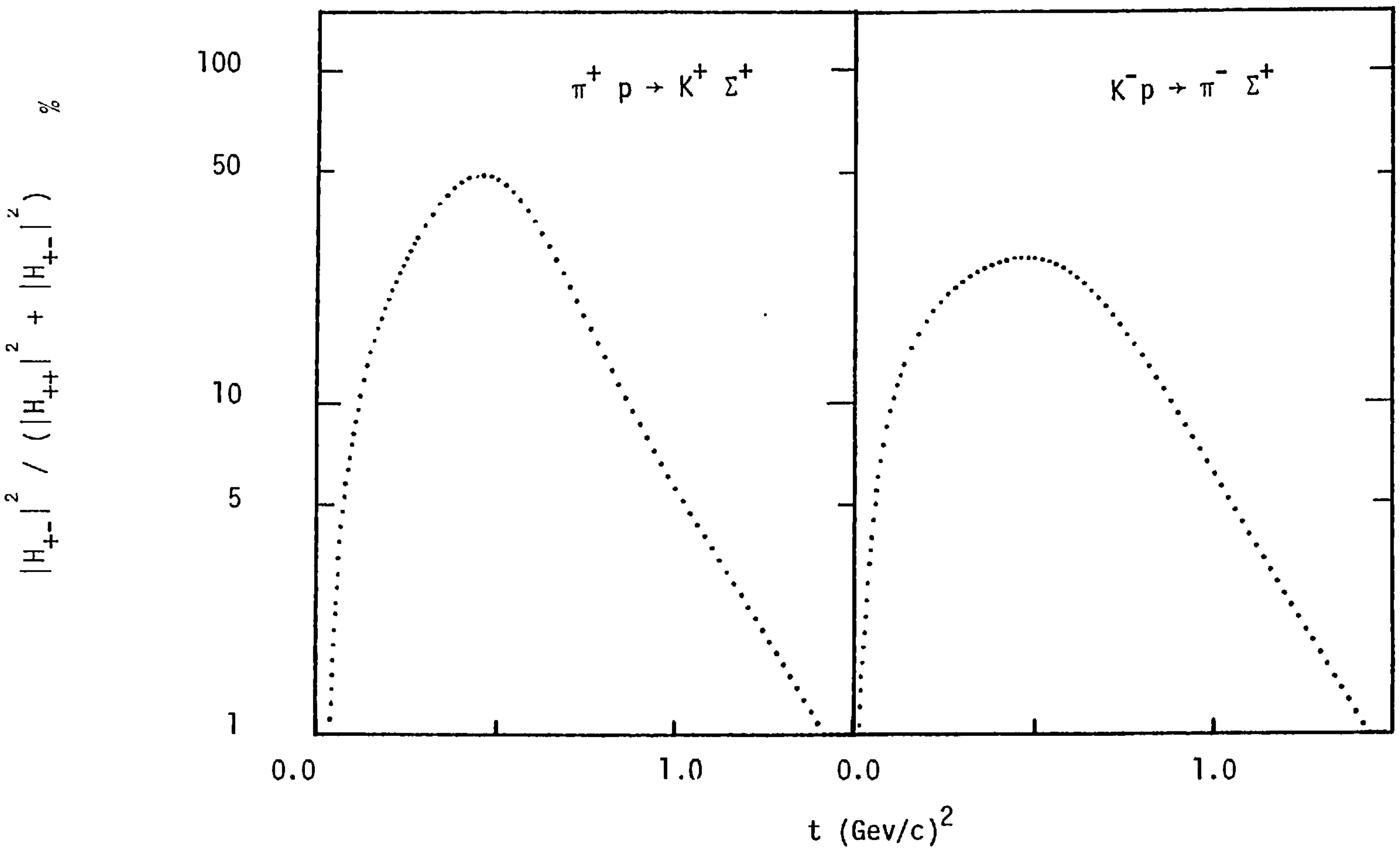

Fig 7.22 The relative contribution of the spin-flip amplitude to the differential cross-section obtained using the amplitudes from our fit.

Data from exotic reactions would help our understanding of these corrections because cuts alone should appear since no Regge poles can be exchanged. Hence we will be able to study cuts arising from $R \otimes R$ exchanges. Also data from polarized targets would be useful since one can then extract the amplitudes with no model dependent assumptions and hence discriminate between various models.

7.10 Conclusions

We have studied the line reversed pair of reactions $\pi^+ p \to K^+ \Sigma^+$ and $K^- p \to \pi^- \Sigma^+$ and found them to be dominated by the exchange of vector $K^*(890)$ and tensor $K^*(1420)$ Regge trajectories. We see a smaller violation of EXD than observed at lower energies. The violation seems to be decreasing with energy when compared with the 11.5 Gev/c SLAC experiment carried out on the same apparatus. Polarization measurements of the Σ^+ show a reflection symmetry between the π^+ and K^- reactions at both energies, hence supporting the weak EXD hypothesis and ruling out strong EXD. By adopting the parameterization of the Navelet and Stevens model, and using HYCEX data in the interval $7.0 < P$ incident < 16.0, an amplitude analysis was performed enabling the extraction of the amplitudes which provided an adequate description of the data that were used.

APPENDIX I

This appendix gives the derivation of expressions 4.2.1.(i) and 4.2.2.(i), used in length and small angle weighting.

A1.1 Length weighting

The decay length distribution for Σ^+'s is described by an exponential.

If there are N_0 Σ^+'s at $\ell = 0$, then the number of Σ^+'s with decay length greater than ℓ is given by

$$N_\ell = N_0 \, E^{-\ell/\eta}$$

where the mean path length $\eta = \frac{pct}{m}$

with p being the momentum, t the proper lifetime

and m the mass of the Σ^+.

Thus the number of Σ^+'s decaying within a length such that $\ell_1 < \ell < \ell_2$ is given by

$$N_{12} = N_0 \, (E^{-\ell_1/\eta} - E^{-\ell_2/\eta})$$

If the detection efficiency between ℓ_1 and ℓ_2 is one and below one everywhere else, and if N_{12} is the number of events observed in the interval, then the true number of events is simply given by

$$N_0 = \frac{N_{12}}{E^{-\ell_1/\eta} - E^{-\ell_2/\eta}}$$

Thus each event in the interval $\ell_1 < \ell < \ell_2$ is weighted by the factor

$$\frac{I}{E^{-\ell_1/\eta} - E^{-\ell_2/\eta}}$$

If the projected length is used then the weighting factor is

$$\frac{I}{E^{-\ell_1 pr/\eta\cos\lambda} - E^{-\ell_2 pr/\eta\cos\lambda}}$$

where $\ell^{pr} = \ell\cos\lambda$ is the projected length and λ is the dip of the Σ^+ track.

A1.2 Small angle weighting

There are two major factors which contribute to the loss of events due to the opening angle between Σ^+ and the charged decay product being too small. These are discussed in the next three sub-sections.

A1.2.1 Some events may be lost if the decay plane of the Σ^+ is nearly perpendicular to the film plane resulting in a small projected opening angle. This is illustrated in Fig. A1.1.

To correct for such a loss, consider $\Sigma^+ \to n\pi^+$ decay. Without loss of generality, we can take the Σ^+ to be in the $x-z$ plane in the bubble chamber frame.

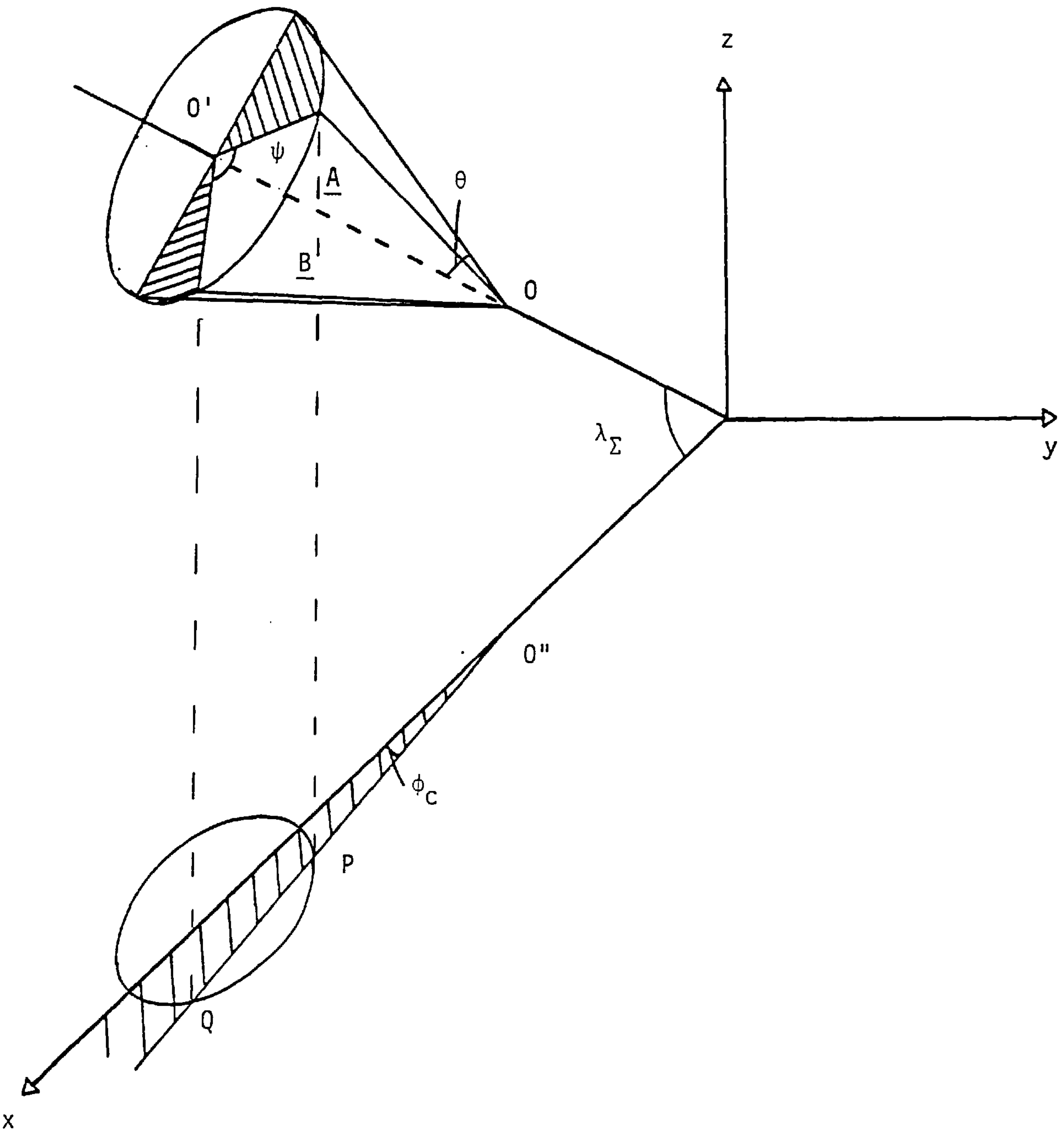

Fig. A1.1 The system for the small-angle weight.

Then $\phi_\Sigma = 0$. If θ is the angle between the Σ^+ and π^+ in space and ϕ_c is the minimum projected angle for 100% detection efficiency on the scanning table, then we will always observe the kink if the π^+ vector lies between the two vectors $\underline{A}$ and $\underline{B}$. Each event with a projected opening angle greater than ϕ_c has to be weighted by

$$W = \frac{\pi}{\psi} \qquad \text{see Fig. A1.1}$$

Evaluation of ψ

For Σ track, $S_x = |p_\Sigma| \cos\lambda_\Sigma$
$S_y = 0$
$S_z = |p_\Sigma| \sin\lambda_\Sigma$

For track A, $A_x = |A| \cos\lambda_A \cos\phi_c$
$A_y = |A| \cos\lambda_A \sin\phi_c$
$Az = |A| \sin\lambda_A$

and similar expressions for track B.

Now

$$\cos\theta = \frac{\underline{A}.\ \underline{S}}{|A|\,|S|}$$

$$= \cos\lambda_\Sigma \cos\lambda_A \cos\phi_c + \sin\lambda_\Sigma \sin\lambda_A$$

$$\therefore \quad \sin\lambda_A = \frac{\cos\theta\sin\lambda_\Sigma \pm \cos\phi_c\cos\lambda_\Sigma\sqrt{(\sin^2\lambda_\Sigma - \cos^2\theta + \cos^2\phi_c\cos^2\lambda_\Sigma)}}{\sin^2\lambda_\Sigma + \cos^2\phi_c\cos^2\lambda_\Sigma}$$

Hence λ_A and λ_B are determined.

Thus tracks A and B are now determined. If α is the angle between A and B, and since θ is the half angle of the cone in Fig. A1.1, and with reference to Fig. A1.2, it can be shown that

$$\sin\frac{\psi}{2} = \frac{\sin\frac{\alpha}{2}}{\sin\theta} \qquad \text{(ii)}$$

When θ is large such that the projected ellipse (fig. A1.1) encircles the decay point 0" we can have backward decay. Then we put

$$\lambda_A = \lambda_\Sigma + \theta, \quad \phi_A = 0 \quad \text{if} \quad \lambda_\Sigma + \theta > \frac{\pi}{2} \text{ , and}$$
$$\lambda_B = \lambda_\Sigma - \theta, \quad \phi_B = 0 \quad \text{if} \quad \lambda_\Sigma - \theta < -\frac{\pi}{2}$$

When θ is small such that the projected ellipse falls completely within ϕ_c, then all the decays will be missed. This will happen when

$$\sin^2\lambda_\Sigma - \cos^2\theta + \cos^2\theta_c \cos^2\lambda_\Sigma = 0$$
$$\Rightarrow \quad \sin\theta = \sin\phi_c \cos\lambda_\Sigma$$

and thus we will miss all the decays for which

$$\sin\phi_c \cos\lambda_\Sigma > \sin\theta \qquad \text{(iii)}$$

In Chapter 4 we determined ϕ_c to be 4^0 for $\Sigma^+ \to n\pi^+$ and 8^0 for $\Sigma^+ \to p\pi^0$ decay modes. A cut of $|t| < 1.0\ (\text{Gev}/_c)^2$ $(p_\Sigma < 1.3\ \text{Gev}/_c)$ on the $\Sigma^+ \to n\pi^+$ and $|t| < 0.6\ (\text{Gev}/_c)^2$ $(p_{\Sigma^+} < 0.82\ \text{Gev}/_c)$ was imposed on the data used for determination of the differential cross-sections (cf. Chapter). These cuts ensured that the projected ellipse never fell completely within ϕ_c or that a substantial number of events failed condition (iii).

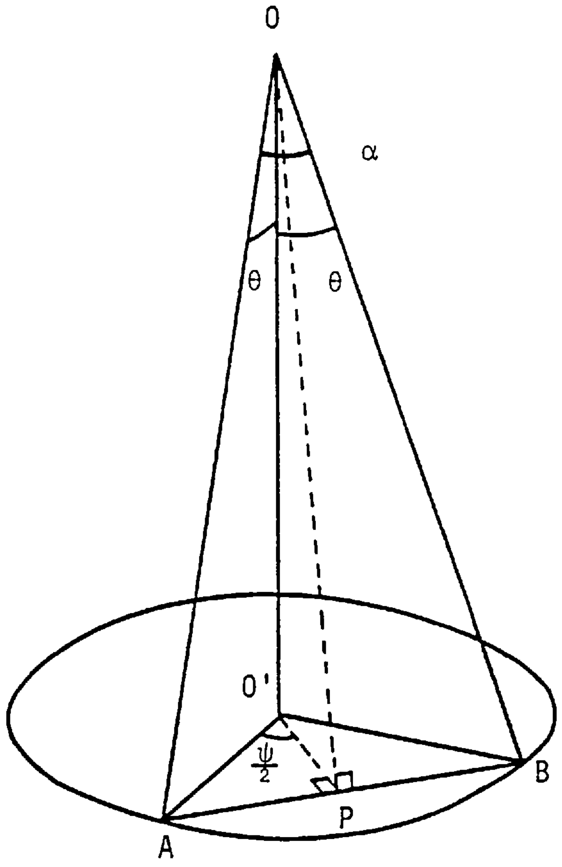

Fig. a1.2 A projection from Fig. A1.1

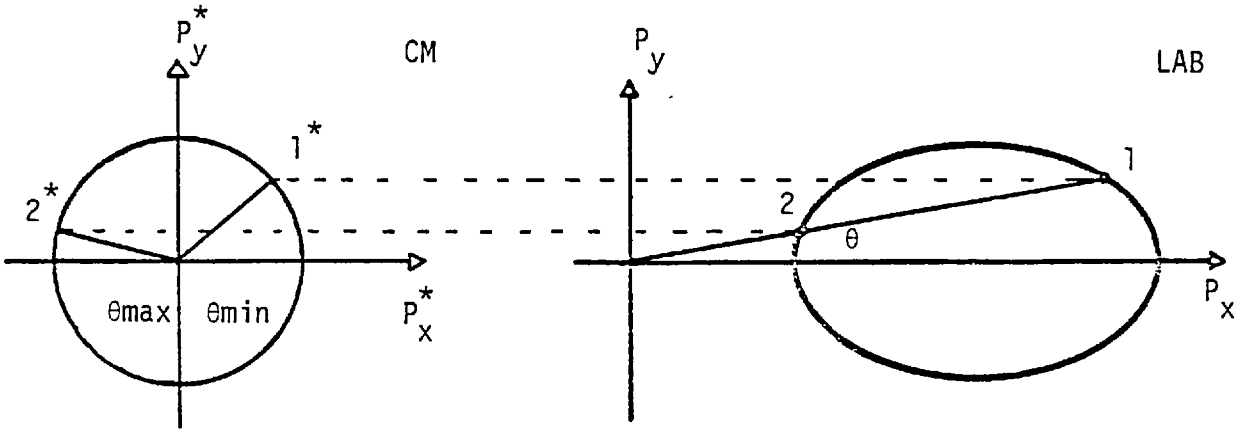

Fig A1.3 The rest and laboratory frames of Σ^+ to illustrate the decay

Nevertheless, some events satisfying condition (iii) are lost and an additional weight is required. This is the second factor contributing to small angle losses.

A1.2.2 Assuming an isotropic angular distribution for the π^+ in the Σ^+ rest frame, we can calculate the range of values of $\cos\theta^*$ which always give lab angles θ such that

$$\sin\theta < \sin\phi_c \cos\lambda_\Sigma$$

The additional weight with reference to fig. A1.3 is

$$W_2 = \frac{2}{\cos\theta^*_{min} - \cos\theta^*_{max}}$$

Evaluation of θ^*_{min} and θ^*_{max}:

Consider the parameters of the π^+ in Σ^+ rest frame and the lab frame.

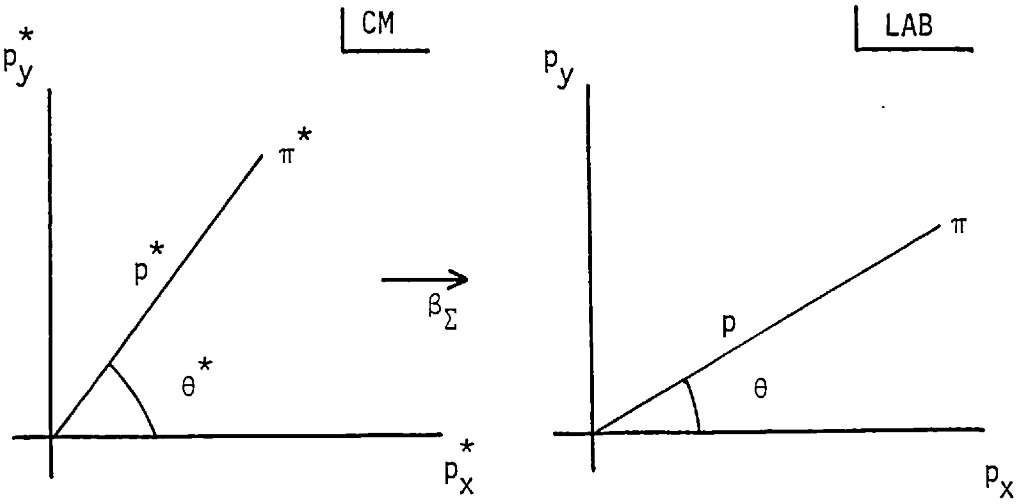

Fig. A1.4

Employing the Lorentz Transformation, with the decay occuring in the x - y plane, and the Σ travelling in the x direction in the lab, then the parameters of the π^+ are given by

$$p_x = \gamma(p_x{}^* + \beta E^*)$$
$$p_y = p_y{}^*$$
$$p_z = p_z{}^* = 0$$

$$\therefore \quad (p^*)^2 = (p_x{}^*)^2 + (p_y{}^*)^2$$

$$= \frac{1}{\gamma^2}(p_x - \beta\gamma E^*)^2 + (p_y)^2$$

substituting for

$$p_x = p\cos\theta$$

and $$p_y = p\sin\theta$$

We arrive at an equation for an ellipse,

$$p^2\ (\sin^2\theta + \frac{\cos^2\theta}{\gamma^2}) + p\ (-\ \frac{2\beta E^*\ \cos\theta}{\gamma}) + (\beta^2 E^{*2} - p^{*2}) = 0 \quad (iv)$$

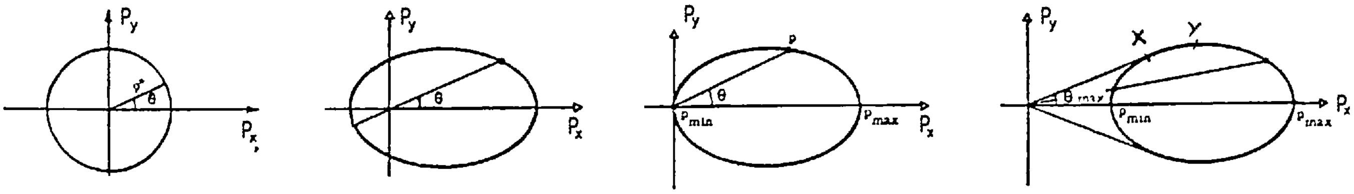

a) CM b) $V_\Sigma < V_+^*$ c) $V_\Sigma = V_+^*$ d) $V_\Sigma > V_+^*$

Fig. A1.5

For a given θ, p is double valued so

if $$A = \sin^2\theta + \frac{\cos^2\theta}{\gamma^2}$$

$$B = \frac{2\beta E^* \cos\theta}{\gamma}$$

and $$C = \beta^2(E^*)^2 - (p^*)^2$$

then $$p_{\substack{\max\\ \min}} = \frac{-B \pm \sqrt{B^2 - 4AC}}{2A}$$

leading to

$$\tan\theta^*_{\substack{\min\\ \max}} = \frac{p_{\substack{\max\\ \min}} \sin\theta}{\gamma\left(p_{\substack{\max\\ \min}} \cos\theta - \beta E\right)}$$

Thus we can now determine W_2.

There are three different forms of ellipses to be considered. These are illustrated in Fig. A1.5 where, c = 1, and V^*_+ is the velocity of the charged decay secondary in the Σ rest frame.

At our Σ momenta, situation (a) is encountered for $\Sigma^+ \rightarrow n\pi^+$ decays while situation (c) is encountered for $\Sigma^+ \rightarrow p\pi^0$ decays. Thus in $\Sigma^+ \rightarrow n\pi^+$ decays, it may happen that even when θ is small, some backward decays may be observed (c.f. fig. A1.5 (b) point X). This is taken into account by putting $\cos\theta^*$ max = -1.

A1.2.3 Charged low momenta secondaries from Σ^+'s may cause some of the kink topology events to be lost, either at the scanning stage or in the processing chain. To account for this loss, momentum cuts of

$$\Sigma^+ \rightarrow p\pi^0 \quad : \qquad p_p > 180 \text{ Mev/c}$$
$$\Sigma^+ \rightarrow n\pi^+ \quad : \qquad p_{\pi+} > 55 \text{ Mev/c}$$

were imposed.

With reference to fig. A1.5 (d), pt. X corresponded to $\cos\theta^*_{max}$, and if $OX < p_c$ the momentum cut, and if $OY = p_c$, the above loss can be accounted for by using θ^*_{max} corresponding to the point Y.

A1.2.4 The overall small angle weight is given by

$$W_s = W_1 \cdot W_2$$

$$= \frac{\pi}{\psi} \cdot \frac{2}{\cos\theta^*_{min} - \cos\theta^*_{max}}$$

Regge Phenomenology

1. V.D. Barger and D.B. Cline, Phenomenological theories of high energy scattering (Benjamin, 1969).

2. P.D.B. Collins, An introduction to Regge theory and high energy physics (CUP, 1977).

3. H. Harrari, Phys. Rev. Lett. 22, (1969) 562.

   J.L. Rosner, Phs. Rev. Lett. 22, (1969) 689.

4. A.C. Irving and R.P. Worden, Phys. Rep. 34C (1977) 117.

5. L. Jauneau, Introduction to Regge Poles, 1969 Herceg-Novi School of Physics.

6. K. Kajantie, Dual models and dual phenomenology, 1970 CERN School of Physics, CERN 71-7.

7. R.J.N. Phillips, High energy two-body phenomenology, 1972 CERN School of Physics, CERN 72-17.

8. B. Sadoulet, Absorption effects in charge and hypercharge exchange reactions. Two Body Collisions, 7th Rencontre de Moriond (1972).

The Experiment

9. The Proposal, Imperial College, IC/HENP/74/01.

10. J. Ballam and R.D. Watt, Hybrid bubble chamber systems, Ann. Rev. Nucl. Sci. 27 (1977) 75.

11. The software algorithm was developed by P.J. Dornan and A.P. White of the Imperial College Bubble Chamber group.

12. T.H. Fieguth and R.A. Gearhart, R.F. separators and separated beams at SLAC, SLAC - PUB - 1552 (1975).

13. R.C. Field, The SLAC 1m. bubble chamber hybrid facility, SLAC internal report S.H.F. Memo 67 (1977).

14. R. Lewis, SLAC Internal Report S.H.F. Memo 13 (1976).

15. R. Lewis, Normalization, SLAC Internal Report S.H.F. Memo 46 (1976).

16. D. Miller, SLAC Internal Report S.H.F. Memo 1 (1975).

Data Processing

17. J.B. Gay, Weighting of V^0 and of kink events. CERN/D.PhII/X42 Note 75-1 (1975).

18. A.J. de Groot, Production of charged sigma-hyperons in 4.2 Gev/c K^-p interactions. Ph.D. Thesis, Zeeman Lab., Amsterdam (1975).

19. G. Hall, Fast track fitting in SLAC hybrid experiment. Imperial College Internal Memo IC/HENP/PN/27 (1975).

20. J.S. Loos et. al., Phys. Rev. <u>173</u> (1968) 1330.

21. B. Penney, An automatic measuring machine for bubble chamber film: its use for K^+p experiment. Ph.D. Thesis Imperial College (1971).

22. P. Villemoes, Data processing in bubble chamber experiments. 1970 CERN Computing and Data Processing School, CERN 71-6.

23. Program 'HYDRA Geometry', CERN Program Library.

24. Program 'GRIND', CERN TC Program Library long write-up.
    a. GRIND/E STOMAS
    b. GRIND/E QUAMIS
    c. GRIND/E SUBCL5

25. Program 'AUTOGRIND', CERN TC Program Library.

Measurements of $\pi^+ p \to K^+ \Sigma^+$

26. M.W. Arenton et. al., Argonne National Laboratory ANL-HEP-PR-78-24, (Preliminary 70 Gev/c).

27. P.A. Baker et. al., Phys. Rev. Lett. 40 (1978) 678.

28. J. Ballam et. al., Phys. Rev. Lett. 41 (1978) 676.

29. A. Bashian et. al., Phys. Rev. D4 (1971) 2667. (3.5, 3.75, 4, 4.25, 5, 6, 10, 14 Gev/c).

30. A. Berglund et. al., Phys. Lett, 73B (1978) 369.

31. K.S. Han et. al., Phys. Rev. Lett. 24 (1970) 1353. (3, 4, 5 Gev/c).

32. S.M. Pruss et. al., Phys. Rev. Lett. 23 (1969) 189 (3, 3.25, 4, 5.05, 7 Gev/c).

Measurements of $K^- p \to \pi^- \Sigma^+$

33. D. Birnbaum, Phys. Lett. 31B (1970) 484. (8,16 Gev/c).

34. B. Chaurand, Nucl. Phys. B117 (1976) 1. (14.3 Gev/c).

35. G.G.G. Massaro et. al., Phys. Lett. 66B (1977) 385. (4.2 Gev/c).

Also references 27, 28 and 29.

Amplitude Analysis

36. A.C. Irving, A.D. Martin and V. Barger, Nuovo Cimento 16A (1973) 573.

37. H. Navalet and P.R. Stevens, Nucl. Phys. B104 (1976) 171.

Other References

38. P. Bonamy et. al., Phys. Rev. Lett. 20 (1966) 75.

39. S.L. Lloyd, A study of the reaction $\pi^- p \rightarrow K^0 \Lambda$ at 5 Gev/c using a polarized proton target, Ph.D. Thesis, Imperial College, 1978.

40. D. Perkins, Introduction to high energy physics, (Addison-Wesley, 1972).

ACKNOWLEDGEMENTS

It has been a pleasure to work in the HENP group at Imperial College for which I would like to thank all the members of the group.

In particular, I am grateful to Dr. P.J. Dornan for the direction and encouragement which made this work possible.

Also I would like to thank Professor Ian Butterworth for the opportunity of working in HENP.

The part played by the SLAC bubble chamber group in this experiment is gratefully acknowledged.

The SRC provided financial support for a period of three years.

The excellent typing of this thesis, due to Mandy Clausson is greatly appreciated.

Finally, I would like to thank Vatsala for not only putting up with me but also for keeping me in good spirits during the course of this work.